

POLITECNICO DI TORINO

**Corso di Laurea Magistrale in
Ingegneria Meccanica**

Tesi di Laurea Magistrale

**High Temperature Sensitive Optimal
Calibration of Energy Management for a
Parallel-Through-the-Road Hybrid Electric
Vehicle**



Relatori:

Prof. Giovanni BELINGARDI

Ing. Pier Giuseppe ANSELMA

Candidato:

Marco DEL PRETE, s256901

A.A. 2019/2020

Summary

The current trend towards an ever greater electrification of vehicles brings to life a whole series of new stimulating design issues. Among these, the aging process that affects Lithium-ion batteries life is of particular importance since it turns out to be extremely sensitive to the variation of operating conditions that normally occurs in the electric ESSs (energy storage systems) installed on hybrid and electric vehicles, namely the fluctuations of temperature, C-rate and DOD (depth of discharge).

In this work, in hopes of examining interesting aspects of the aforementioned topic, a quasi-static model of a plug-in hybrid vehicle, inspired by the *Jeep® Renegade 4xe*, has been implemented in *Simulink* (by *MathWorks®*) with the purpose of evaluating how a reasonable management of the battery temperature, aimed at safeguarding the battery life and obtained by means of a PSO (particle swarm optimization), affects the actual exploitation of the electric power during driving missions.

Key words: hybrid electric vehicle, battery aging, battery thermal management, battery state of health.

Contents

List of Figures	IV
List of Tables	VI
Definitions/Abbreviations	VII
1. Preface	1
1.1. Introduction to Battery Aging: Calendar and Cycle life	2
1.2. Cycle Life Evaluation by means of Quasi-Static Vehicle Models.....	4
1.3. Objectives.....	5
1.4. Jeep® Renegade 4xe.....	6
1.5. Thesis Outline	7
2. State of the Art	9
2.1. Capacity Fade Models.....	9
2.2. Battery Thermal Management in Quasi-Static Vehicle Models.....	12
2.3. Particle Swarm Optimization	13
3. Jeep® Renegade 4xe Quasi-Static Model	15
3.1. Steady-State Models of Powertrain Motors.....	15
3.2. Vehicle Free Body Diagram.....	19
3.3. Driver Model.....	21
3.4. Default Rule-Based EMS.....	24
3.5. Transmission Specifications.....	29
4. High Voltage Battery Model	34
4.1. Equivalent Electric Circuit Model.....	34
4.2. Single Temperature Lumped-Parameter Model and BTMS.....	39
4.2.1. <i>Air Cooling System</i>	41
4.2.2. <i>Heating Pads System</i>	46
4.3. Throughput-Based Battery Capacity Fade Model	47
5. Model Performances and Sensitivity Analysis	52
5.1. Driving Missions.....	52
5.2. Model Reliability by means of Consumptions Comparison and Battery Lifetime Calculation.....	56
5.3. Sensitivity Analysis Considerations	64

6. PSO Implementation	73
6.1. PSO Theoretical Basics	73
6.2. Problem Characterization	76
6.3. Cost Function and Research Domain Determination	78
7. Calibration Results	84
7.1. Fuel Consumptions Minimization	87
7.2. Optimized Rule-Based EMS	89
7.3. High-Level Strategy	91
8. Conclusions	96
References	99
Papers.....	99
Images	103
Acknowledgements	104

List of Figures

- Figure 1.1:** Comparison in terms of specific power and energy among different ESSs, p.1
- Figure 1.2:** Specific energy density of different typologies of batteries compared to gasoline, p.2
- Figure 1.3:** Temperature influence on SOH variation over time for a NMC:LMO/graphite Li-ion cell under unitary C-rate, p.3
- Figure 1.4:** Comparison between commonly used HEVs EMSs, p.5
- Figure 1.5:** *Jeep® Renegade 4xe*, p.6
- Figure 2.1:** Number of papers published per year about HEVs from 1990 to 2017, p.9
- Figure 2.2:** LiFePO₄ cylindrical cell (*ANR26650M1B*) by A123 Systems, p.11
- Figure 2.3:** Flock of birds, whose behavior is at the basis of PSO, p.14
- Figure 3.1:** ICE maximum torque, p.17
- Figure 3.2:** ICE friction torque, p.17
- Figure 3.3:** ICE efficiency map, p.17
- Figure 3.4:** ICE optimal operating line, p.17
- Figure 3.5:** MGP4 maximum torque, p.17
- Figure 3.6:** MGP0 maximum torque, p.17
- Figure 3.7:** MGP4 power losses, p.18
- Figure 3.8:** MGP0 power losses, p.18
- Figure 3.9:** Vehicle proceeding on a slanting road, p.20
- Figure 3.10:** PID controller, p.22
- Figure 3.11:** Intrinsic difference between desired and actual speed, p.24
- Figure 3.12:** Powertrain diagram, p.25
- Figure 3.13:** Flowchart illustrating the logic of powertrain management, p.26
- Figure 3.14:** Gear logic implemented in Stateflow tool, p.31
- Figure 4.1:** Cell equivalent electric circuit model, p.35
- Figure 4.2:** Battery equivalent electric circuit model obtained as Thevenin equivalent circuit, p.36
- Figure 4.3:** Battery equivalent electric circuit model in operation, p.37
- Figure 4.4:** Battery cells configuration, p.40

- Figure 4.5:** Air cooling circuit, p.41
- Figure 4.6:** Common convective coefficient for air and water, p.44
- Figure 4.7:** Ah-throughput evolution at 25°C according to C-rate variation, p.49
- Figure 4.8:** Ah-throughput evolution at C-rate=2 according to temperature variation, p.50
- Figure 5.1:** *WLTP* driving cycle, p.53
- Figure 5.2:** *RTS 95* driving cycle, p.53
- Figure 5.3:** *FTP 75* driving cycle, p.53
- Figure 5.4:** *HWFET* driving cycle, p.53
- Figure 5.5:** RWD01 driving mission, p.53
- Figure 5.6:** RWD06 driving mission, p.53
- Figure 5.7:** RWD03 driving mission, p.54
- Figure 5.8:** RWD04 driving mission, p.54
- Figure 5.9:** *FTP 75* (flat route) desired and actual accelerations, p.55
- Figure 5.10:** RWD01 (sloping route) desired and actual accelerations, p.55
- Figure 5.11:** Intervention of the ICE while travelling the *WLTP* in Electric mode and starting from a SOC value of 0.95 or 0.70, p.58
- Figure 5.12:** Intervention of the ICE while travelling the *WLTP* in Electric mode and starting from a SOC value of 0.40, p.60
- Figure 5.13:** SOC evolution while travelling the *WLTP* in Electric mode and starting from a SOC value of 0.95 or 0.70, p.61
- Figure 5.14:** Intervention of the ICE while travelling the *WLTP4* in Electric mode, with $SOC_0=0.95$, at $T_a=25^\circ\text{C}$ and with the cooling system off, p.63
- Figure 5.15:** Intervention of the ICE while travelling the RWD03 in Electric mode, with $SOC_0=0.95$ and at $T_a=-5^\circ\text{C}$, p.69
- Figure 5.16:** SOC and battery temperature variation while travelling the RWD03 in Electric mode, with $SOC_0=0.95$ and at $T_a=-5^\circ\text{C}$, p.69
- Figure 6.1:** Schematic representation of the updating of particle velocity, p.74
- Figure 6.2:** D^N portion effectively explored by the particles when D^N is used, p.82
- Figure 6.3:** D^N portion effectively explored by the particles when \bar{D}^N is used, p.82
- Figure 7.1:** $\Delta T_{CSon,best}$ variation over T_a , p.86
- Figure 7.2:** $\Delta T_{CSoff,best}$ variation over T_a , p.86
- Figure 7.3:** $\Delta SOC_{var,best}$ variation over T_a , p.86
- Figure 7.4:** $f_{100km,ave,best}$ variation over T_a , p.86
- Figure 7.5:** RWD03 SOC evolution with SOC_{var} equal to 0.30 and 0.40, at $T_a=25^\circ\text{C}$, p.88
- Figure 7.6:** SOH evolution while travelling the *WLTP* at $T_a=25^\circ\text{C}$, in Electric mode and starting from a SOC value of 0.95, p.93
- Figure 7.7:** Improvements in fuel consumptions by means of an online evaluation of battery life evolution, for both cases of HVAC system on and off, p.94

List of Tables

- Table 3.1:** Technical specifications provided by *FCA* about the motors installed on the two versions of *Renegade 4xe* (respectively 190 hp and 240 hp), p.16
- Table 3.2:** Technical specifications of the motors employed in the model implemented, p.18
- Table 3.3:** Road load coefficients, p.19
- Table 3.4:** Radius of the wheels, transmission ratios and respective efficiencies, p.31
- Table 4.1:** Cell and battery nominal values of capacity and voltage, p.37
- Table 4.2:** Battery and air thermal parameters, p.40
- Table 4.3:** Air convective coefficients, p.44
- Table 4.4:** Battery aging parameters for A123 26650 cell, p.49
- Table 5.1:** Driving missions main characteristics: distance, difference of altitude end-beginning, maximum speed and total time, p.54
- Table 5.2:** Consumptions and final values of SOC related to the simulation of the *WLTP* at $T_a=25^\circ\text{C}$ and with the cooling system off by using the different driving modes and distinct initial values of SOC, p.58
- Table 5.3:** Consumptions and final values of SOC related to the simulation of the *WLTP4* (four *WLTP* disposed in series) at $T_a=25^\circ\text{C}$ and with the cooling system off by using the different driving modes and distinct initial values of SOC, p.59
- Table 5.4:** Final values of SOH related to the simulations of *WLTP* and *WLTP4*, p.60
- Table 5.5:** Battery lifetime values referring to *WLTP* and *WLTP4* when simulated in Electric mode, with $SOC_0=0.95$, at $T_a=25^\circ\text{C}$ and with the cooling system off, p.63
- Table 5.6:** Battery sensitive analysis with the HVAC system turned off, p.67
- Table 5.7:** Battery sensitive analysis with the HVAC system operating, p.68
- Table 7.1:** PSO outcomes for HVAC system turned off, p.84
- Table 7.2:** PSO outcomes for HVAC system operating, p.84
- Table 7.3:** Integration to PSO outcomes for HVAC system turned off, p.85
- Table 7.4:** Integration to PSO outcomes for HVAC system operating, p.85

Definitions/Abbreviations

BSFC	brake-specific fuel consumption
BTMS	battery thermal management system
DOD	depth of discharge
ECM	equivalent circuit model
EMS	energy management strategy
EOL	end of life
ESS	energy storage system
FTP 75	Federal Test Procedure 75 driving cycle
HEV	hybrid electric vehicle
HV	high voltage
HVAC	Heating, Ventilation, and Air Conditioning
HWFET	Highway Fuel Economy Test driving cycle
ICE	internal combustion engine
MGPO	electric motor/generator in configuration P0
MGP4	electric motor/generator in configuration P4
PID	proportional–integral–derivative
PSO	particle swarm optimization
QSA	quasi-static approach
RB	rule-based
RTS 95	random test standardized 95 driving cycle
RWD01	extra-urban uphill driving mission
RWD03	long highway driving mission
RWD04	down mountain driving mission
RWD06	extra-urban downhill driving mission
SEI	surface electrolyte interface/interphase
SI	International System of Units
SOC	state of charge
SOH	state of health
WLTP	Worldwide Harmonized Light Vehicles driving cycle
WLTP4	four WLTP disposed in series

1. Preface

Nowadays, the continuous reduction of the automotive environmental impact finds in the hybrid and electric vehicles a valuable ally [1]. Nevertheless, the consequent introduction of Lithium-ion ESSs (energy storage systems), which are currently the most employed electrochemical solution (figure 1.1) [2], brings along some critical issues (included some safety features [2]) that really restrict the diffusion of electrified powertrains.

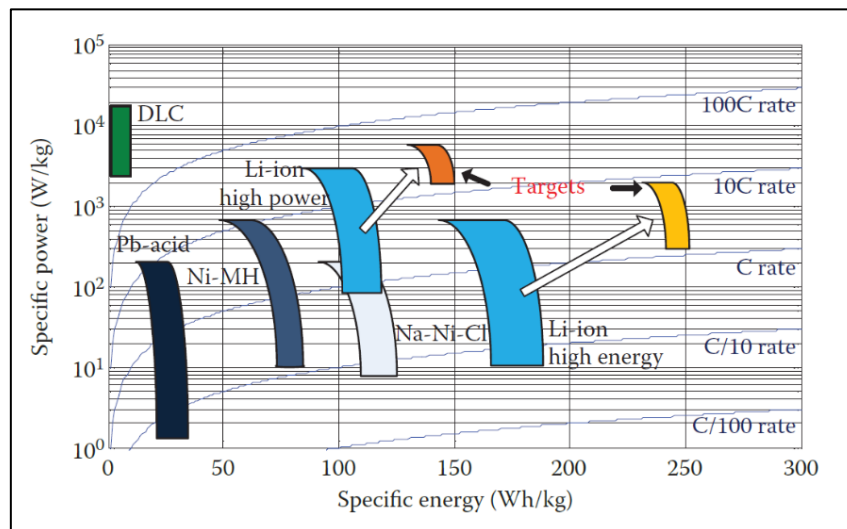


Figure 1.1: Comparison in terms of specific power and specific energy among different ESSs. The acronym DLC does not refer to an electrochemical solution, but to the double-layer capacitors [2]. Source: [a].

Chief among these problematic questions is certainly the high cost of Li-ion battery packs (500-2500 \$/kWh [2]), who makes these vehicles be more expensive than those equipped with traditional propulsion. Besides this first aspect, there are also the limited amount of km provided in pure electric mode, that can be considered proportional to the energy density of the battery (typically around 160-180 Wh/kg per Li-ion batteries [2], figures 1.1 and 1.2) and the evident degradation of battery

performances (battery aging) throughout its life. However, with respect to the first main issue, the governments of several countries [1,3,4], with Norway to the first place, constantly propose subsidies that make the actual final price rather competitive. Furthermore, as far as hybrid electric powertrains are concerned, their combined nature solves the autonomy problem that, at present, characterized the majority of electric vehicles. Hence, as regards HEVs (hybrid electric vehicles), it mainly remains crucial the question related to battery aging.

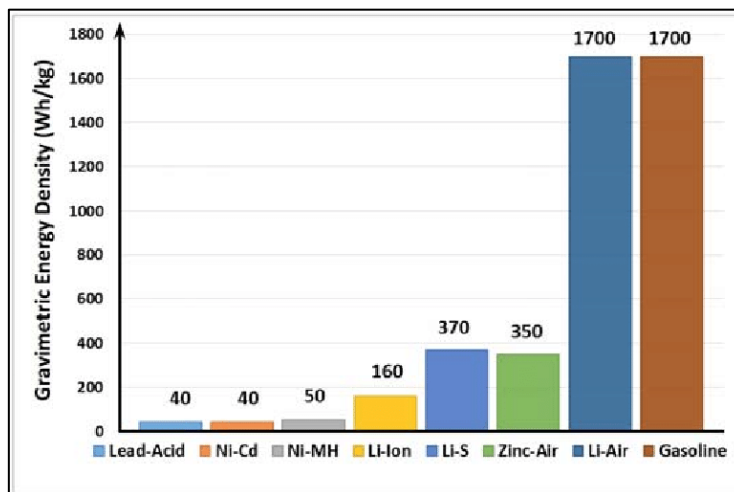


Figure 1.2: Specific energy density of different typologies of batteries compared to gasoline. Source: [b].

1.1. Introduction to Battery Aging: Calendar and Cycle life

Fundamentally, it is possible to distinguish two types of battery aging, namely calendar aging and cycle aging. Since these two processes are normally quantify in terms of permitted battery lifetime (in automotive applications generally expressed in terms of years or of total amount of km travelled by the vehicle before battery breakdown), it is preferred to use the concepts of calendar and cycle life [2]. With respect to the first one, it can be interpreted as the total period of time a battery can be stored before it “expires”; therefore, it is related to the chronic degradation (due to chemical side reactions) that naturally affects batteries regardless of the employment. However, the speed of this deterioration process is not always the same, but it is largely influenced by the values of temperature and battery SOC (state of charge) that characterized the storage [2,5]. Actually, as far as the HEVs are concerned, except for the cases of extreme climate conditions [6], the cycle life, that is related to the aging

occurring during effective battery utilization, is normally the most critical aging aspect. In particular, this second type of aging depends on the operating conditions [5]. In fact, factors as C-rate, DOD (depth of discharge) and battery temperature overwhelmingly influence how rapidly the battery EOL (end of life) is attained. However, defining the EOL is not a trivial operation. Indeed, the EOL is not simply related to the effective maximum number of charging-discharging cycles a battery can supply, but to a more subtle concept of battery charge throughput (often expressed as Ah-throughput and better specified in subchapter 4.3. of this paper). In fact, the total value of cycles loses relevance if the maximum capacity (that can be measured in both Ah and Wh) manageable by the battery considerably decreases after a certain number of cycles. In particular, with respect to the automotive employment, the progression of the battery towards its EOL, that is normally monitored by the battery SOH (state of health, described in 4.3 *Throughput-Based Battery Capacity Fade Model* and equal to 1 for a brand-new battery), ends when the battery reduces its initial nominal capacity by a percentage of 20% (that corresponds to $SOH=0$) [2]. This simply means that, even if the battery was still able to realize cycles, it is considered obsolete since no more able to fulfil its task from an energy storage point of view.

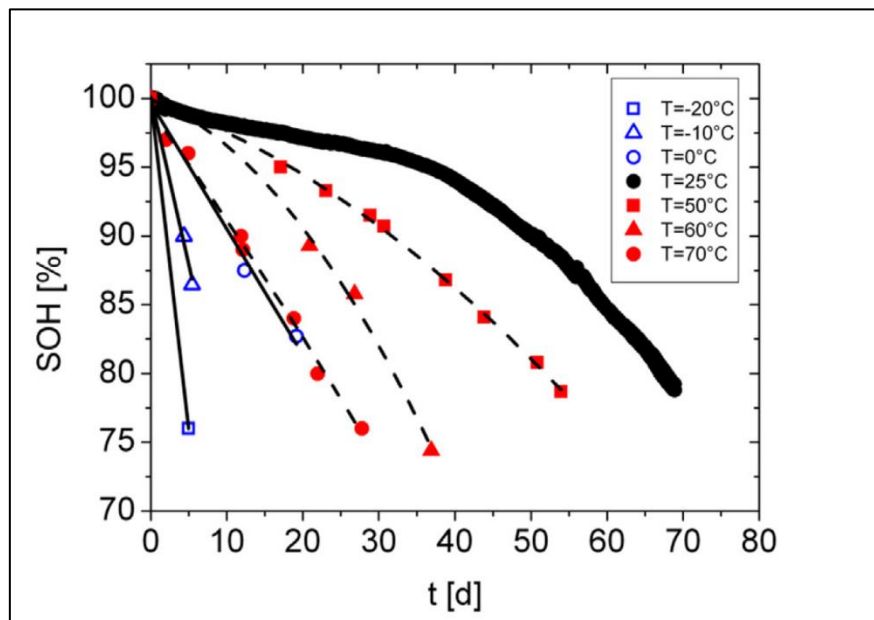


Figure 1.3: Temperature influence on SOH variation over time for a NMC:LMO/graphite Li-ion cell under unitary C-rate. Source: [c].

With respect to the chemical processes that cause this progressive capacity loss in Li-ion ESSs, they are the growth of SEI (solid electrolyte interface/interphase) layer on the anode, which occurs mainly at high temperatures [5,7] (i.e. above the ideal thermal range of battery employment 15-35°C [7]), and Lithium plating [7,8], again at the anode, principally at low temperatures (i.e. below the previous thermal range). Since both phenomena subtract Li-ion from the electrolyte, it follows that outside of the 15-35°C range the battery capacity fades faster (figure 1.3).

However, these chemical processes (especially SEI thickening) can also occur between 15°C and 35°C [8,9], with rates that normally vary with the values of C-rate, DOD swing and, unexpectedly, temperature as well. In fact, as it will be specified in subchapter 4.3., while remaining in the ideal battery thermal range (15-35°C), the temperature has still a notable impact. Finally, it is important to specify that, even if these chemical processes are common to all types of Li-ion batteries, which differ among them in the electrodes materials (mainly in the cathode ones, since the anode is commonly made of LiC_6 [2]), the respective rates and impacts of the different factors are not the same. Therefore, the cycle life model referring to a particular Li-ion cell (which is the fundamental element that constitutes a Li-ion battery pack and can be of different shapes: cylindrical, prismatic and pouch) cannot be shifted to another one.

1.2. Cycle Life Evaluation by means of Quasi-Static Vehicle Models

As it will be specified in the following chapter of this paper (2. *State of the Art*), the issues related to the cycle life of HEVs batteries are and continue to be largely explored. In particular, those works that include the aging aspect in the implementation of optimized EMSs (energy management strategies, figure 1.4), by means of the simulations of one or more quasi-static vehicle models, are of great interest since the battery is evaluated under realistic conditions of use. Nevertheless, in these works, if on the one hand both the DOD and the C-rate changes over time are commonly evaluated in an accurate manner and, therefore, their realistic impact on battery aging is precisely estimated, on the other hand the thermal influence is often simply qualitative. In fact, it is normally asserted that the battery is equipped with a cooling/heating system that maintains its temperature fixed at a specific value. Obviously, this hypothesis is legitimate, but could lead to an underestimation of battery aging. In fact, even if the battery is equipped with a BTMS (battery thermal

management system), its temperature will be always deeply dependent on ambient temperature and conditions of use.

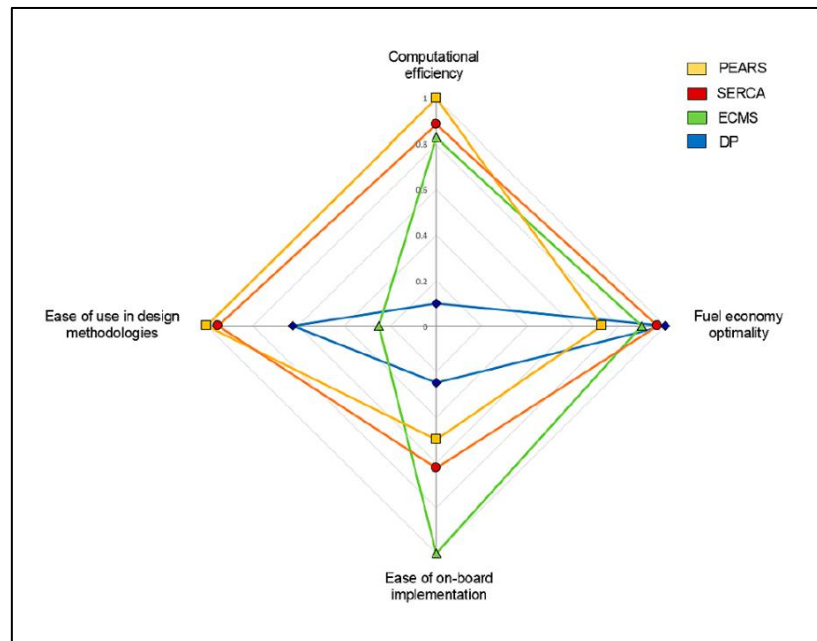


Figure 1.4: Comparison between commonly used HEVs EMSs. Source: [d].

1.3. Objectives

In consequence of what just exposed, the contribution this work would like to make is to describe the realization of a simple thermal model of HEV battery, including plausible associated cooling and heating plants, in a way that the evolution of battery lumped-temperature, throughout the simulation of several driving missions, is evaluated and, as a consequence, the thermal impact on the aging process is quantified. Finally, the acquired thermal information is employed actively in order to perform an optimization aimed at guaranteeing a sufficient duration of battery life in different cases of boundary conditions and uses; obviously, still aiming at fuel economy. Notably, a PSO (particle swarm optimization) has been implemented.

In order to achieve the aforementioned purpose, it has been realized a quasi-static plug-in hybrid vehicle model in *Simulink*. For the uninitiated, *Simulink* is a software created by *MathWorks*[®] and designed to simplify multidomain simulation and Model-Based design by means of block diagram implementation [10]. The fact *Simulink* can work coordinately with *MATLAB* environment makes this software an extremely powerful device. Its possible applications are wide, but with respect to its

employment in this work, a fixed-step solver (*ode5*), with a fundamental sample time of 0.1 seconds, has been adopted.

1.4. Jeep® Renegade 4xe

As far as the vehicle modelled (described in the following chapter 3.) is concerned, it was inspired by the *Jeep® Renegade 4xe* (figure 1.5). Together with the *Jeep® Compass 4xe*, the *Renegade 4xe* is the first *Jeep®* hybrid vehicle presented by *FCA* [11].



Figure 1.5: Jeep® Renegade 4xe. Source: [e].

The powertrain designed for these two models, by adopting a parallel-through-the-road configuration, combines the current trend of reducing the environmental impact of transportation with continuous research in driving performances improvement (such as a more sophisticated four-wheel drive). In fact, it is equipped with an internal combustion engine (1.3-liter, four-cylinder, turbo petrol engine [11], from now on indicated with the acronym ICE), acting on the front axle, and two electric motors (permanent magnet), one in configuration P4 (at the rear axle) and one in configuration P0 (from now on indicated respectively with MGP4 and MGP0), that allow the *Renegade 4xe* to travel in hybrid mode and, for an average range of 50 km (according to *NEDC* cycle), in full-electric. This has been made possible because, besides the conventional 12V battery, a HV (high voltage) battery pack is present (11.4 kWh, 400 volt, Lithium-ion, nickel-manganese-cobalt [11]). With respect to this

work, the range of variation of the HV battery SOC has been placed between a maximum value of 0.95 and a minimum one of 0.20. Moreover, both electric motors can work as generators, making it possible to perform features as, for example, regenerative braking.

Before moving on, it is necessary to specify that no official detailed information about the actual *Renegade 4xe* operating modes or components was available for the realization of this work. In fact, the model realized has been implemented starting from public *FCA*'s data about the vehicle [11-15]. Consequently, all the results obtained in this paper derive from the modelling of reasonable replacements of the unknown *Renegade 4xe* items, according to proven methodologies available in literature [16,17] that later, when effectively used, are briefly described.

1.5. Thesis Outline

Finally, the structure of this thesis can be revealed. Besides this introductory section, the paper is organized in 7 additional chapters. The successive chapter 2. *State of the Art* comments the main studies at the basis of this paper. For the sake of clarity, not all the references are mentioned in this chapter, but only those considered fundamental for the comprehension of the purposes of this work. With respect to the other sources, they are commented throughout the paper at the appropriate time. Chapter 3. *Jeep® Renegade 4xe Quasi-Static Model* introduces, instead, the *Simulink* model of the powertrain and explains its operation. In particular, a reasonable simple default RB (rule-based) controller, tasked to manage the alternance among the possible driving modes provided by the *Renegade 4xe*, which are defined by another RB controller (indicated as low level one, in order to differentiate it from the previous one, intuitively dubbed high level RB controller), is introduced. Specifically, this initial high level controller (as EMS) conciliates the preference of the driver (who can select the driving mode he/she prefers) with the current driving conditions according to the requested tractive power and the battery SOC; hence, without taking into account, at this initial stage, battery aging aspects. Afterward, the following section 4. *High Voltage Battery Model* describes the models employed for reproducing the HV battery from an electric, a thermal and an aging point of view. With respect to chapter 5. *Model Performances and Sensitivity Analysis*, the results obtained by simulating the quasi-

static vehicle model on several driving missions and with different boundary conditions, moreover without the intervention of the BTMS, are shown and the effectiveness of the default EMS (initial high level RB controller) is judged from a point of view related to the battery aging. In particular, an optimization of the operation of the cooling system together with a different management of the possible driving modes turns out to be necessary. Consequently, section 6. *PSO Implementation* illustrates how the PSO has been applied to the considered thermal question in order to guarantee a sufficient duration of battery lifetime (expressed in terms of km), together with a satisfying fuel economy. The results obtained from the optimization are then commented in chapter 7. *Calibration Results* and a new high level RB controller (indicated as optimized one) is proposed. Finally, in chapter 8. *Conclusions*, the overall outcome of the thesis is resumed and new potential research works are proposed.

2. State of the Art

As it has been highlighted in the overview by Anselma and Belingardi (2019) [18] about the past, the present and the future role of HEVs, this branch is now (2020) passing through a fundamental development phase. This is widely proven by the number of published papers about this topic, that has recently recorded an exponential increase (figure 2.1). In particular, although the related possible areas of research and development are wide, the battery aging topic raises great interest. Furthermore, it is possible to observe from the related literature that the last ten years have been a period extremely flourishing for the afore-said theme.

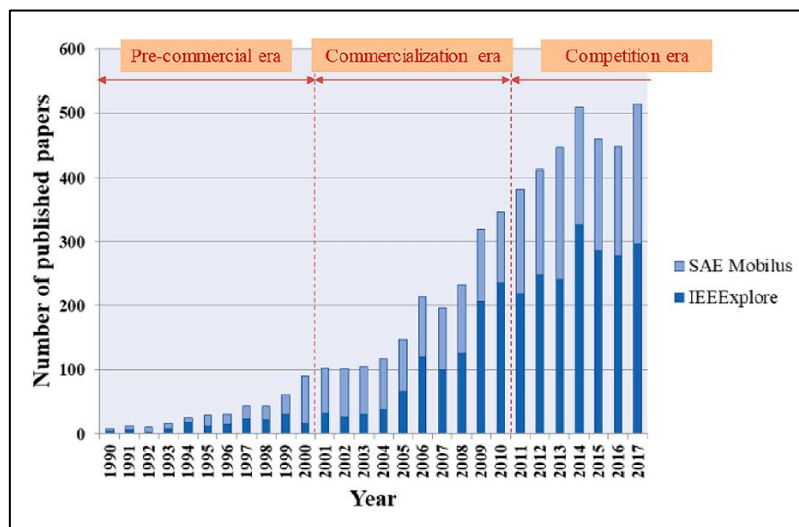


Figure 2.1: Number of papers published per year about HEVs from 1990 to 2017. Source: [d].

2.1. Capacity Fade Models

However, there are some pioneers that must be mentioned. In particular, the trailblazing considerations contained in the work of Bloom et al. (2001) [5] are still at the basis of current research. In fact, the approach proposed for the evaluation of

battery cycle life evolution (caused by SEI growth) over time under different constant operating conditions, who takes inspiration from the Arrhenius' gas equation, is a point of reference in the evaluation of battery capacity fade. Nevertheless, the range of temperature explored by Bloom is placed between 40°C and 70°C; therefore the related model (obtained by means of an empirical fitting of the data) is not able to evaluate cycle life evolution when the SEI growth is not the principal cause of battery capacity fading (i.e. at low temperatures).

More recently, another fundamental contribution has been made by Wang et al. (2011) [9], whose impressive operation of experimentation has flown into a precise life model, inspired by Bloom's work, of the A123 26650 cylindrical cell (LiFePO₄ based) [19]. Differently from Bloom's cycle life model, the evolution of capacity fading evaluated by Wang is no more expressed in terms of time, but by using the Ah-throughput, a parameter that is related to the overall amount of charge manageable by the battery throughout its life (better defined in subchapter 4.3. *Throughput-Based Battery Capacity Fade Model*) and, therefore, can be considered proportional to the life duration in terms of time.

Consequently, it is preferable to speak about throughput-based battery capacity fade model. In particular, this typology of capacity fade models allows the evaluation of the Ah-throughput expected by the battery when it is exposed, during its life, to different, but constant, conditions of use (i.e. battery temperature, C-rate and DOD swing).

Although Wang's experimentation was conducted on a range of temperature within -30°C and 60°C, the life model obtained, that results valid for the A123 26650 cell only, was able to depict the capacity fade evolution for temperatures between 15°C and 60°C. In fact, the cells cycled at -30°C broke down very quickly whereas those at around 0°C were governed by other aging mechanisms (i.e. mainly related to Li plating phenomenon).

As a consequence, similar to Bloom's work, Wang's model is not able to evaluate cycle life evolution at low temperatures.

With respect to this work, although the Li-ion cylindrical cell examined by Wang is different from the type used in the *Renegade 4xe*, that is a LiNiMnCoO₂ (NMC) cell [11], the great quantity of information available in literature about the A123 26650 cell (figure 2.2), together with the really poor public data about the authentic one, has

pushed the authors of this paper to model the HV battery as a structured assembly of A123 cylindrical cells, obviously with the constraint of obtaining overall characteristic values as close as possible to the real ones, i.e. 11.4 kWh of nominal capacity and 400 V of nominal voltage.



Figure 2.2: LiFePO₄ cylindrical cell (ANR26650M1B) by A123 Systems. Source: [f].

Once introduced the expedient of resorting to the use of A123 26650 cell, it is possible to move to the analysis of the methods that can be found in literature for applying Wang's throughput-based battery capacity fade model to more realistic cases, in which the battery does not operate under constant conditions.

Particularly interesting is the work of Ebbesen et al. (2012) [20], in which the concept of SOH is successfully adopted for supervising the state of battery aging during the simulation of different driving missions by means of a quasi-static vehicle model. Actually, similar considerations have been simultaneously made by Onori et al. (2012) [21], but by introducing a severity factor in place of the SOH. Consequently, with respect to this paper, a combination of these last two approaches by Ebbesen and Onori has been used for monitoring battery aging.

As far as the application of battery aging concepts on HEVs is concerned, a common reflection that is possible to find in the papers in question is the need for HEVs EMSs to abandon the common habit of focusing exclusively on minimizing fuel consumptions [20-22]. In fact, for example, in the work conducted by Anselma et al.

(2020) [22] it is illustrated how aiming solely at fuel economy can really compromise battery duration. Moreover, Anselma also shows that almost negligible increments in fuel consumption can really slow down the related battery aging process [22]. Therefore, it follows that the EMSs have to conduct an adequate tradeoff between fuel economy and battery lifetime.

2.2. Battery Thermal Management in Quasi-Static Vehicle Models

Therefore, overseeing the quantities affecting cycle life (battery temperature, C-rate and DOD swing) becomes essential. However, as already mentioned in chapter 1. *Preface*, in current literature the battery temperature, during driving missions simulations, is normally considered constant or, in other cases, its evolution is controlled by cooling conditions that difficulty are feasible on HEVs [20-22]. Moreover, from the portion of literature that has been consulted for this work, it does not arise a BTMS whose operating modes were directly calibrated on guaranteeing an acceptable value of battery lifetime (in terms of total amount of travelled km before battery EOL) during the simulation of real employment of HEVs. In fact, the BTMSs are normally set in order to maintain the temperature of the battery within appropriate boundaries (normally, the already mentioned 15°C and 35°C [7]). However, still remaining between these thresholds, the variation of battery life duration due to thermal aspect, as it will be shown later (figure 4.7 in subchapter 4.3.), remains remarkable. Hence, this paper wants to focus on the impact of thermal management on battery life during plausible real use of HEVs.

As a consequence, it becomes basic to suitably model, from a thermal perspective, the battery. In literature, a wide range of valid options is available, each one with its strengths and weaknesses. With respect to the simplicity of implementation in *Simulink*, together with a sufficient precision, the lumped-parameter thermal models are the most appropriate. Among these, the solution proposed by Lin et al. (2014) [23], in which the battery is equipped with two temperatures (surface and core), is particularly interesting. However, the consequent improvement in depicting the battery thermal behavior, in comparison to single-state thermal models (characterized by one only battery temperature), is not very significant (especially because of the other approximations normally made in this type of works, as specified

in subchapter 4.2.1. *Air Cooling System*). Moreover, it is less efficient from a computational point of view. Therefore, a single temperature lumped-parameter model has been chosen for representing the battery thermal behavior. Afterward, the cooling system to install on the vehicle can be elected. As shown in the paper by Janarthanam et al. (2017) [24], the main typologies of cooling systems employed on HEVs are two: those based on the active use of atmosphere air (potentially cooled down) and those equipped with a closed cooling circuit traveled by a solution of water and ethylene glycol (normally 50%-50%). If the first ones are cheaper and simpler, the second ones are surely more efficient in extracting thermal power from the battery. For the sake of simplicity, taking inspiration from the work of Han et al. (2018) [25], an air cooling system exploiting cabin air has been adopted. Before proceeding beyond, it must be specified that, although the self-imposed variation of battery temperature is also related to entropy changes, as quantified by De Vita et al. (2017) [26], in this work it has only been considered the main contribution of Joule's heating, as it is normally done [26].

However, designing exclusively a cooling plant is not sufficient. In fact, as already mentioned, low temperatures affect battery life as well. With respect to A123 26650 cell (but similar argumentations can be conducted for other types of Li-ion cells), although in literature is not present yet a precise cycle life model for low temperatures, the related degradation is well known [8,9]. Therefore, the battery must also be equipped with a heating system, that normally operates for preheating the battery before its utilization. Nevertheless, even if the battery is preheated, it may be necessary to supply heat during its operation as well [7]. With respect to this work, as heating system it was adopted a solution similar to that proposed by Jaguemont et al. (2016) [6], later exposed in 4.2.2. *Heating Pads System*.

2.3. Particle Swarm Optimization

Lastly, as already revealed, a PSO has been employed for optimizing the management of the cooling system operation and of the RB EMS. In particular, the version proposed by Clerc and Kennedy in 2002 and available as a *MATLAB* script on *Yarpiz* website (2020) [27] has been adapted to the necessities of this work.

Although the PSO is better analyzed in chapter 6. *PSO Implementation*, it can be useful to the reader if its main characteristics are introduced now. Consequently, PSO is an optimization algorithm formulated by means of a simple mathematical model and based on the social behavior, observed in nature, of birds flock, fish school or group of other organisms that live in community (figure 2.3). A really interesting aspect about this metaheuristic (advanced framework that sets the strategies to implement heuristic optimization algorithms) is that the employment of different individuals allows the group to reach a global intelligence far superior than that of a single component. Moreover, one of the reasons that makes this algorithm really popular is that PSO can be simply and successfully employed for a wide variety of different problems, including that in question.



Figure 2.3: Flock of birds, whose behavior is at the basis of PSO. Source: [g].

3. Jeep[®] Renegade 4xe

Quasi-Static Model

Although the introduction of more detailed modelling methods over the years, the QSA (quasi-static approach) is still largely used in HEVs design/analysis due to its high computational efficiency [18]. However, its backward approach implies that the usual cause-and-effect relationship of dynamic systems is inverted [28]. This aspect does not only imply that speeds are not calculated from forces, but also that the functioning of all components, with motors first and foremost, is modelled in a quasi-static way. Hence, by adopting the QSA, the model is normally devoid of any differential equations to solve and, consequently, the computational speed is high, but the collection of information about the drivability of the vehicle is extremely limited [28]. Nevertheless, at the moment, this approach seems to be still the most valid alternative [18].

With respect to this paper, a modified QSA has been adopted. In fact, as in the forward-facing approach [28], the driver is modelled as well. This expedient solves, therefore, the dynamics concerning the relation between forces and speeds. However, for simplicity and differently from the authentic forward-facing approach, the motors have been modelled in a quasi-static way by means of lookup tables.

3.1. Steady-State Models of Powertrain Motors

As already highlighted in subchapter 1.4. *Jeep[®] Renegade 4xe*, no public specific data about the *Renegade 4xe* motors (here indicated as ICE, MGP4 and MGP0) are available. In fact, all the related characteristics provided by *FCA* about the two power versions commercialized (190 *hp* and 240 *hp*) are collected in table 3.1 [29] and, as it can be inferred, they are not sufficient for modelling precisely these components.

<u>Motors technical specifications</u>		<i>190 hp</i>	<i>240 hp</i>
<i>ICE</i>	Maximum power (hp @ RPM)	<i>130 @ 5500</i>	<i>180 @ 5750</i>
	Maximum torque (Nm @ RPM)	<i>270 @ 1850</i>	<i>270 @ 1850</i>
<i>MGP4</i>	Maximum power (hp @ RPM)	<i>60 @ 4000</i>	<i>60 @ 4000</i>
	Maximum torque (Nm @ RPM)	<i>250 @ -</i>	<i>250 @ -</i>
<i>MGP0</i>	Maximum power (hp @ RPM)	<i>- @ -</i>	<i>- @ -</i>
	Maximum torque (Nm @ RPM)	<i>- @ -</i>	<i>- @ -</i>

Table 3.1: Technical specifications provided by FCA about the motors installed on the two versions of Renegade 4xe (respectively 190 hp and 240 hp) [29].

As a consequence, the related quasi-static models adopted in this work do not correspond exactly to the real motors installed on the *Renegade 4xe*, but they take inspiration from the data in table 3.1 by reasonably integrating the absent information. In particular, in order to obtain the corresponding lookup tables, it has been used a procedure analogous to the one employed in the already mentioned paper by Anselma [22]. Consequently, with respect to the ICE used in this work (which corresponds to the 130 hp version in table 3.1), its model is obtained by means of the methodology implemented in *Amesim* by Alix et al. (2015) [16]. In particular, one or two-dimensional lookup tables have been obtained for quantify the maximum possible ICE torque (as a function of ICE speed, figure 3.1), the ICE friction torque (again as a function of speed, figure 3.2) and the BSFC map (brake-specific fuel consumption, as function of both ICE speed and torque). Afterward, the BSFC map can be easily converted in a fuel table, in which the consumption rate $m_{fuel}(\frac{g}{s})$ is expressed as function of ICE speed and torque. This new two-dimensional lookup table allows the realization of two others, one for mapping the ICE efficiency (by using the fuel lower heating value $LHV=43740 \frac{J}{g}$, figure 3.3) and one for evaluating the

OOL (optimal operating line) of the ICE (figure 3.4), that is the set of best combinations of torque and speed for the ICE in question.

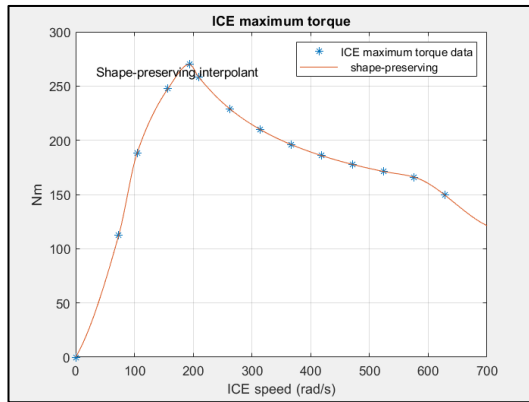


Figure 3.1: ICE maximum torque.

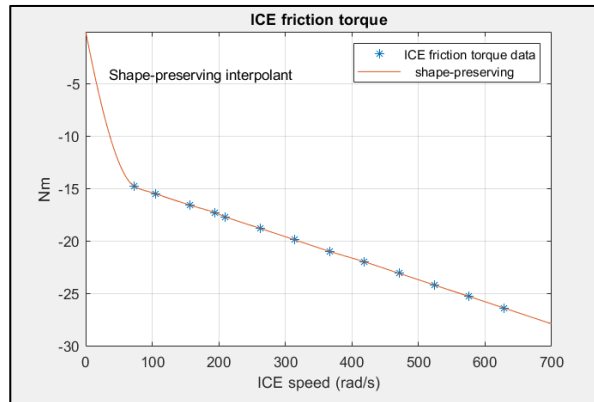


Figure 3.2: ICE friction torque.

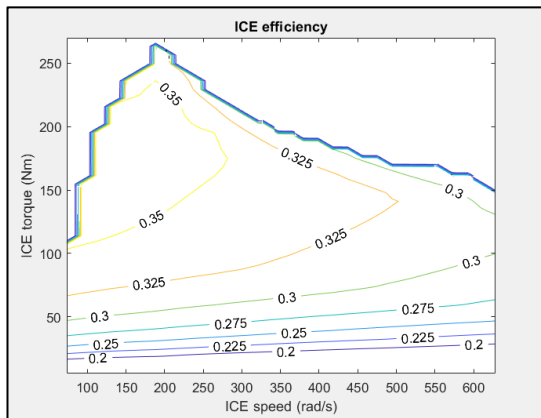


Figure 3.3: ICE efficiency map.

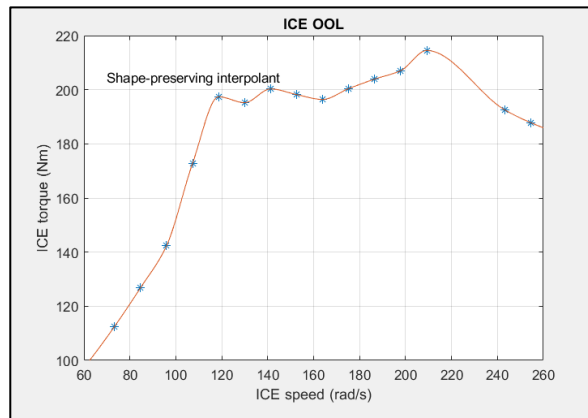


Figure 3.4: ICE optimal operating line.

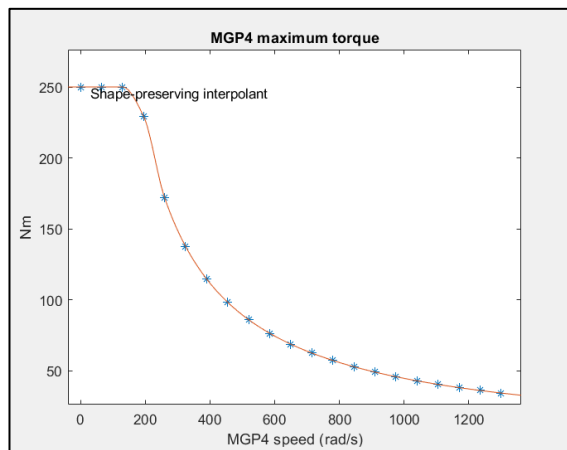


Figure 3.5: MGP4 maximum torque.

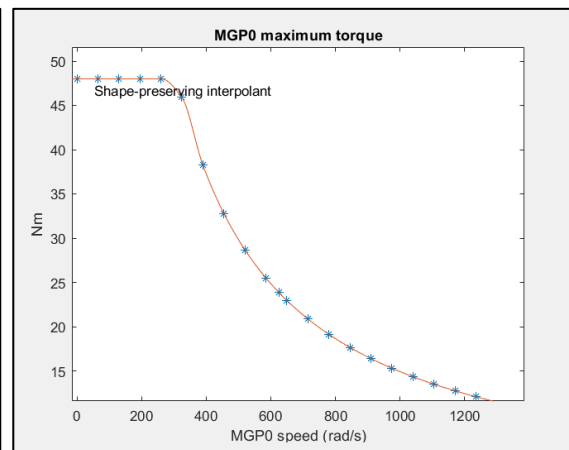


Figure 3.6: MGP0 maximum torque.

Conversely, with respect to both the electric motors, the lookup tables of maximum torques (as function of motor speed, figures 3.5 and 3.6), together with the respective maps of power losses (as function of both speed and torque, figures 3.7 and 3.8) have

been obtained following a procedure analogous to that proposed by Le Berr et al. (2012) [17].

Therefore, the afore-said lookup tables have been used in the *Simulink* vehicle model for evaluating the operation of the motors (whose resulting characteristics are collected in table 3.2) and computing both the consumptions of electric energy and fuel throughout the considered driving missions.

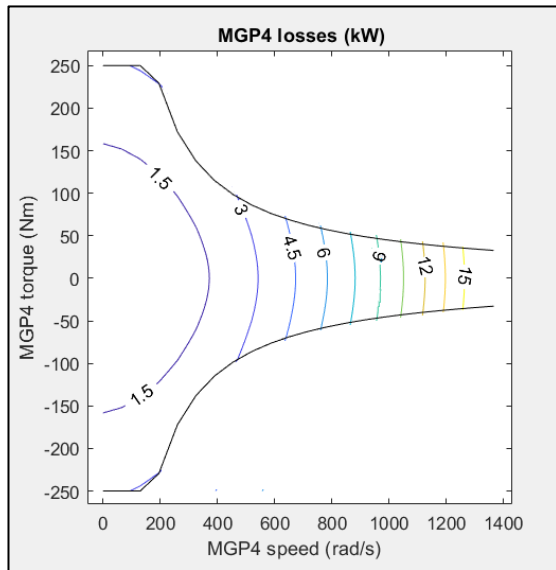


Figure 3.7: MGP4 power losses.

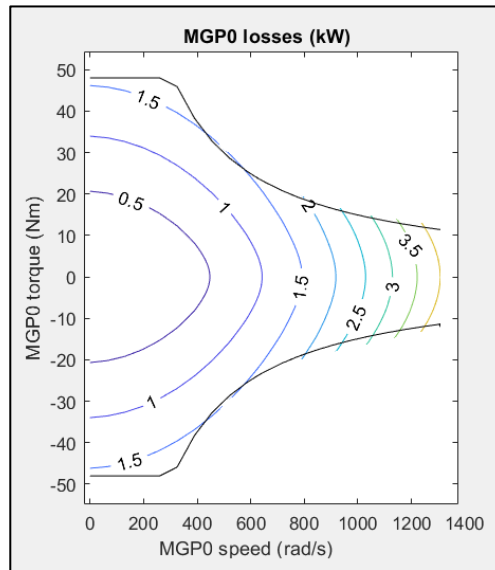


Figure 3.8: MGP0 power losses.

<u>Motors modelled technical specifications</u>		<u>190 hp</u>
<u>ICE</u>	Maximum power (hp @ RPM)	130 @ 5500
	Maximum torque (Nm @ RPM)	270 @ 1850
<u>MGP4</u>	Maximum power (hp @ RPM)	60 @ >1240
	Maximum torque (Nm @ RPM)	250 @ <1240
<u>MGP0</u>	Maximum power (hp @ RPM)	20 @ >2480
	Maximum torque (Nm @ RPM)	48 @ <2480

Table 3.2: Technical specifications of the motors employed in the model implemented.

3.2. Vehicle Free Body Diagram [2]

An important aspect that must be specified before moving on is that all the formulae present in this subchapter, as well as those in the rest of the paper (except for the PSO theory in chapter 6. *PSO Implementation*), are expressed in terms of continuous time for greater clarity. However, in *Simulink*, they are solved in a discrete way, with a sample time of 0.1 seconds.

It is common knowledge that the main resistances to the vehicle motion are the aerodynamic drag, the rolling resistance and the grading resistance. However, the grading resistance, which can also convert itself, in case of a descent, into a tractive force, is normally not considered in quasi-static simulations since the standard driving cycles (commonly used) are extended on flat paths. In rare cases, a fixed slope is considered, but this stratagem is not very interesting since the grading resistance remains constant all along. With respect to this work, besides some common driving cycles, 4 real-world driving missions (precisely described in chapter 5. *Model Performances and Sensitivity Analysis*), in which the variation of altitude along the road has been measured and recorded, have been simulated as well. Consequently, during the simulation of these driving missions, the effect of realistic grading forces can be evaluated.

On the contrary, an aspect that has not been considered in any of the driving missions, since judged of little significance, is the vehicle proceeding backwards.

A (N)	94.0354
B (Ns/m)	3.805027
C (Ns^2/m^2)	0.47610668

Table 3.3: Road load coefficients [22].

As far as the evaluation of the resistive forces is concerned, the aerodynamic drag F_{aero} (N) and the rolling resistance F_{roll} (N), together with some miscellaneous terms incorporated in F_{misc} (N), have been computed by using the following equation based on the road load coefficients A, B and C [22] (reported in table 3.3):

$$F_{aero} + F_{roll} + F_{misc} = A \cdot (v \neq 0) + Bv + Cv^2 \quad (1)$$

where v (m/s) is the longitudinal speed of the vehicle, that is supposed to be only positive or null (no backwards motion).

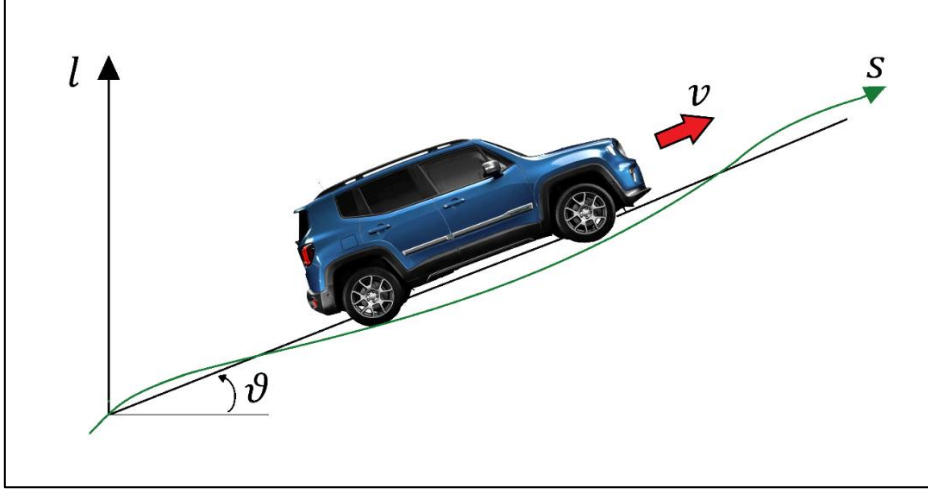


Figure 3.9: Vehicle proceeding on a slanting road. The angle θ is positive for uphill roads and negative for downhill ones.

With respect to the grading resistance F_{grad} (N), it is proportional to the sine of the road slope angle ϑ (rad). However, since ϑ changes continuously and, moreover, it can hardly be measured directly, it is preferable to express the sine as the variation of the altitude l (m) divided by the portion of related space travelled s (m) (figure 3.9). Therefore, F_{grad} can be calculated as follows:

$$F_{grad} = m_{tot,veh}g\sin\vartheta = m_{tot,veh}g\frac{dl}{ds} \quad (2)$$

in which g (m/s^2) is the gravitational acceleration and $m_{tot,veh}$ (kg) is the total mass of the vehicle, that can be expressed as:

$$m_{tot,veh} = 1768kg + 100kg \cdot n_{pass} \quad (3)$$

where n_{pass} is the number of passengers and can vary between 1 (only driver) to 5.

Therefore, the total resistive force $F_{res,tot}$ (N) can be easily obtained:

$$F_{res,tot} = F_{aero} + F_{roll} + F_{misc} + F_{grad} \quad (4)$$

Then, by introducing the tractive force F_{tract} (N), provided at the wheels by the powertrain, and the inertia of the vehicle, that can be approximated to the simply total mass of the car $m_{tot,veh}$ (therefore, without considering the contribution of the rotating parts), the equilibrium equation of the system can be written as:

$$m_{tot,veh}a = F_{tract} - F_{res,tot} \quad (5)$$

where a (m/s^2) indicates the longitudinal acceleration of the vehicle. It is important to specify that, although the name, F_{tract} can also be a braking force (during notable deceleration).

3.3. Driver Model

How equation (5) is used plays a fundamental role in the qualification of the vehicle model. In fact, as revealed at the beginning of this chapter, the classic QSA is characterized by a distortion of the cause-and-effect principle that computes, at each time step, the force requested to the powertrain from the speed/acceleration information provided by the considered driving mission. Therefore, according to this method, the inputs of equation (5) would be a and v (this latter is necessary for calculating $F_{res,tot}$), whereas the output would be F_{tract} . Although this expedient really hastens the resolution of the simulations and the implementation of the model, its logic is not realistic and can be easily solved, without introducing notable complications, by modelling the driver. Effectively, what the driver does in traditional driving (but autonomous one follows the same principles) is to act on the pedals in order to achieve a desired velocity v_{des} (m/s), that must not be confused with the actual speed v . In particular, v_{des} can be associated to the speed data of the contemplated driving mission. Hence, the logic process normally conducted by the driver is:

1. to evaluate the desired speed v_{des} (in these simulations it is directly furnished by the driving mission data, but in real world it is related to the road signage, the traffic situation, etc.);

2. to compare it with the current v ;
3. to act on pedals in order to reach v_{des} , i.e. to ask the powertrain for a tractive/braking force;
4. to ascertain the new v and to compare it with the objective one;
5. to correct the pedals position in order to reduce the error between the two speeds.

Actually, the process is more complex since v_{des} changes continuously. However, it is clear that the actual speed v is a consequence of the tractive force and not vice-versa. Moreover, strictly speaking, the actual speed cannot be known, but a measure of it yes. Another important aspect is that, since in *Simulink* the time is discretized, v_{des} (related to a specific instant of time) is always compared to the actual speed v referring to the previous time step. Similarly, the current total resistive force $F_{res,tot}$ is computed from equation (4) by using the speed v and the space s related to the preceding time instant.

Therefore, the driver model in *Simulink* must operate following a procedure analogous to the one exposed above. This is possible by assigning the driver's role to a PID (proportional–integral–derivative) controller.

In fact, the PID controller, exactly as the driver, requires as input the difference between the two speeds and outputs the tractive force (at the wheels) requested to the powertrain (figure 3.10).

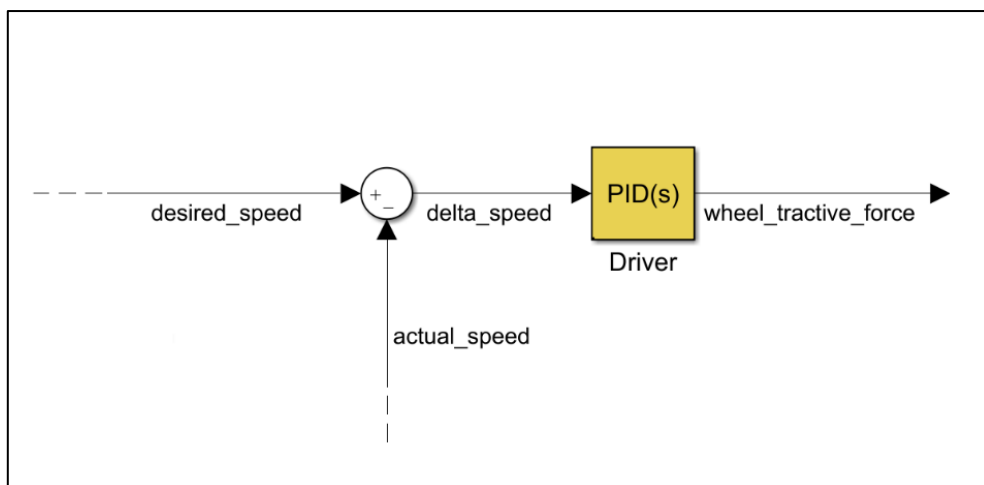


Figure 3.10: PID controller.

If the desired speed, as already mentioned, comes from the driving mission prescriptions, the actual one, v , is computed by integrating the acceleration a obtained from equation (5) (in which the considered F_{tract} is the one outputted by the PID at the previous time step) over time t (s). Consequently, by integrating v over time, it is also possible to evaluate the space travelled s , that is necessary in equation (2) for computing F_{grad} .

Entering into detail, the PID controller employed in this work was performed in the most common version of simple PI (without derivative term D or anti-windup scheme), since the results obtained by simply using these 2 gains satisfy the desired level of detail. As values of the gains, $P=3800$ and $I=150$ (with P and I in accord with *MATLAB* notation) have been used. The way to determine them was Trial-and-error, checking visually, with a *Simulink* scope block, for what pair of gains the graphs over time of the two velocities (v_{des} and v) were more similar. In addition, a control was conducted on accelerations (desired and actual) as well, arising interesting considerations later specified in 5.1. *Driving Missions*.

It is important to specify that the graphs of desired and actual quantities are desired similar, but not coincident. In fact, this difference reflects the realistic conduct of the driver, that continuously operates the pedals for reducing the distance between v and v_{des} . Obviously, the more expert is the driver, the smaller is the gap. This aspect, not present in the QSA, is well depicted by the PID controller. However, the PID generates some problems when the desired speed is the null one (vehicle at standstill). In fact, the actual speed v deriving indirectly from PID indications will not be zero, but slightly positive, or even worse, negative (figure 3.11). Obviously, this feature does not represent anymore the operating of the driver and could have an adverse impact if not corrected. For example, problems would arise in equation (1), with a consequent wrong calculation of equation (4). Therefore, for preventing an incorrect computation of $F_{res,tot}$, equation (1) can be converted into equation (6):

$$F_{aero} + F_{roll} + F_{misc} = (A + Bv + Cv^2) \cdot (v \geq 0.1 \text{ m/s}) \quad (6)$$

In this way, the effects of the little speeds (normally $< 0.1 \text{ m/s}$), due to the imprecise behavior of the PID at standstill, are neutralized.

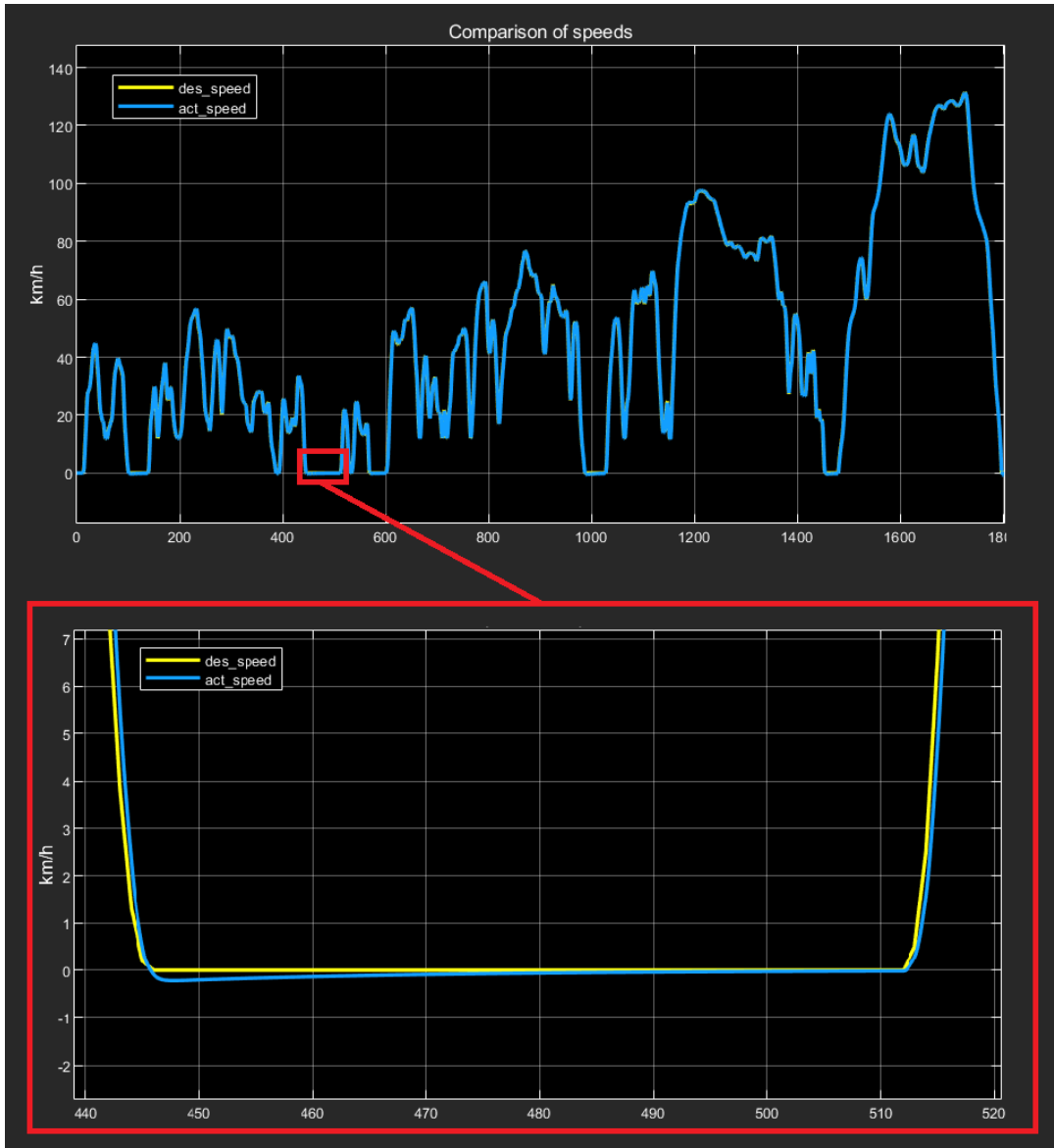


Figure 3.11: Difference between the desired speed v_{des} (in yellow, in this case deriving from the WLTP driving cycle) and the actual speed v (in blue, computed from PID indications); it can be observed that v , when supposed to be null, is instead slightly negative.

3.4. Default Rule-Based EMS

In the previous subchapter, it has been shown how the F_{tract} is specified by the PID, but no extra information about how the powertrain (figure 3.12) is supposed to furnish it was given.

In fact, once the PID controller determines the F_{tract} requested to the powertrain, this latter could provide it by differently combining the torques supplied by its motors (the ICE, the MGP4 and the MGP0) and by the brakes (not reported in figure 3.12 and only brought into play in particular cases later specified). As it can be intuitively

understood, some combinations, in certain conditions, can be considered better than others, but the benchmark of the comparison must be declared clearly. However, the discriminating factor is hard to choose since, generally, it is necessary to conduct a tradeoff between different aspects, which are likely to be clashing among them. In fact, as mentioned in chapter 2. *State of the Art*, the currently explored HEVs EMSs (both online and offline ones [18]) are tasked to manage the different components of the powertrain aiming at the optimum compromise between fuel economy and battery lifetime [20,22].

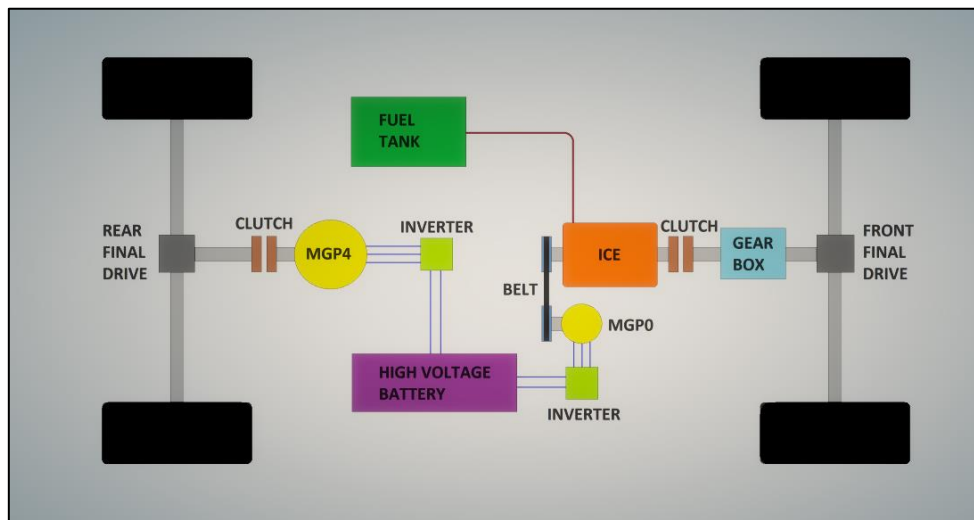


Figure 3.12: Renegade 4xe powertrain diagram (not to scale).

With respect to the different ways an EMS can be performed [18], the RB strategies are a valid and simple online supervisory option [43] and, for this reason, have been adopted in this work. Specifically, as already mentioned, two levels (high and low) of RB controllers have been implemented by taking inspiration from the public information about the EMS effectively developed in the *Renegade 4xe* (named *HCP algorithm* [11]). With respect to the low RB controller, that will remain unvaried along all the paper (therefore will not be object of the optimization conducted in chapter 6.), it concerns how the different driving modes allowed by the *Renegade 4xe* (i.e. Hybrid mode, Electric mode and E-save mode) influence the functioning of the powertrain; therefore, this controller indicates how the powertrain is managed according to the three different driving possibilities. In particular, these modes can be manually selected by the driver before or during the trip. However, there is no guarantee that

the powertrain is effectively working according to the chosen mode; in fact, the high RB controller (which will be object of the PSO) has the task of evaluating if the selected mode is feasible in the current driving conditions. Consequently, this second controller has the possibility to switch autonomously (temporarily or for longer periods) to more appropriate driving modes. Therefore, the driver has a limited decision-making power because, if he chooses a driving mode that is not suitable for a particular condition (for example, Electric mode at a very low value of SOC), the EMS, which coincides with the high level RB controller, automatically moves to a practicable one (Hybrid or E-save mode). Hence, the simple flowchart in figure 3.13 resumes this hierarchy concerning the powertrain functioning.

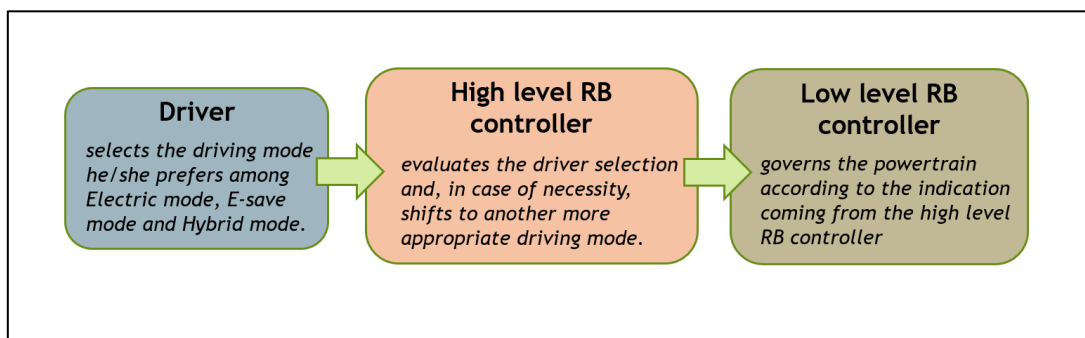


Figure 3.13: Flowchart illustrating the logic of powertrain management.

However, it is important to specify that the change between two different driving modes is not instantaneous, but requires a quantity of time (a delay) that depends on the potential change of ICE state (on and off) and that has been modelled as well in this work. Before describing more in detail these two RB controllers, it must be highlighted that, since beyond the area of interest of this paper, neither the logic related to the four-wheel drive for any value of SOC (that is guaranteed in the real *Renegade 4xe*) nor the more specific driving modes (auto, rock, etc.) or the e-coasting modality have been developed [11].

Hence, it is then possible to specify what the low level RB controller dictates for the different driving modes:

- In the Electric mode, the powertrain provides a pure electric traction by means of the MGP4 only, which is supplied by the HV battery. During decelerations, this motor works as a generator and performs regenerative braking; however,

if the battery is completely charged or the imposed braking torque is too high for the MGP4 to regenerative brake, traditional braking is employed.

- In the E-save mode, the traction is supplied mainly by the ICE, that is always switched on, except in few occasions (due to start&stop logic). In particular, the ICE normally works at its OOL (indicated by the respective lookup table), unless the tractive force requested is higher than the sum between the ICE OOL and the maximum torque from the MGPO (checked by means of another lookup table). In this last case, in fact, the ICE works above its OOL. In more rare cases, when the tractive torque requested is higher than the one resulting from the combination of the maximum torques from both the ICE and the MGPO, the MGP4 comes to the aid. Conversely, if the tractive torque is lower than the OOL, an extra torque is provided by the ICE (which, in this way, still operates around its OOL) and used to charge the battery by means of the MGPO operating as a generator. During braking, instead, the ICE is on and it performs engine braking (with fuel cut-off). This braking torque from the ICE limits the possibility of regenerative braking (performed by the MGPO and, in case of necessity, by the MGP4 as well), but it was highlighted that it is better to engine braking instead of having the ICE idling during decelerations. In the very rare situations of extremely intense deceleration or battery already completely charged, traditional braking is respectively used together or instead of regenerative one. When the vehicle is at standstill (that, because of the PID, does not corresponds to $v=0 \text{ m/s}$, but to $v < 0.1 \text{ m/s}$) and no torque is requested, the ICE is off (start&stop logic).
- In the Hybrid mode, the system works similarly to the E-save mode. Specifically, as long as the SOC is higher than 0.3, if the requested tractive torque is higher than the one corresponding to the ICE operating at its OOL, both the MGPO and the MGP4 comes to the aid. Consequently, the ICE works above its OOL only in case the contribution of the maximum torques from both the MGPO and the MGP4 is not enough. Conversely, when the OOL torque is higher than the requested one, the ICE simply works below its OOL, without recharging the battery by means of the MGPO. In case the SOC is lower than 0.3, instead, the ICE operates alone in order to limit the risk regarding the achievement of too low SOC values. Obviously, in case the requested torque is

too large to be solely provided by the ICE, both the MGP0 and the MGP4 can intervene. With respect to the regenerative braking and to the start&stop logic, considerations analogous to the E-save mode can be done for both.

As already mentioned, the driver can select the driving mode (among the afore-said) he/she prefers; however, his/her choice is sifted through the high level RB controller, who operates in the following way:

- When the Electric mode is selected, if the SOC goes below 0.30, it is performed an automatic change to the Hybrid mode in order to pass from charge depleting strategy to charge sustaining one. During the authentic Electric mode (i.e. before going below SOC=0.30), if the driving mission asks for a tractive power higher than the one that can be provided by the MGP4 at the speed in question (checked by means of the corresponding maximum torque lookup table), the powertrain will temporarily operate in Hybrid mode. In particular, specific power thresholds and delays have been set in order to prevent the ICE from being frequently switched on and off. Moreover, although the maximum speed reachable by the real *Renegade 4xe* in pure electric is declared to be of 130 km/h , in this work it was considered an upper limit of 136 km/h , above whom it is effectuated a temporary passage to Hybrid mode.
- When the E-save mode is selected, if the SOC is lower than 0.80, the battery is charged up to this value; after that, the system moves to the Hybrid mode, which is maintained up to the lower SOC of 0.70, for then moving back to the E-save mode (if still selected) and so on.
- When the Hybrid mode is selected, as long as the SOC is higher than 0.60, the vehicle proceeds in pure electric (Electric mode), coming back to Hybrid mode each time the power requested is too high to be provided solely by the MGP4. Afterward (below 0.60), unless the SOC returns above 0.80, the Hybrid mode is maintained. However, in case a SOC value of 0.25 is reached, it is performed a passage to the E-save mode, which will be maintained up to a SOC of 0.30, in order to guarantee that the minimum SOC manageable by the battery (i.e. 0.20, as it has been specified before in this paper) is not overtaken.

As it can be inferred by what mentioned above, this initial high level RB controller, that has been determined reasonably, but still arbitrarily, does not take into account aspects related to battery aging. In fact, as already highlighted, it is simply a default controller that will be optimized later. Moreover, as disclosed in *1.5. Thesis Outline*, although this work wants to focus on the thermal aging effect and aims at proposing a plausible relation among exploitation of electric power and battery temperature, before introducing thermal aspects in the EMS it has been considered useful to first simulate the vehicle model devoid of a thermal control (as this default RB controller does). Consequently, it will be possible to obtain an optimized EMS (by means of a PSO) and to perform an interesting comparison with the default one.

3.5. Transmission Specifications

Now that the default EMS has been introduced, further information can be given about how the requested F_{tract} is actually provided by the motors and, potentially, by the brakes. To do so, it is clearly better to reason in terms of torques, instead of forces. Consequently, the total tractive torque T_{tract} (Nm) requested at the wheels can be computed as:

$$T_{tract} = F_{tract}r_{wheel} \quad (7)$$

in which r_{wheel} (m) is the radius of the wheels (215/60 R16 tire) and it is reported in table 3.4. In order to explicit all the possible contributions to T_{tract} , equation (8) is used:

$$T_{tract} = T_{ICE,wheel} + T_{MGP4,wheel} + T_{MGPO,wheel} - T_{brakes} \quad (8)$$

where the terms $T_{ICE,wheel}$ (Nm), $T_{MGP4,wheel}$ (Nm) and $T_{MGPO,wheel}$ (Nm), representing the torques at the wheels provided by the different motors according to the EMS indications, can be individually null (no contribution to T_{tract}), positive (traction condition) or negative (deceleration condition), whereas T_{brakes} (Nm) is the torque supplied by the brakes and it is mainly null, but positive when traditional braking is performed. In order to pass from $T_{ICE,wheel}$, $T_{MGP4,wheel}$ and $T_{MGPO,wheel}$ to the torques T_{ICE} (Nm), T_{MGP4} (Nm) and T_{MGPO} (Nm) effectively outputted by the

motors (i.e. indicated torques), it is necessary to introduce the transmission ratios that characterize the powertrain (figure 3.12). Specifically, the components in question, reported with their transmission ratios [13,14] (whose values are collected in table 3.4), are the following:

- the rear final drive, with a ratio i_{rear} ;
- the front final drive, with a ratio i_{front} ;
- the gear box, with a ratio i_{gear} . In particular, the vehicle is equipped with a six-speed automatic transmission; therefore, i_{gear} can assume 6 different values (actually, one more if backward motion was considered);
- the belt connecting the ICE and the MGPO, with a ratio i_{belt} .

In the successive equations, for simplicity, i_{front} and i_{gear} are incorporated in one single term called $i_{front,tot}$, defined as $i_{front,tot} = i_{front}i_{gear}$. Therefore, T_{ICE} , T_{MGP4} and T_{MGPO} can be computed as follows:

$$T_{MGP4} = \frac{T_{MGP4,wheel}}{i_{rear}} \quad (9)$$

$$T_{ICE} = \frac{T_{ICE,wheel}}{i_{front,tot}} + \min \left[\left(T_{OOL} - \frac{T_{ICE,wheel}}{i_{front,tot}} \right), 0.6 \cdot T_{MGPO,max} i_{belt} \right] \cdot \left[0 < \left(T_{OOL} - \frac{T_{ICE,wheel}}{i_{front,tot}} \right) < T_{OOL} \wedge d_{mode} = e_{save} \right] \quad (10)$$

$$T_{MGPO} = \frac{T_{MGPO,wheel}}{i_{front,tot} i_{belt}} - \min \left[\left(\frac{T_{OOL}}{i_{belt}} - \frac{T_{ICE,wheel}}{i_{front,tot} i_{belt}} \right), 0.6 \cdot T_{MGPO,max} \right] \cdot \left[0 < \left(T_{OOL} - \frac{T_{ICE,wheel}}{i_{front,tot}} \right) < T_{OOL} \wedge d_{mode} = e_{save} \right] \quad (11)$$

where T_{OOL} (Nm) indicates the ICE torque related to the OOL, $T_{MGPO,max}$ (Nm) is the maximum torque manageable by the MGPO (according to the respective lookup table) whereas d_{mode} detects the current driving mode. It is interesting to observe that equations (10) and (11) appear more complex than equation (9) due to the particular feature of the E-save mode that allows the ICE to provide simultaneously torque aimed at vehicle traction and at battery recharge by means of MGPO.

Actually, each transmission ratio ($i_{front,tot}$, i_{rear} and i_{belt}) is associated with an efficiency, that has not been written in equations (9), (10) and (11) for the sake of clarity, but, obviously, must be considered. In fact, if reported in the previous equations, these efficiencies indicated by $\eta_{front,tot}$, η_{rear} and η_{belt} [15] (collected in table 3.4) would independently multiply or divide the right members of the equations depending on how the respective transmission (or combination of transmissions) is related to the left member. For example, looking at equation (9) in case of full electric driving, the only transmission brought into play is the rear final drive. During effective traction, from this transmission point of view, the T_{MGP4} is seen as a motor torque and, therefore, the only right member is divided by η_{rear} . Instead, during deceleration, T_{MGP4} is a load torque and, as a consequence, the right member is multiplied by η_{rear} . Similar considerations can be made for equations (10) and (11) as well.

r_{wheel} (m)	0.322
i_{front}	4.438
i_{rear}	10
i_{gear}	4.15; 2.12; 1.36; 0.98; 0.76; 0.62
i_{belt}	2.7
$\eta_{front,tot}$	0.90
η_{rear}	0.95
η_{belt}	0.94

Table 3.4: Radius of the wheels, transmission ratios and respective efficiencies [12-15].

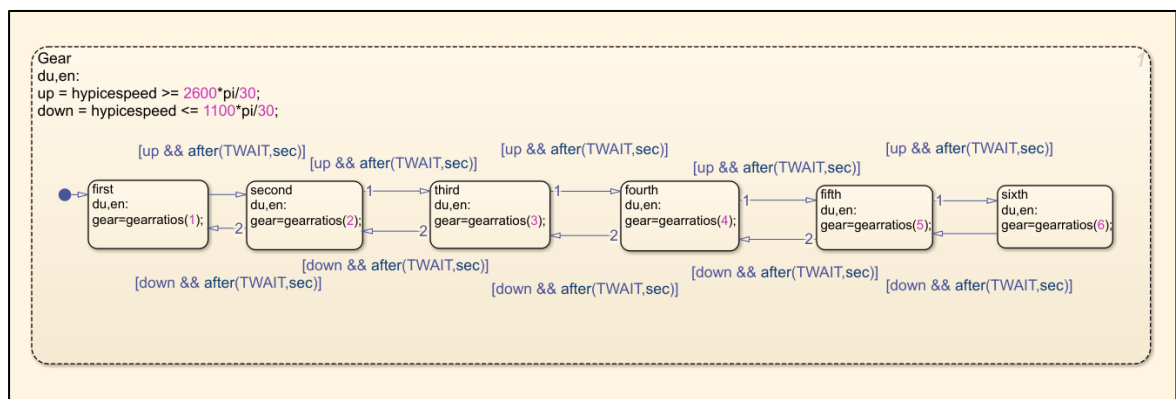


Figure 3.14: Gear logic implemented in Stateflow tool.

With respect to the model employed in this work for the selection of the suitable value of i_{gear} , it has been developed a simple gear logic (figure 3.14) in the *Simulink* tool named *Stateflow*. In particular, it realizes upshifting when the ICE speed is maintained larger than 2600 *RPM* for more than 2 seconds and downshifting when the speed goes below 1100 *RPM*, again with a delay of 2 seconds.

Obviously, equations analogous to those just written for the torques can be expressed in terms of speed. Indeed, the one corresponding to equation (7) will be:

$$\omega_{wheel} = \frac{v}{r_{wheel}} \quad (12)$$

in which ω_{wheel} (rad/s) is the angular speed of the wheels. With respect to equation (8), instead, it corresponds to:

$$\omega_{wheel} = \max(\omega_{ICE,wheel}, \omega_{MGP4,wheel}, \omega_{MGP0,wheel}) \quad (13)$$

where $\omega_{ICE,wheel}$ (rad/s), $\omega_{MGP4,wheel}$ (rad/s) and $\omega_{MGP0,wheel}$ (rad/s) can be individually null, when the corresponding motor is not taking part in T_{tract} generation (for the ICE, instead, it is possible that this motor is idling), or equal to ω_{wheel} . Finally, the relations addressed to the computation of the effective motors speed are simpler than the corresponding equations (9), (10) and (11) because neither the efficiencies nor particular features of the possible driving modes intervene in their expression. Therefore, the equations for calculating ω_{MGP4} (rad/s), ω_{ICE} (rad/s) and ω_{MGP0} (rad/s) are simply:

$$\omega_{MGP4} = \omega_{MGP4,wheel} i_{rear} \quad (14)$$

$$\omega_{ICE} = \omega_{ICE,wheel} i_{front,tot} \quad (15)$$

$$\omega_{MGP0} = \omega_{MGP0,wheel} i_{front,tot} i_{belt} \quad (16)$$

Afterward, once the operating conditions (torque and speed) of each motor are known, it is possible to evaluate, by means of the frequently mentioned lookup tables, the fuel consumed by the ICE and the electric power requested by (or supplied by, in case of generator modality) the electric motors to the HV battery, which, although is part of the vehicle model, is described in the next chapter since a fundamental element of this work.

Therefore, the following equations can be written:

$$m_{fuel} = \int_0^t m_{fuel} \dot{dt} + n_{crank} m_{crank} \quad (17)$$

$$P_{bat,MGP4} = \omega_{MGP4} T_{MGP4} + P_{loss,MGP4} \quad (18)$$

$$P_{bat,MGP0} = \omega_{MGP0} T_{MGP0} + P_{loss,MGP0} \quad (19)$$

In equation (17), $m_{fuel}(g)$ is the total quantity of fuel consumed by the ICE up to instant t , $m_{fuel} \dot{(g/s)}$ is the already mentioned consumption rate, evaluated by entering the designated lookup table with ω_{ICE} and T_{ICE} , $m_{crank}(g)$ is the quantity of fuel employed every time the ICE is cranked (equal to 0.5 g [15,22]) and n_{crank} indicates the number of occurrences, in the period $[0, t]$, in which the ICE is cranked. With respect to equations (18) and (19), instead, $P_{bat,MGP4}(W)$ and $P_{bat,MGP0}(W)$ represent the powers requested/supplied by the electric motors to the battery, whereas $P_{loss,MGP4}(W)$ and $P_{loss,MGP0}(W)$ indicates the power losses that characterize the two motors and can be obtained from the corresponding lookup tables by simply inputting, respectively, the $\omega_{MGP4} \setminus T_{MGP4}$ and $\omega_{MGP0} \setminus T_{MGP0}$ values. It must be specified that, whereas $P_{loss,MGP4}$ and $P_{loss,MGP0}$ can be only positive, the terms $\omega_{MGP4} T_{MGP4}$ and $\omega_{MGP0} T_{MGP0}$ are positive when MGP4 and MGP0 work as motors and negative when they operate as generators.

4. High Voltage Battery Model

As it has been mentioned in subchapter 1.4. *Jeep® Renegade 4xe*, the *Renegade 4xe* is equipped with two batteries: a conventional 12V battery and a HV battery pack. In the model realized, since the usage of conventional batteries is by now well-established and their operating is well known (i.e. cranking the ICE and supplying some auxiliaries), the 12V battery has not been considered. Instead, fundamental is the implementation of an appropriate model of the HV battery, since at the basis of further considerations.

In particular, as the following subchapters show, it is necessary to model the battery from three points of view: electrically, thermally and from an aging angle.

4.1. Equivalent Electric Circuit Model

In literature, different methodologies can be found in order to model batteries, namely equivalent circuit models, electrochemical models, analytical models with empirical data fitting and artificial neural networks [21]. Among these, the ECM (equivalent circuit models) results particularly simple to implement since the battery is represented as an elementary electric circuit made of voltage sources, resistors and capacitors.

With respect to this work, in order to represent electrically the A123 cell, it has been adopted an Internal Resistance Model [30], that is a particular type of ECM just made of a voltage source in series with a resistance. Therefore, each cell, to whom is associated a capacity C_{cell} (Wh) [19], can be simply represented as a voltage source OCV_{cell} (V) in series with an internal resistance R_{cell} (Ω) (figure 4.1), whose values can be obtained from the catalogue of A123 systems [19] and the already mentioned papers by Wang [9] and Ebbesen [20].

However, as it was explained in chapter 2. *State of the Art*, the A123 26650 is not the cell constituting the real HV battery of *Renegade 4xe*, but it simply substitutes the LiNiMnCoO_2 cell since this latter was characterized by the absence of a well-proven life model, that would not have allowed the argumentations conducted in this paper. Consequently, the replacement battery made of A123 cells must be obtained with the constraint of obtaining nominal values of capacity and voltage really close to the real ones, i.e. 11.4 kWh and 400 V .

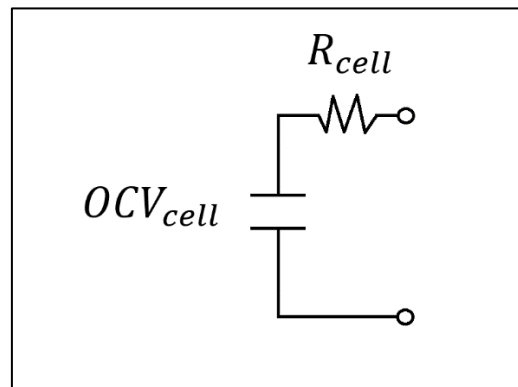


Figure 4.1: Cell equivalent electric circuit model.

More specifically, the investigated battery configuration can be extrapolated by employing the Thevenin's theorem [31]. However, before introducing this theorem, it must be highlighted that the cells parameters are not constant, but change during operation. In particular, with respect to OCV_{cell} , its value varies with the battery SOC, whereas R_{cell} depends on more factors, namely the battery SOC, the C-rate, the battery temperature and the charging/discharging condition [9,19,20]. In particular, OCV_{cell} decreases with SOC reduction whereas R_{cell} increases with SOC and/or C-rate decrease and/or cell temperature growth. Actually, also OCV_{cell} is sensitive to temperature variation, but this behavior is normally of little significance. Obviously, all these relationships are then reflected on the related battery (made of several cells of same type). In the battery *Simulink* model, all these interconnections have been taken into account by means of lookup tables deriving from literature [9,20]. Anyway, back to the application of the Thevenin's theorem, by assembling N_{tot} cells (which are considered perfectly identical) according to N_p and N_s values, that respectively represent the number of parallel branches and the number of cells in series per each

branch, it is possible to obtain the electric model of the whole battery (circuit on the left in figure 4.2), characterized by a capacity C_{bat} (Wh) calculable as:

$$C_{bat} = N_p N_s C_{cell} \quad (20)$$

However, a battery depicted in this way turns out to be rather inconvenient to use. Hence, by means of the Thevenin's theorem, it is possible to obtain an equivalent electric circuit of the battery simply composed of an equivalent voltage source OCV_{bat} (V) in series with an equivalent internal resistance R_{bat} (Ω) (circuit on the right in figure 4.2).

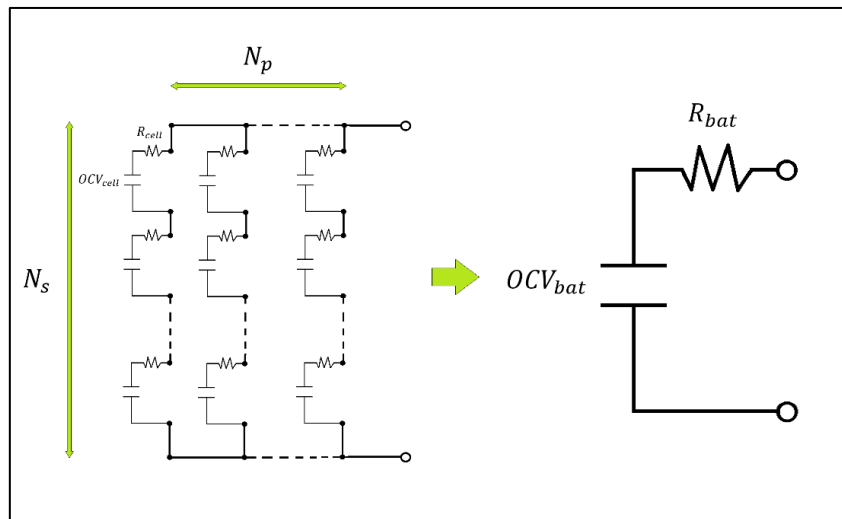


Figure 4.2: Battery equivalent electric circuit model obtained as Thevenin's equivalent circuit.

In particular, thanks to the mentioned theorem, the following relations between cell and battery electric parameters can be introduced:

$$OCV_{bat} = N_s OCV_{cell} \quad (21)$$

$$R_{bat} = \frac{N_s}{N_p} R_{cell} \quad (22)$$

As a consequence, by reasoning on equations (20) and (21) it can be inferred that a configuration of $N_{tot}=1440$ cylindrical cells organized in $N_p=12$ and $N_s=120$ allows to obtain values of battery capacity and voltage that are not so distant from the desired ones. In particular, the results obtained are reported in table 4.1 (computed by equations (20) and (21) using the nominal values of cell parameters [19]).

N_p	12
N_s	120
$C_{cell,nom}$ (Wh)	7.6
$C_{bat,nom}$ (Wh)	10940
$OCV_{cell,nom}$ (V)	3.33
$OCV_{bat,nom}$ (V)	400

Table 4.1: Cell and battery nominal values of capacity and voltage [19].

Now that the battery has been electrically modeled in a proper way, it is possible to start considering its functioning. By applying the power conservation law to the resulting battery (figure 4.3), the following equation is obtained:

$$V_{bat}I_{bat} = OCV_{bat}I_{bat} - I_{bat}^2R_{bat} \quad (23)$$

where V_{bat} (V) is the voltage that is effectively supplied at battery terminals when the pack is handling a current I_{bat} (A). Both V_{bat} and I_{bat} are unknowns, but if V_{bat} can be exclusively positive, I_{bat} is positive (that means it is equally oriented with the related arrow in figure 4.3) during discharging events and negative during charging phases.

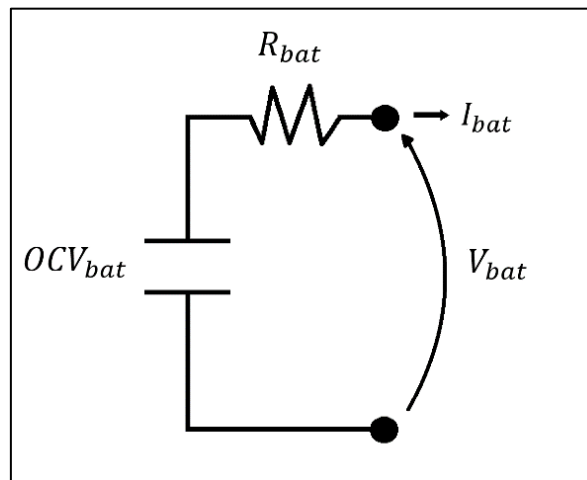


Figure 4.3: Battery equivalent electric circuit model in operation.

Apparently, solving equation (23) appears complex since two unknowns (V_{bat} and I_{bat}) are present. However, it is possible to introduce the battery power $P_{bat} = V_{bat}I_{bat}$, that is known since calculable from the powertrain operating condition:

$$P_{bat} = P_{bat,MGP4} + P_{bat,MGP0} + P_{aux} \quad (24)$$

in which P_{aux} (W) is the power related to the auxiliaries supplied by the high voltage battery. In particular, it can be expressed as:

$$P_{aux} = 100W + P_{fan} + P_{heat} \quad (25)$$

where, besides a constant request supposed of $100 W$, there are the terms P_{fan} (W) and P_{heat} (W) referring respectively to the powers requested by the fan of the cooling system (introduced in the next subchapter), when operating, and the power consumed by the heating pads inside the battery, when they are on. An important aspect concerning P_{bat} is not to confuse it with the internal battery power $P_{int,bat} = OCV_{bat}I_{bat}$.

Back to the solution of equation (23), it turns out to be:

$$I_{bat} = \frac{OCV_{bat} \pm \sqrt{OCV_{bat}^2 - 4P_{bat}R_{bat}}}{2R_{bat}} \quad (26)$$

from whom, since I_{bat} can be null as well, it is inferred that the actual I_{bat} is:

$$I_{bat} = \frac{OCV_{bat} - \sqrt{OCV_{bat}^2 - 4P_{bat}R_{bat}}}{2R_{bat}} \quad (27)$$

Once I_{bat} has been computed, besides V_{bat} it is possible to calculate at any instant both the battery C-rate and the battery SOC, this latter by means of the Current integration method, as it is commonly done in literature [20,22]:

$$C_{rate} = \frac{|I_{bat}|}{C_{Ah,bat}} \quad (28)$$

$$SOC = SOC_0 - \int_0^t \frac{I_{bat}}{C_{Ah,bat}} dt \quad (29)$$

where SOC_0 is the initial battery SOC and $C_{Ah,bat}$ (Ah) is the battery capacity, but now expressed in Ah and related to C_{bat} (Wh) by $C_{bat} = C_{Ah,bat}OCV_{bat}$. It must be specified that, even if the unit of measurement of the C-rate is $1/h$, it is normally indicated as a dimensionless parameter, but, obviously, it is not. Moreover, in equation (28), before integrating over time, $C_{Ah,bat}$ must be expressed according to SI (International System of Units), i.e. in As (equal to 3600Ah).

4.2. Single Temperature Lumped-Parameter Model and BTMS [32,33]

The temperature has a great impact on battery performances. In fact, it intervenes in both SOC and SOH variations. In fact, with respect to the SOC, at low temperatures the internal electric resistance of the battery R_{bat} becomes larger [6,9] and, consequently, the battery discharges faster. Conversely, as far as SOH is concerned, both high [5,9] and low [7,8] temperatures cause problems (as shown in 1.1. *Introduction to Battery Aging: Calendar and Cycle Life*). However, as already mentioned, in literature are not present many cycle life models concerning the battery aging at low temperatures (A123 26650 included), but it is clear that the degradation occurs. Therefore, the temperature is effectively a fundamental aspect to manage and, as a consequence, both battery cooling and heating systems are requested to be installed on HEVs in order to maintain battery temperature within designated range (normally 15°C-35°C). However, simply speaking about battery temperature is not accurate. In fact, the battery is an extended body characterized by a distribution of temperature that is rather complex to model [34]. Nevertheless, as already mentioned in chapter 2.2. *Battery Thermal Management in Quasi-Static Vehicle Models*, the thermal lumped-parameter models employing a single battery temperature T_{bat} (K) are considered a valid compromise between simplicity and precision. As a consequence, with the goal of acquiring the evolution of battery temperature and trying to maintain it within reasonable thresholds, a single temperature lumped-parameter model of the battery, together with the related BTMS, has been formulated by taking inspiration from the works by Han [25] and Jaguemont [6].

As illustrated in the previous subchapter, the battery considered in this paper is constituted by a total of 1440 cylindrical cells of type A123 26650. As reported by the manufacturer [19], each cell is shaped in a cylinder of $\text{\O}26 \times 65 \text{ mm}$, for 76 g of weight.

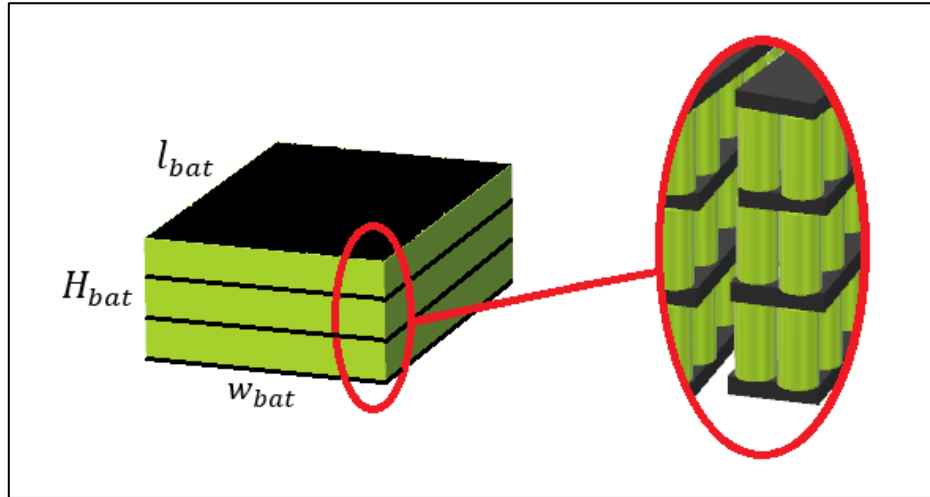


Figure 4.4: Battery cells configuration.

Therefore, from the manipulation of these values, along with some data from the work of Kim et al. (2013) [34], the reasonable values reported in table 4.2 have been obtained. In particular, they refer to the battery mass m_{bat} (kg), to its specific heat c_{bat} (J/kgK) and to its sizes: length l_{bat} (mm), height H_{bat} (mm), width w_{bat} and consequent exchange surface S_{bat} (m^2) with the surrounding air, characterized by a specific heat $c_{p,air}$ (J/kgK).

m_{bat} (kg)	109.44
$l_{bat} \times H_{bat} \times w_{bat}$ (mm)	1050x240x400
S_{bat} (m^2)	1.10
$S_{int,bat}$ (m^2)	2.55
c_{bat} (J/kgK)	1109.2
$c_{p,air}$ (J/kgK)	1005

Table 4.2: Battery and air thermal parameters [19, 34].

It is interesting to point out that, even if the battery is modeled in a thermal lumped way, it is not lumped from a spatial point of view (figure 4.4). In particular, along l_{bat} are aligned 40 cells, along H_{bat} 3 and, finally, along w_{bat} 12 cells (organized in pairs), leaving the space necessary for the heating pads (in black) and for the channels (of 15 mm of width) in which, when the cooling system operates, flows the cooling air from the cabin, constituting an overall exchange surface $S_{int,bat}$ (m^2) (table 4.2).

4.2.1. Air Cooling System

With respect to the air cooling system, the most commonly solution of exploiting the cabin air has been employed in this work. In particular, the paper by Han (2018) [25] has been adopted as main reference for the following considerations. As already mentioned, the air cooling is less effective than liquid cooling, but still widely used since cheaper and simpler to install [24]. Moreover, it is commonly employed in literature when the purpose is the evaluation of the thermal behavior of cylindrical Li-ion cells [23,35]. In addition, the objective of this work is not to find out the best cooling system possible, but to analyze how the actual operation of a realistic cooling system (with several simplifications, as, for example, the neglect of the thermal gradient that characterized air cooled batteries [34]) impacts on the effective employment, during driving missions, of electric power.

Consequently, a scheme of the cooling system implemented is reported in figure 4.5.

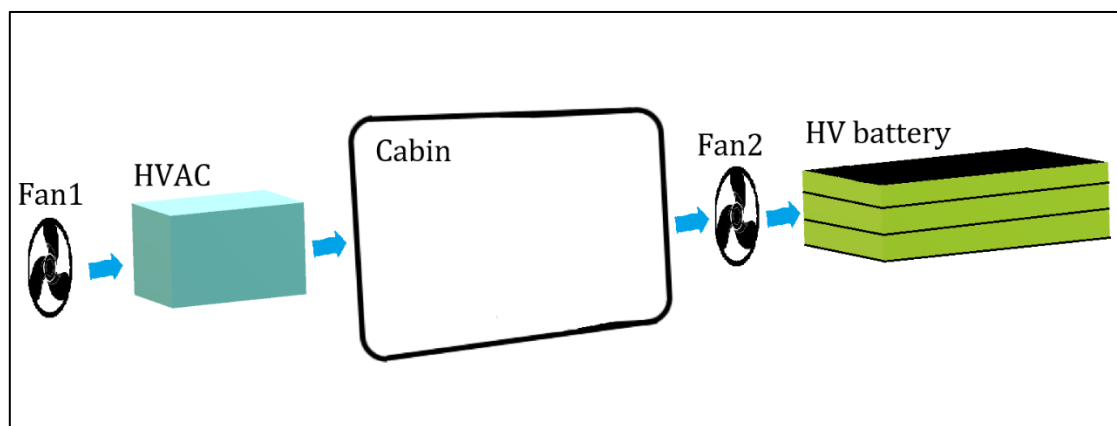


Figure 4.5: Air cooling circuit.

When the cooling system is on (condition evaluated by means of the parameter $CSstate$, that can thus be equal to *on* or *off*), the path the air flow rate follows (indicated by the blue arrows in figure 4.5) starts, pushed by a fan (in the figure

indicated as Fan1), from the HVAC (Heating, Ventilation, and Air Conditioning) system; then it continues in the vehicle cabin and finally, by means of a second fan (Fan2 in figure 4.5), it passes through the battery (in the channels conveniently left among the cells, figure 4.4), in which it occurs a forced convection heat exchange by means of $S_{int,bat}$. However, it is important to specify that, since the air flow rate recirculates, this solution can slightly affect the cabin climate comfort of the passengers [24]. Moreover, if the passengers do not switch on the air conditioning, the air flow tasked to cool the battery will be at ambient temperature, limiting decisively the cooling effect. Obviously, when the cooling system is off ($CSstate = off$), the battery only dissipates heat with the surrounding air (natural convection, passive cooling) by means of S_{bat} . Afterward, it must also be specified that the $CSstate$ value depends on the battery temperature; in fact, the cooling system starts working when the battery temperature reaches T_{CSon} (K) and stops when it goes below T_{CSoff} (K). As it will be shown in chapter 5. *Model Performances and Sensitivity Analysis*, the choice of these two temperatures is not trivial and the definitive ones will be determined by means of a PSO.

Once the main features of the cooling system have been illustrated, it is possible to introduce the corresponding thermal model, together with the related parameters and the simplifications adopted.

As far as the heat generation Q_{bat} (W) inside the battery is concerned, it has been considered related to the Joule's heating only:

$$Q_{bat} = R_{bat} I_{bat}^2 \quad (30)$$

In particular, Q_{bat} can take three different paths: a portion Q_C (W) remains stored in the battery and contributes to increase its temperature; a quantity $Q_{sur,air}$ (W) is dispersed by means of natural convective phenomena with the surrounding air, supposed at a constant temperature T_{cabin} (K), while the remaining part $Q_{int,air}$ (W), that is different from zero only when the cooling system is operating ($CSstate = on$), is the portion of heat transferred to the air flow rate (at T_{cabin} as well) passing through the battery and generated by a fan (Fan2). With respect to T_{cabin} , when the HVAC is not operating, it has been considered equal to the ambient temperature T_a (K);

conversely, when the passengers use the air conditioning, it has been set fixed constantly at 20°C (introducing in this way an important approximation).

Hence, the following equation can be written:

$$Q_{bat} = Q_c + Q_{sur,air} + Q_{int,air} \quad (31)$$

that, by expliciting each term, can be rewritten as:

$$R_{bat} I_{bat}^2 = m_{bat} c_{bat} \frac{dT_{bat}}{dt} + \frac{(T_{bat} - T_{cabin})}{R_{sur,air}} + \frac{(T_{bat} - T_{cabin})}{R_{int,air}} \cdot (CSstate = on) \quad (32)$$

where $R_{sur,air}$ (K/W) and $R_{int,air}$ (K/W) are the overall thermal resistances respectively implicated in the heat transfer from the battery to the surrounding air and to the cooling flow rate (when $CSstate = on$).

In general, similarly to the electric case, different contributions (related among them in series or in parallel) intervene into thermal resistances evaluation. These shares, for the temperature ranges involved here, are mainly of conductive and convective nature. However, the order of magnitude of each thermal resistance considered in this model is defined by a convective contribution, whereas the other contributions are decisively minor. Hence, since this model is far from being a rigorous thermal study and its objective simply is to obtain plausible evolution of T_{bat} from reasonable values of the parameters, it was solely considered the respective more incisive convective contribution. As a consequence, $R_{sur,air}$ and $R_{int,air}$ are thus defined:

$$R_{sur,air} = \frac{1}{h_{sur,air} S_{bat}} \quad (33)$$

$$R_{int,air} = \frac{1}{h_{int,air} S_{int,bat}} \quad (34)$$

where $h_{sur,air}$ (W/m^2K) is the convective coefficient of the air surrounding the battery and $h_{int,air}$ (W/m^2K) is the convective coefficient of the air passing through the battery. Both these values are collected in table 4.3.

$h_{sur,air}$ (W/m^2K)	10
$h_{int,air}$ (W/m^2K)	50

Table 4.3: Air convective coefficients [35].

Therefore, all the parameters of equation (32) are determined. Nevertheless, it is necessary to specify a notable approximation that concerns this equation.

Specifically, this main approximation refers to the way the convective heat exchange between the battery and the air flow rate has been modelled. In fact, if the way the natural convection has been considered is the standard one (both in the expression of $Q_{sur,air}$ and in the choice of $h_{sur,air}$ value), the evaluation of the forced convection contribution is not rigorous. As it is commonly known, the convective coefficient (especially for forced convection) is not an intrinsic property of the considered fluid, but it is also influenced by the geometry of the object immersed in/containing the fluid flow and by the flow rate magnitude (consequently by the velocity of the fluid as well) [35]. As a consequence, its evaluation is rather complex and normally it is obtained by means of correlations (designed for forced convection) available in literature and correlating the adimensional numbers of Reynolds, Prandtl and Nusselt [35]. However, these correlations normally refer to very simple cases and, if applied to more intricate configurations, can lead to important errors. Nevertheless, in literature, it is quite usual to find tables that associate to the most widely used fluid the respective range of variation of the convective coefficient (figure 4.6).

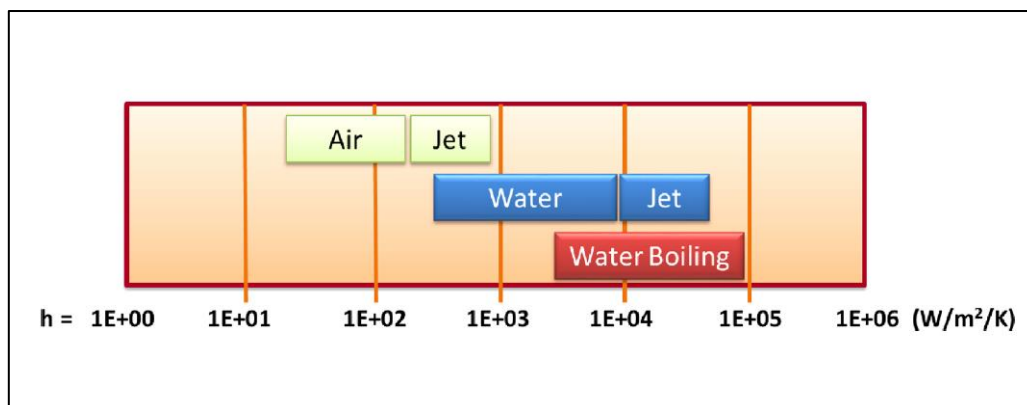


Figure 4.6: Common convective coefficient for air and water. Source: [h].

Therefore, it is quite common to simply pick a value in the range, without taking into account all the aforesaid aspects that effectively influence the actual size of the convective coefficient. Consequently, serious errors can be made, especially when the convection phenomenon regard a specific quantity of flow rate (as for the pipes case and similar). With respect to this work, as already highlighted, the procedure followed has not been precise, for several reasons. In fact, the quantity $Q_{int,air}$, that refers to the thermal exchange between the battery and the air flow rate, is characterized by some notable approximations. To start, the formula employed for $Q_{int,air}$ (used in equation (32)) considers that the air flow remains at a constant temperature equal to T_{cabin} during the heat exchange with the battery. Obviously, this is not realistic, but it is acceptable when the first principle of thermodynamics is applied to the flow rate in question. Therefore, with respect to this work case, the first principle concerning the air flow passing through the battery can be written in the following way:

$$\frac{(T_{bat} - T_{cabin})}{R_{int,air}} = \dot{m}_{int,air} c_{p,air} (T_{out,bat} - T_{cabin}) \quad (35)$$

in which $\dot{m}_{int,air}$ (kg/s) refers to air mass flow rate whereas $T_{out,bat}$ (K) indicates the temperature of the flow rate coming out from the battery (which, because of the previous considerations, can be interpreted as an instantaneous change of the air flow rate temperature once out of the battery). From equation (35), it is evident that, for a specific value of $\dot{m}_{int,air}$, the maximum absorption of heat that is theoretically permitted to the air flow rate occurs when $T_{out,bat} = T_{bat}$. Consequently, by remembering equation (34), this limit condition corresponds to:

$$h_{int,air} S_{int,bat} = \dot{m}_{int,air} c_{p,air} \quad (36)$$

Therefore, by using the values of $S_{int,bat}$ and $c_{p,air}$ reported in table 4.2 and adopting a typical value of \dot{m}_{air} normally managed by a HVAC system, that, according to Han's work [25], is around 0.127 kg/s (i.e. $380 \text{ m}^3/h$ at 20°C), it can be obtained $h_{int,air} = 50 \text{ W/m}^2\text{K}$, exactly as reported in table 4.3 (i.e. the value employed in this work). Therefore, although a convective coefficient of $50 \text{ W/m}^2\text{K}$ could appear as a scant

value for air into motion (according to figure 4.6), it actually represents the maximum theoretic limit condition permitted by the first principle of thermodynamics for the case considered. Consequently, as already mentioned, it does not make sense to speak about forced convective coefficients without specifying both the exchange surface in question (i.e. the geometry) and the magnitude of fluid flow rate. Therefore, back to this work, the heat absorbed by the air flow rate has been set equal to the limit condition (unfeasible in practice) expressed by equation (36). Although not realistic, this approximation can be considered acceptable for the purposes of this paper and, in addition, it still results more precise than assigning a convective coefficient without further information.

With respect to the power requested for the operating of the cooling system, the HVAC system and the relative fan (Fan1 in figure 4.5) could be considered supplied by the ICE; however, this solution is not feasible since it will not allow the HVAC system to operate while travelling in pure electric or at standstill (due to start&stop logic). Consequently, they both are supplied by the battery, but, for reasons explained later in chapter 6., their power employment has not been considered in equation (25) (i.e. they do not weight on the battery). With respect to the power requested by the other fan (Fan2), indicated as P_{fan} and present in equation (25) (i.e. effectively provided by the battery when $CSstate = on$), its value has been set equal to 200 W [36].

4.2.2. Heating Pads System

As already mentioned, low temperatures can affect battery life too. However, if for temperatures superior than 15°C it exists in literature a proven life cycle model concerning A123 26650 cell (Wang's model [9]), this is not true, for the moment, for lower thermal conditions. Consequently, due to the fact that below 15°C the consequences on battery aging cannot be quantified precisely, but it is sure that they brings to a reduction of battery life, in this work the battery has been equipped with a system of heating pads (according to the configuration of figure 4.4), inspired by the solution adopted by Jaguemont [6], that guarantees battery temperature does not go below 15°C when operating. Moreover, when the vehicle is connected to the electric grid (therefore it is recharging), these pads bring and maintain the battery at a temperature of 20°C when $T_a < 15^\circ\text{C}$, by using electric power supply by the grid. Therefore, it is possible to write the following battery thermal equation:

$$Q_{bat} = Q_c + Q_{sur,air} + Q_{heat} \quad (37)$$

where Q_{heat} is the heat power furnished by the heating pads to the battery and is equal to the electric power P_{heat} requested by the heating pads to the battery:

$$R_{bat} I_{bat}^2 = m_{bat} c_{bat} \frac{dT_{bat}}{dt} + \frac{(T_{bat} - T_{cabin})}{R_{sur,air}} + P_{heat} \cdot (HSstate = on) \quad (38)$$

In particular, when the heating pads operates ($HSstate = on$), it results $Q_{heat} = 360 \text{ W}$. Similarly to the cooling system logic, the heating system starts operating when T_{bat} goes below T_{HSon} (K) and remains active until T_{bat} reaches T_{HSoff} (K).

With respect to the T_{cabin} value, now again it can assume two values. In case the HVAC system is not operating, it results $T_{cabin} = T_a$, whereas, if the hot air is blown (obviously for low temperatures the HVAC system does not furnish conditioned air, but heated one), it turns out to be constantly $T_{cabin} = 20^\circ\text{C}$.

4.3. Throughput-Based Battery Capacity Fade Model

As declared in *1. Preface*, this work wants to focus mainly on battery cycle life, that is related to the aging that occurs during battery usage and is influenced by the operating conditions (DOD swing, C-rate and battery temperature). In general, the cycle life can be evaluated by using three different types of models [20]: electrochemical, event-based or energy-throughput based models. Similarly to the studies mentioned in chapter 2. *State of the Art*, in this paper it has been employed a throughput-based battery capacity fade model [20] (third typology), which is based on the concept of battery charge throughput (Ah-throughput). However, in literature, divergent interpretations of this quantity are present. In fact, some authors associate the Ah-throughput to the overall quantity of charge that a battery is able to deliver before reaching its EOL [20]. Therefore, they interpret it as the value obtained by summing all the quantity of charge that can be related to each discharging phase performed by the battery throughout its life. Others, instead, believe that charging phases must be consider as well [21]. Therefore, according to this latter point of view, plug-in charging contributions and regenerative braking events must be taken into account too. Although both schools of thought are reliable, the second one results

more precautionary since believes that recharging impacts battery life as well. Therefore, in this paper, it has been adopted the following definition of battery charge throughput, indicated by $Q_{Ah,EOL}$ (Ah):

$$Q_{Ah,EOL} = \int_0^{t_{EOL}} |I_{bat}| dt \quad (39)$$

where t_{EOL} (s) is the instant of time in which occurs the EOL and its duration depends on the already mentioned conditions of utilization of the battery, that normally vary during battery operation. Obviously, for being expressed in Ah, the result of the integral must be divided by 3600. Conventionally, the EOL occurs when the percentage value of battery nominal capacity decrement, indicated by $C_{fading,Ah,\%}$, equals 20% (i.e. $C_{fading,Ah,\%} = 20$). When the battery operates under constant conditions, $Q_{Ah,EOL}$ and $C_{fading,Ah,\%}$ can be related among them by adapting to the entire battery the formula proposed by Wang [9] for a single A123 26650 cell (inspired by the Arrhenius' gas equation [5]):

$$C_{fading,Ah,\%} = B \cdot \exp\left(-\frac{A_f}{T_{bat}}\right) \left(\frac{Q_{Ah,EOL,const}}{N_p \cdot 1 Ah}\right)^z \quad (40)$$

in which it is interesting to observe that the battery charge throughput has been indicated as $Q_{Ah,EOL,const}$ for specifying it refers to the value obtained under constant conditions. In equation (40) are then present the terms B , A_f (K) and z that indicate respectively the pre-exponential factor, the aging factor and the power-law factor [22]. Since these parameters refer to a single cell, in order to move to the whole battery it is necessary to divide $Q_{Ah,EOL,const}$ by the number of parallel branches N_p , as done in equation (40). The values of B , A_f and z [9] are reported in table 4.4. In particular, B (linearly interpolated) and A_f depend on the battery C-rate.

Hence, $Q_{Ah,EOL,const}$ can be computed as:

$$Q_{Ah,EOL,const} = N_p \left(\frac{C_{fading,Ah,\%}}{B} \exp\left(\frac{A_f}{T_{bat}}\right) \right)^{\frac{1}{z}} \cdot 1 Ah \quad (41)$$

Therefore, $Q_{Ah,EOL,const}$ depends on the constant values of C-rate and temperature the battery is subjected to, but not on the DOD swing extent. In fact, as shown by Wang [9], the DOD does not have any noteworthy effect on $Q_{Ah,EOL,const}$ of A123 cells.

By computing $Q_{Ah,EOL,const}$ for different values of C-rate at a constant temperature of 25°C (figure 4.7), it can be observed a strange behavior of this quantity, that, intuitively, should decrease along with C-rate growth. As it was explained by Ebbesen [20], the weird curve trend at low C-rate is due to the fact that, during the experimentation conducted for obtaining equation (40) [9], the calendar life effects were not inhibit and, for this segment of C-rate values, they had considerable influenced the results obtained.

B	$C_{rate} = 0.5$	31630
	$C_{rate} = 2$	21681
	$C_{rate} = 6$	12934
	$C_{rate} = 10$	15512
$A_f (K)$		$3814.68-44.56 \left(\frac{C_{rate}}{1/h}\right)$
z		0.55

Table 4.4: Battery aging parameters for A123 26650 cell [9].

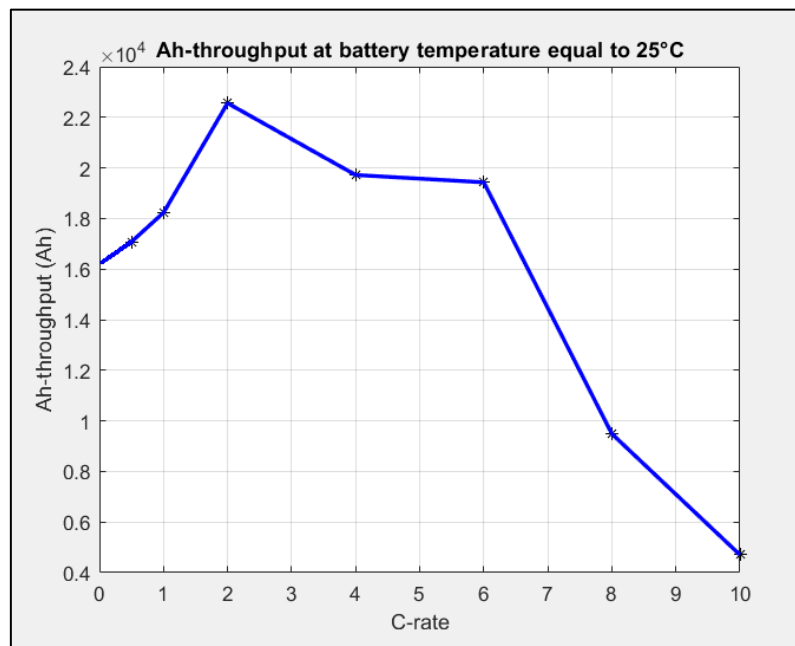


Figure 4.7: Ah-throughput evolution at 25°C according to C-rate variation.

Moreover, it is probably more interesting to compute $Q_{Ah,EOL,const}$ for different values of T_{bat} with a constant C-rate of 2 (figure 4.8). In particular, it can be observed that the evident notable variation of $Q_{Ah,EOL,const}$ (in fact, at 35°C the Ah-throughput is less than a third of the value at 20°C) occurs while remaining inside the ideal thermal range of Li-ion batteries, i.e. 15-35°C [7].

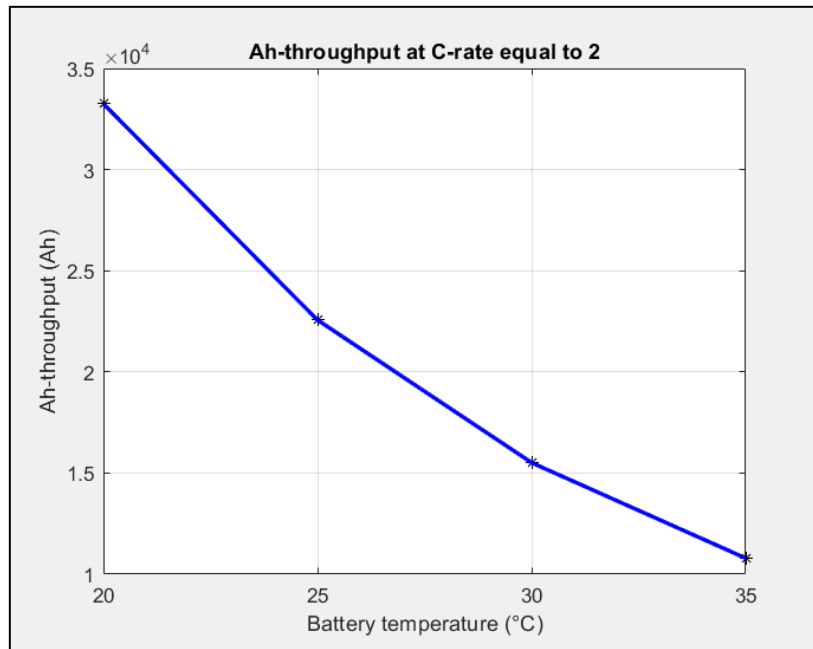


Figure 4.8: Ah-throughput evolution at C-rate=2 according to temperature variation.

After computing $Q_{Ah,EOL,const}$, if it is known the overall quantity of charge $Q_{Ah,const}$ (Ah) that has been supplied by a battery under fixed values of C-rate and temperature, it is possible to evaluate the current battery “state of aging” by comparing $Q_{Ah,const}$ with $Q_{Ah,EOL,const}$. However, as already highlighted in 2.1. *Capacity Fade Models*, the batteries employed in HEVs will unlikely operate at constant value of C-rate and T_{bat} . On the contrary, these parameters change continuously. Therefore, in order to evaluate the contribution of each pair of C-rate and T_{bat} towards the achievement of $Q_{Ah,EOL}$, a concept similar to that of damage present in the Palmgren-Miner’s rule, that is used in the evaluation of structural failure for mechanic fatigue, can be adopted. In particular, the SOH concept proposed by Ebbesen [20], that reaches the null value at the EOL, follows this idea. However, the concept of number of cycles this author uses it is abandoned in this paper, since it results of little significance for batteries subjected to variable C-rate, temperature and

DOD swing. Moreover, Ebbesen [20] interprets the Ah-throughput differently from the way adopted here. For these reasons, the modified equation proposed here for the evaluation of SOH, that results symmetric to that of SOC, is the following:

$$SOH = SOH_0 - \int_0^t \frac{|I_{bat}|}{Q_{Ah,EOL,const}} dt \quad (42)$$

where SOH_0 is the initial state of health of the battery and, when the battery is brand new, it is equal to 1. Obviously, $Q_{Ah,EOL,const}$ varies continuously with the C-rate and T_{bat} and, when integrating, it must be expressed in As (instead of Ah). With respect to the mentioned influence of calendar life effects on $Q_{Ah,EOL,const}$ at low C-rate (figure 4.7), it could be reasonable thought to eliminate it by not considering the aging contribution of little C-rates. However, since the currents at stake in these circumstances are small, their actual participation in the aging process still remains negligible. Instead, different considerations will be done while computing, in subchapter 5.2., the participation of plug-in recharge to battery aging.

5. Model Performances and Sensitivity Analysis

Once the *Simulink* model of the vehicle (which, evidently, includes also the battery model described in the previous chapter) is realized, it is possible to move to the simulation phase. In order to allow the reader to autonomously judge the results obtained from the following simulations, it is necessary to specify precisely the way they were conducted.

5.1. Driving Missions

With respect to the driving missions that have been simulated, since the objective was to approach as much as possible to the actual utilization of the vehicle, besides some standard driving cycles (*WLTP*, *RTS 95*, *FTP 75* and *HWFET*), which are commonly used for evaluating the performances of real vehicles and making comparisons among them, four real-world driving missions have been employed as well. This fact really increases the veracity of the simulations since, as already highlighted in 3.2. *Vehicle Free Body Diagram*, the real-world driving missions, besides the data of speed and acceleration at each instant, are also equipped with the road grade information, normally not present in standard driving cycles.

Therefore, a total of eight driving missions has been considered. With respect to the four real-world driving missions, they have been recorded by the supervisors of this thesis and include an extra-urban uphill mission (from now on indicated as RWD01), a long highway trip (RWD03), a down mountain tract (RWD04) and an extra-urban downhill mission (RWD06). All the main information about these eight driving missions is collected in table 5.1 and the corresponding evolutions of speed and altitude values over time are depicted in figures 5.1-5.8.

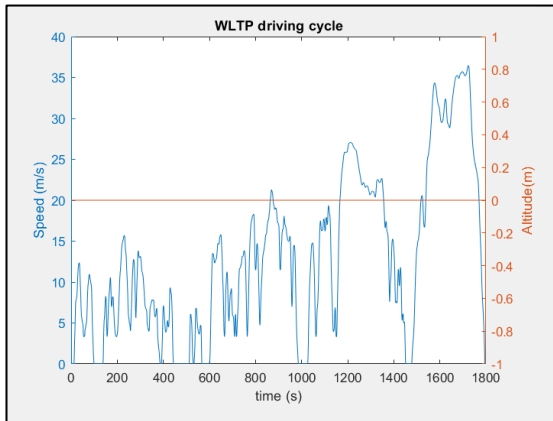


Figure 5.1: WLTP driving cycle.

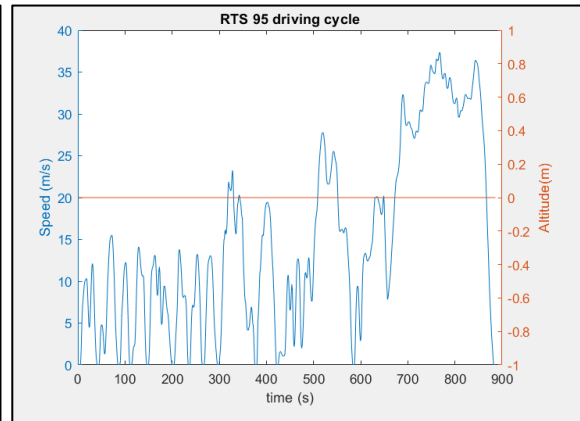


Figure 5.2: RTS 95 driving cycle.

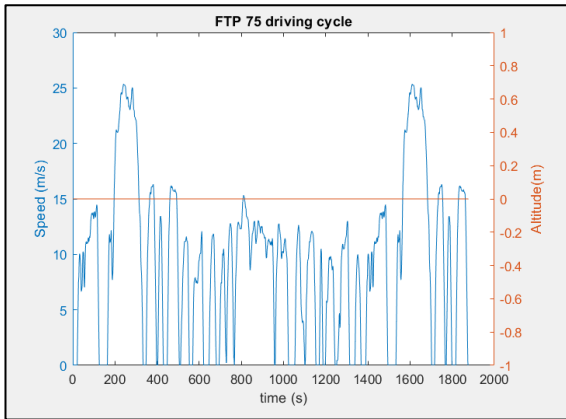


Figure 5.3: FTP 75 driving cycle.

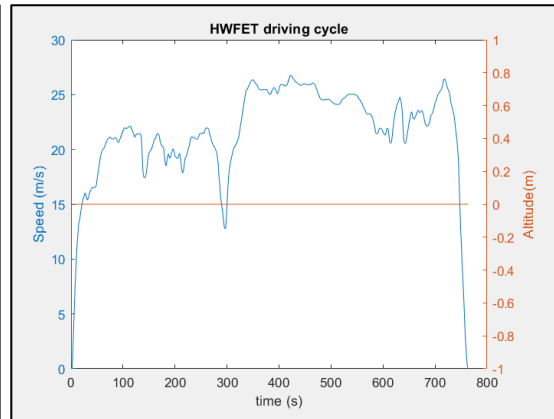


Figure 5.4: HWFET driving cycle.

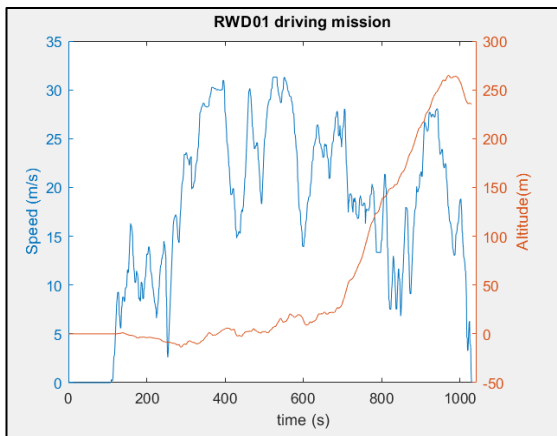


Figure 5.5: RWD01 driving mission.

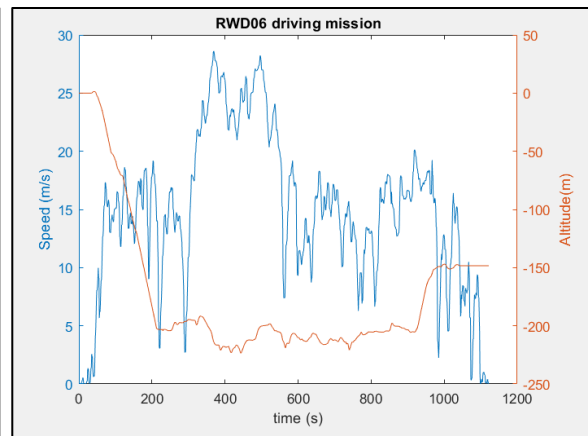


Figure 5.6: RWD06 driving mission.

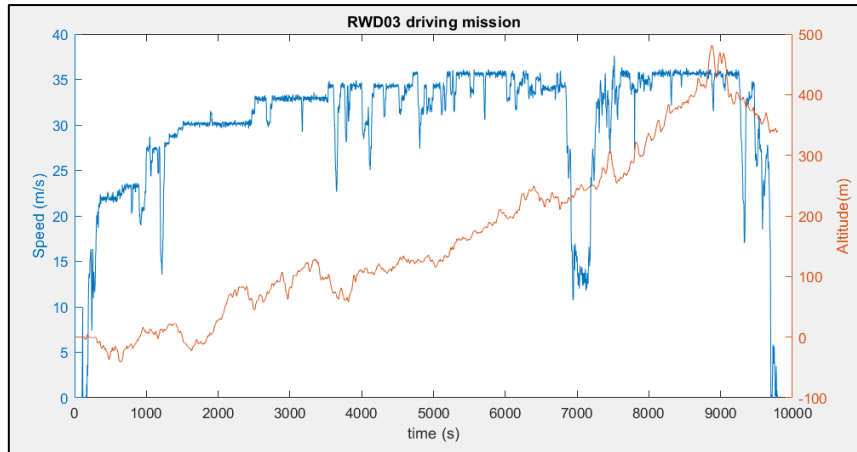


Figure 5.7: RWD03 driving mission.

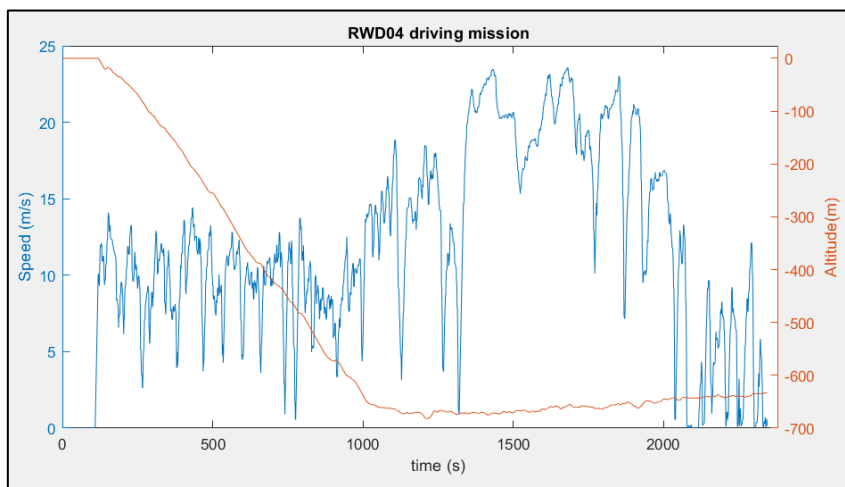


Figure 5.8: RWD04 driving mission.

Driving mission	Distance (km)	Difference of altitude end-beginning (m)	Maximum speed (km/h)	Total time (s)
<i>WLTP</i>	23.27	0	131.30	1800
<i>RTS 95</i>	12.93	0	134.45	886
<i>FTP 75</i>	17.77	0	91.25	1877
<i>HWFET</i>	16.49	0	96.30	765
<i>RWD01</i>	17.78	235	112.68	1031
<i>RWD03</i>	296	341	135.40	9792
<i>RWD04</i>	27.39	-632	84.88	2345
<i>RWD06</i>	16.69	-148	102.97	1123

Table 5.1: Driving missions main characteristics: distance, difference of altitude end-beginning, maximum speed and total time.

Moreover, interesting considerations can be made about how the driver model (i.e. the PID controller) performs when the road presents a varying slope. Indeed, as illustrated in subchapter 3.3. *Driver Model*, the PID controller calibrates its indications from a single input concerning the difference between v_{des} and v (figure 3.10). Therefore, the PID has no feeling about the variation of road slope, whereas the real driver yes (he/she constantly adjusts the pedals position according to the road grade is going to be travelled). Consequently, if from a speed point of view (gap between v and v_{des} curves) the PID continues to function properly, some issues arise while comparing the actual acceleration to the desired one. In fact, as figures 5.9 and 5.10 show, when the road is flat (e.g. *FTP 75*), these two accelerations are very similar, whereas when the slope varies (e.g. *RWD01*), they are slightly different.

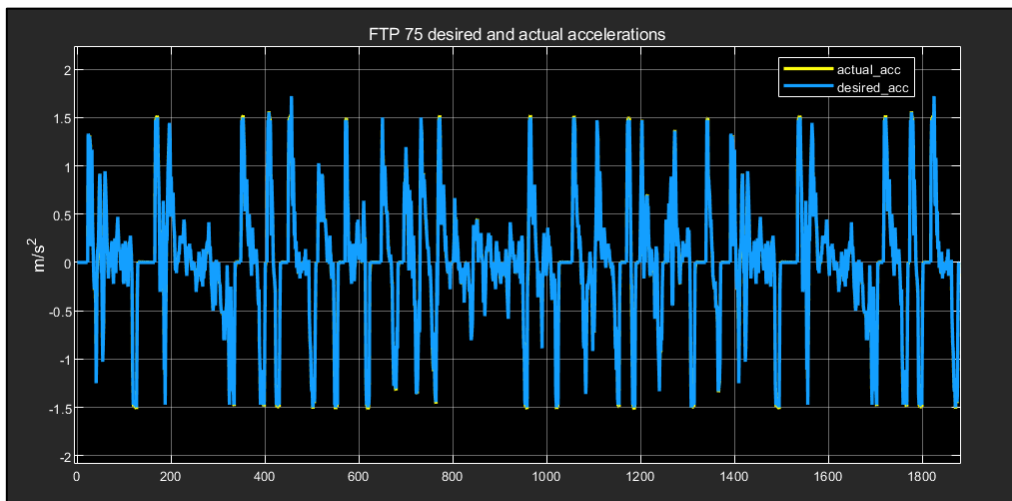


Figure 5.9: *FTP 75 (flat route) desired and actual accelerations.*

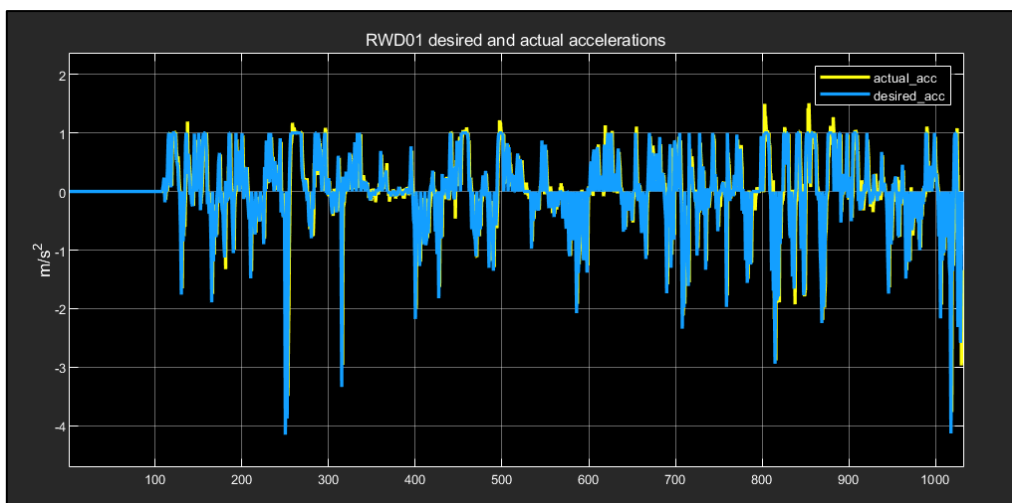


Figure 5.10: *RWD01 (sloping route) desired and actual accelerations.*

In particular, these discrepancies occur in all those occasions in which (unexpectedly for the PID controller), for example, an uphill stretch (that corresponds, in figure 5.10, to a larger actual acceleration) or a downhill section (smaller actual acceleration) start. As a consequence, in order to correct this question, it has been tried to ponder the input of the controller (depending on its sign) with a weight that considers the variation of road slope. Although the method implemented allowed to have the two accelerations closer (but not as much as the cases with flat route, figure 5.9), the difference between the results of the simulations conducted with and without this correction was not significative. Therefore, for simplicity, it was decided to maintain the basic controller.

5.2. Model Reliability by means of Consumptions Comparison and Battery

Lifetime Calculation

In order to evaluate the reliability of the model, it was thought to compare the values of consumptions obtained from the simulations, both in terms of fuel (in $l/100km$) and electric energy provided by the battery (in $kWh/100km$), with those declared by *FCA* [11], but also taking into account those values unofficially measured during *Renegade 4xe* real use [37].

In particular, since the official consumptions values have been evaluated on the *WLTP*, it was chosen to use this driving cycle as well. However, due to the fact that the length of the journey really influences the average values (per 100 km) of consumptions, besides one simple *WLTP* (figure 5.1), it was also considered a driving mission composed by 4 cycles of this type disposed in series (from now on indicated as *WLTP4*).

With respect to the simulation conditions, each possible driver selection of driving mode (Hybrid, E-save and Electric) has been simulated starting from four different values of SOC_0 : 0.95 (i.e. battery completely charged), 0.70, 0.40 and 0.21 (i.e. battery almost completely discharged). From a thermal point of view, instead, it was considered a constant ambient temperature $T_a=25^\circ C$ (halfway between $15^\circ C$ and $35^\circ C$), whereas the battery temperature T_{bat} has been left free to increase without the intervention of the cooling system ($CSstate = off$); therefore, the battery dissipates heat only with the surrounding air in a natural convective way (passive cooling).

Moreover, it was considered one only passenger; therefore, in equation (3), it was used $n_{pass}=1$.

In tables 5.2 and 5.3, the consumptions values obtained for both the *WLTP* and the *WLTP4* are collected. Actually, these tables also report the final values of SOC resulting at the end of each simulation, indicated as SOC_{end} . In particular, it is interesting to observe that, in some cases, SOC_{end} results larger than the initial SOC (SOC_0) and, consequently, the respective electric energy consumptions are negative since the battery is not discharged, but charged. Specifically, this can happen in several cases: when the E-save mode is selected, when the EMS (high level RB controller), of necessity (i.e. low values of SOC), moves autonomously to the E-save mode for considerable tracts or, finally, to a lesser extent, thanks to the regenerative braking. Obviously, since in the E-save mode the ICE is normally used for both the traction and the recharge of the battery, the related simulations are particularly fuel consuming (orange cells in tables 5.2 and 5.3) if compared to those effectuated in Electric mode (green cells). However, as affirmed by *FCA* [11], this feature can turn out to be really useful when, for example, it is not possible to charge the battery and it is known that at a certain point of the trip it is necessary to proceed in pure electric for entering a ZTL (zona a traffico limitato) [38]. Therefore, simulating the E-save mode for high values of SOC (i.e. 0.95 and 0.70) is not very realistic because it is very unlikely that the driver selects this mode when the battery is practically completely charged. In fact, since HEVs are known to be more expensive than the corresponding traditional vehicles, it is very likely that who buys a plug-in hybrid vehicle will try to exploit as much as possible the electric driving, in such a way as to minimize fuel consumption. Another interesting aspect about these simulations concerns the fuel consumed for effectuating, starting from high values of SOC_0 (i.e. 0.95 and 0.70), the *WLTP* in Electric Mode. In fact, as reported in table 5.1, the *WLTP* driving cycle stretches around 23 km; therefore, since the HV battery (as specified in subchapter 1.4. *Jeep® Renegade 4xe*) is theoretically able to permit up to 50 km in pure electric [11], it seems odd to see that the employment of fuel is requested in the two cases in question ($1.53 \text{ l}/_{100km}$, table 5.2). However, as specified in subchapter 3.1., the *MGP4* is characterized by a maximum power of 60 hp, which can often be insufficient for the requested traction conditions. Consequently, as illustrated in 3.4. *Default Rule-Based EMS*, the high level RB controller can perform momentary shifts to Hybrid mode in

case of need and, effectively, this is what happens when travelling the *WLTP* with the Electric mode selected and the battery initially almost completely charged. In particular, figure 5.11 shows the moments in which the ICE intervenes while travelling the *WLTP* in Electric mode, with an initial SOC of 0.95 or 0.70.

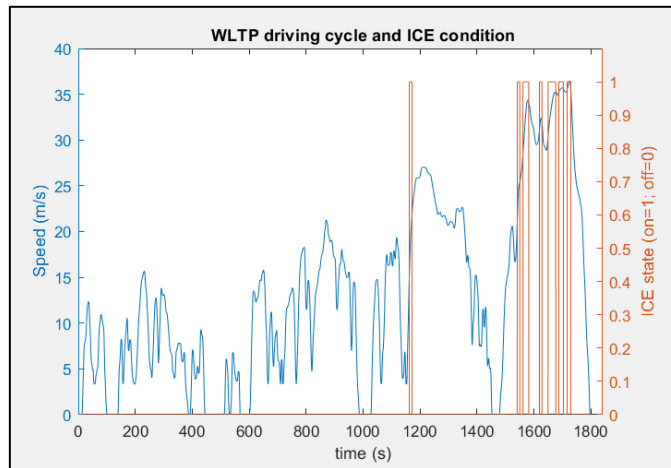


Figure 5.11: Intervention of the ICE while travelling the *WLTP* in Electric mode and starting from a SOC value of 0.95 or 0.70, according to the conditions of table 5.2.

<i>WLTP</i>		<i>SOC</i>₀			
		<u>0.95</u>	<u>0.70</u>	<u>0.40</u>	<u>0.21</u>
<u>Hybrid mode</u>	<i>SOC</i>_{end}	0.67	0.61	0.44	0.33
	<i>l</i>/100km	1.53	4.13	6.60	7.73
	<i>kWh</i>/100km	13.27	3.90	-1.98	-5.37
<u>E-save mode</u>	<i>SOC</i>_{end}	0.94	0.83	0.64	0.45
	<i>l</i>/100km	6.60	7.91	9.78	9.78
	<i>kWh</i>/100km	0.24	-5.87	-11.22	-11.22
<u>Electric mode</u>	<i>SOC</i>_{end}	0.67	0.42	0.32	0.33
	<i>l</i>/100km	1.53	1.53	4.13	7.73
	<i>kWh</i>/100km	13.27	13.19	3.88	-5.37

Table 5.2: Consumptions and final values of SOC related to the simulation of the *WLTP* at $T_a=25^\circ\text{C}$, with the cooling system off, for one only passenger and by using different driving modes and distinct initial values of SOC.

WLTP4		SOC₀			
		<u>0.95</u>	<u>0.70</u>	<u>0.40</u>	<u>0.21</u>
<u>Hybrid mode</u>	SOC_{end}	0.70	0.74	0.57	0.46
	l/100km	4.88	5.99	6.60	6.89
	kWh/100km	2.83	-0.52	-1.98	-2.83
<u>E-save mode</u>	SOC_{end}	0.95	0.95	0.90	0.87
	l/100km	6.60	6.93	7.91	8.53
	kWh/100km	0	-2.87	-5.80	-7.61
<u>Electric mode</u>	SOC_{end}	0.37	0.40	0.45	0.46
	l/100km	3.56	4.63	5.99	6.89
	kWh/100km	6.80	3.52	-0.52	-2.83

Table 5.3: Consumptions and final values of SOC related to the simulation of the WLTP4 (four WLTP disposed in series) at $T_a=25^\circ\text{C}$, with the cooling system off, for one only passenger and by using different driving modes and distinct initial values of SOC.

Anyway, as a whole, by considering the average consumptions obtained with the model realized (for the simulations in Electric and Hybrid modes, tables 5.2 and 5.3), the respective values are in accordance with the sources considered [11,37].

Therefore, since the vehicle model appears valiant (from the consumptions point of view), further considerations can be made. In particular, it is possible to start considering the battery aging. Consequently, employing equation (42) and assuming that the initial battery state of health SOH_0 is equal to 1 for each case previously considered (tables 5.2 and 5.3), it is possible to obtain the related final values of SOH, indicated as SOH_{end} (table 5.4). In particular, it can be observed that, for both the WLTP and the WLTP4, the lowest values of SOH_{end} (yellow cells in table 5.4) occur when the Electric mode is selected. In fact, evidently, this driving mode is the one that exploits the most the battery. However, if for the WLTP4 this happens at $SOC_0=0.95$, with respect to the WLTP, instead, the SOH_{end} referring to $SOC_0=0.70$ is slightly lower (i.e. more critical) than that related to $SOC_0=0.95$.

SOH_{end}		SOC_0			
		<u>0.95</u>	<u>0.70</u>	<u>0.40</u>	<u>0.21</u>
WLTP	<u>Hybrid mode</u>	0.9999479	0.9999732	0.9999932	0.9999835
	<u>E-save mode</u>	0.9999990	0.9999826	0.9999674	0.9999671
	<u>Electric mode</u>	0.9999479	0.9999471	0.9999728	0.9999835
WLTP4	<u>Hybrid mode</u>	0.9999096	0.9999521	0.9999724	0.9999626
	<u>E-save mode</u>	0.9999940	0.9999629	0.9999294	0.9999080
	<u>Electric mode</u>	0.9998536	0.9998983	0.9999514	0.9999626

Table 5.4: Final values of SOH related to the simulations of WLTP and WLTP4 considered in tables 5.2 and 5.3.

Specifically, this latter aspect occurs because, as already shown in figure 5.11, both the initial values of SOC_0 0.95 and 0.70 result in the same alternation between electric and hybrid traction while travelling the WLTP. This specific alternation, instead, does not occur when $SOC_0 = 0.40$ (figure 5.12), since the SOC rapidly reaches the value of 0.30, which marks the passage imposed by the EMS from charge depleting to charge sustaining strategy (i.e. from the Electric mode to the Hybrid one).

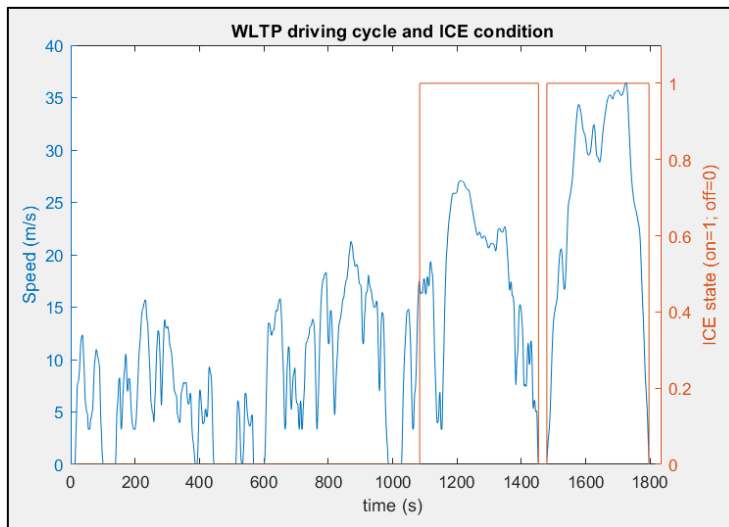


Figure 5.12: Intervention of the ICE while travelling the WLTP in Electric mode and starting from a SOC value of 0.40, according to the conditions of tables 5.2 and 5.3.

Back to SOC_0 equal to 0.95 or 0.70, the latter case turns out to be more critical because the battery works at a lower SOC range (figure 5.13) and, therefore, as specified in 4.4. *Equivalent Electric Circuit Model*, the OCV_{bat} and the R_{bat} result respectively smaller and larger than those for $SOC_0=0.95$. Consequently, the I_{bat} and the C-rate turn out to be larger and this fact explains the lower value of SOH_{end} . However, the difference with the SOH_{end} for $SOC_0=0.95$ is not so substantial and, moreover, in case of longer trips (as the results concerning the simulations of WLTP4 testify in table 5.4), it is intuitive that the aging occurring with $SOC_0=0.95$ is certainly higher than that with $SOC_0=0.70$ (since, evidently, the battery is extensively used for more time, since the 0.30 threshold is reached later). Therefore it can be said that the most critical conditions of use of the battery occur when $SOC_0=0.95$ and the Electric mode is selected. In addition, these are also the most probable conditions since, as already mentioned, if a customer spends more money for an electrified powertrain, he/she will surely try to exploit the pure electric drive as much as possible.

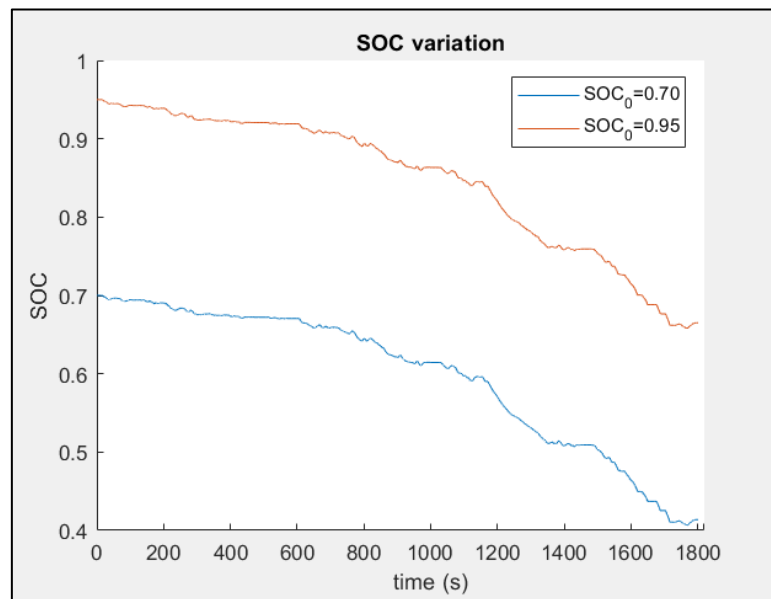


Figure 5.13: SOC evolution while travelling the WLTP in Electric mode and starting from a SOC value of 0.95 or 0.70, according to the conditions of tables 5.2 and 5.3.

Another aspect that can be presumed from table 5.4 is that the WLTP4 seems to be more battery life consuming (since implies lower values of SOH_{end}) than the WLTP. This latter aspect is certainly true when reasoning on the single mission, but can lead to wrong conclusions if shifted to a recurring employment. In fact, focusing on the most critical conditions (that have been associated to the Electric mode and

$SOC_0=0.95$ for both *WLTP* and *WLTP4*), it is possible to introduce an equivalent total number of km provided by the battery during its life, that is the quantity normally employed for estimating battery lifetime (in terms of cycle life, whereas calendar life is normally expressed in years) in automotive applications.

Hence, to compute this quantity, indicated by $L_{bat,km}$ (*km*) and normally simply referred as battery lifetime, the following assumptions are made:

1. at the end of the driving mission the battery is charged back to SOC_0 (in this case 0.95) from the grid;
2. the driving mission in question (for the moment, *WLTP* or *WLTP4*), included the final recharge, is supposed to be repeated identically until the EOL is reached.

Afterward, it is possible to define the following equation:

$$L_{bat,km} = \frac{1}{1 - SOH_{end} + \Delta SOH_{recharge}} \cdot s_{km,tot} \quad (43)$$

where SOH_{end} is computed by using equation (42) and refers to the single driving mission, $s_{km,tot}$ (*km*) is the total space travelled throughout the mission in question and $\Delta SOH_{recharge}$ is the variation of battery SOH due to the plug-in recharge from the SOC_{end} back to SOC_0 , that is supposed effectuated at a constant battery temperature $T_{recharge}$ (equal to T_a if $T_a \geq 15^\circ C$ and to $20^\circ C$ if not) and with a C-rate feasible with the *easyWallbox* [11], indicated as $C_{rate_{easywall}}$. Actually, in this work, as value of $C_{rate_{easywall}}$, it has been used the (unlikely) quantity 2, since, as shown in figure 4.7, it corresponds to the higher value of Ah-throughput (i.e. slower aging). In fact, more realistic C-rates (around 0.3) would imply Ah-throughput values amply affected by calendar aging. Consequently, $\Delta SOH_{recharge}$ can be expressed as:

$$\Delta SOH_{recharge} = \int_0^{t_{recharge}} \frac{|I_{recharge}|}{Q_{Ah,EOL,recharge}} dt \quad (44)$$

in which $I_{recharge}$ (*A*) is the constant current of recharge, that is related to $C_{rate_{easywall}}$ by equation (28), $Q_{Ah,EOL,recharge}$ (*Ah*) is the battery Ah-throughput

related to recharge conditions $T_{recharge}$ and $C_{rate}_{easywall}$ and computed by means of equation (41) (obviously, $Q_{Ah,EOL,recharge}$ must be expressed in As before integrating equation (44), as specified for equation (42)), whereas $t_{recharge}$ (s), that is the recharge duration, is calculated as:

$$t_{recharge} = \frac{SOC_0 - SOC_{end}}{C_{rate}_{easywall}} \quad (45)$$

in which $C_{rate}_{easywall}$ must be expressed in $1/s$ for obtaining $t_{recharge}$ in seconds. Consequently, as reported in table 5.5, it is possible to compute $L_{bat,km}$ values for both *WLTP* and *WLTP4* (simulated according to all the specifications made in the previous paragraphs). In this way, it is evident that the battery ages more rapidly (i.e. it is able to travel less *km* overall) if the vehicle travels repeatedly the *WLTP*. In fact, in this case, during the whole driving mission, the traction power is mainly provided by the battery (figure 5.11), whereas not in the *WLTP4* (figure 5.14); therefore the consequent rate of use of the battery per *km* is larger for the *WLTP* and, consequently, less *km* are feasible overall.

$L_{bat,km}$ (km)	<i>WLTP</i>	318000
	<i>WLTP4</i>	518000

Table 5.5: Battery lifetime values referring to *WLTP* and *WLTP4* when simulated in Electric mode, with $SOC_0=0.95$, at $T_a=25^\circ C$ and with the cooling system off.

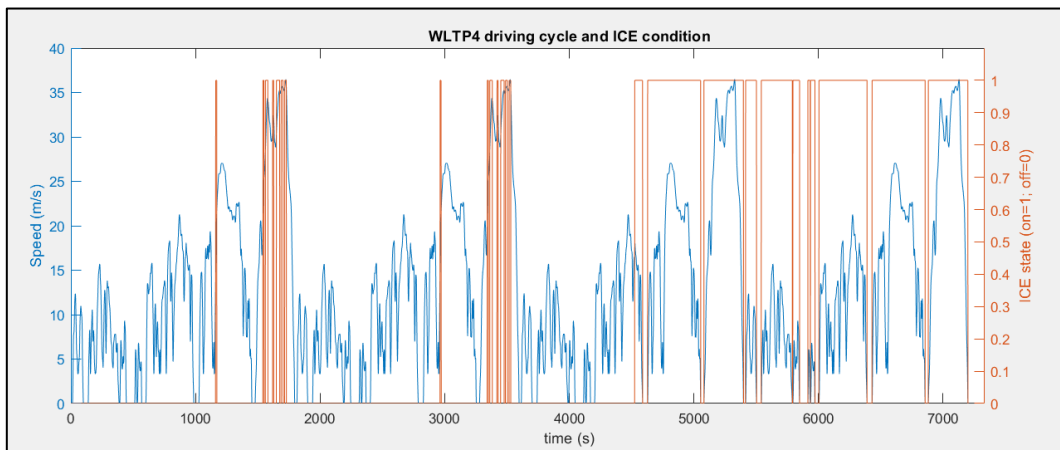


Figure 5.14: : Intervention of the ICE while travelling the *WLTP4* in Electric mode, with $SOC_0=0.95$, at $T_a=25^\circ C$ and with the cooling system off.

However, in order to interpret the values reported in table 5.5, it is necessary to specify what is a reasonable and sufficient amount of km a battery must be able to supply during its life. Consequently, wanting to set a minimum threshold for $L_{bat,km}$, a value around 200000-300000 km can be set, as it is normally done in literature [22]. Therefore, both the values reported in table 5.5 satisfy this requisite; nevertheless, they are not sufficient for asserting that the duration of the battery is not compromised. In fact, even if they refer to the most critic conditions of battery employment (i.e. Electric mode and $SOC_0=0.95$), at the same time they concern very specific cases: the simulation of one only type of driving mission, the *WLTP* (in fact the *WLTP4* is simply made of four *WLTP* in series), and the consideration of one only ambient temperature, 25°C. Consequently, in order to make more significative statements about battery durability, it is necessary to simulate different driving missions (specifically, those indicated in 5.1. *Driving Missions* have been used) for different reasonable values of external temperature.

5.3. Sensitivity Analysis Considerations

As highlighted in the previous subchapter, in order to generalize the results of the simulations, it is necessary to expand the range of different conditions considered. First of all, the eight aforementioned driving missions can be employed. In this way, in fact, it is possible to take into account different potential uses of the vehicle (and therefore of the battery), from short urban employment to long highway trip. Secondly, since the battery temperature, as already introduced, is widely influenced by the ambient one, different reasonable values of T_a have been considered, namely -5°C, 0°C, 5°C, 10°C, 15°C, 20°C, 25°C, 30°C and 35°C [39].

Afterward, since the quantity of simulation parameters is already notable, the following assumptions have been made:

- due to the fact that this work wants to focus on cycle life and knowing that this quantity can be related to the battery rate of use, all the simulations have been conducted with the Electric mode selected and starting from $SOC_0=0.95$ (most critical condition, as highlighted before);
- since the first assumption implies that the battery is initially completely charged, it was considered that the vehicle was connected to the grid before

starting the driving mission; consequently, due to what reported in 4.2.2. *Heating Pads System*, the battery results at an initial temperature equal to 20°C if $T_a < 15^\circ\text{C}$. In all other cases, instead, the battery starting temperature is equal to the ambient one;

- with respect to the number of passengers, that influences the total mass of the vehicle (according to equation (3)), only the two extreme cases have been considered, namely driver alone ($n_{pass} = 1$) and five passengers ($n_{pass} = 5$). Although the number of passengers could appear as an aspect of minor importance, actually it entails interesting considerations since it also intervenes in the computation of the grading resistance (that is present in the real-world driving missions).

Obviously, these assumptions exclude several cases, including some interesting scenarios. For example, it could be intriguing to analyze the situation in which the vehicle is parked without being connected to the grid, with an extremely low ambient temperature and the battery completely out of power, as partly analyzed by Jagemont [6]. However, rather than cycle aging, this latter research would regard calendar aging; therefore, it will be necessary to introduce calendar life models, which are not considered in this work.

Back to the current analysis, before illustrating the results obtained from the simulation of all the eight driving missions, at the given temperatures and according to the aforementioned assumptions, it is necessary to specify how the operation of the BTMS was set and what features have been basically analyzed.

With respect to the cooling and the heating systems, whose functioning depends on the election of the temperatures T_{CSon} , T_{CSoff} , T_{HSon} and T_{HSoff} (subchapters 4.2.1. and 4.2.2.), both these systems have been considered constantly turned off ($CSstate = off$ and $HSstate = off$). In effect, this choice was taken because, when in operation, these systems consume part of the electric energy stored in the battery, that, consequently, cannot be employed for the vehicle traction; therefore, before setting the operation of the BTMS, it is better to evaluate in which cases (among those simulated) the intervention of this system is effectively necessary (i.e. the corresponding employment of electric energy is justified).

Instead, with respect to the traits examined by means of this wide operation of simulations, for each possible combination (of driving missions, temperatures, etc.) it is evaluated if the corresponding battery lifetime $L_{bat,km}$ results larger or not than 200000 km and if the commonly used thermal limits of 15°C and 35°C are overtaken while simulating; therefore, it is checked if the minimum and maximum temperatures reached by the battery during the simulation of a driving mission, respectively indicated as $T_{min} (K)$ and $T_{max} (K)$, exceed the afore-said thresholds. Before moving on, it must also be specified that both the cases of HVAC system turned off and operating (i.e. refreshing the air when $T_a > 20^\circ\text{C}$ and heating it when $T_a < 20^\circ\text{C}$) have been considered. In particular, the first case simply implies $T_{cabin} = T_a$, whereas the second coincides with $T_{cabin} = 20^\circ\text{C}$ (for both cooled and heated air). Finally, it must be remembered that, as mentioned in subchapter 4.2.1 and successively explained in chapter 6., the power necessary for the functioning of the HVAC system (and of the related fan) has not been considered. Back to the sensitivity analysis, tables 5.6 and 5.7 resume the outcomes obtained, by highlighting in green the conditions satisfied, in red the problematic ones and in yellow those not evaluable. From the examination of these two tables, several interesting considerations can be made. Primarily, it can be observed that only the temperatures at the two extremes (especially those at the hot side) introduce some issues (red cells); moreover, the solely operation of the HVAC (without the active intervention of the BTMS) reduces the number of critical events that take place both at low and high ambient temperatures (table 5.7). This happens because the passive heating/cooling that occurs when $T_{cabin} = 20^\circ\text{C}$ it is often sufficient to maintain the battery within its ideal thermal range. Moreover, in some cases, this fact also allows the battery to travel more than 200000 km, which were not guaranteed with the HVAC turned off (as for the WLTP at 30°C, with $n_{pass} = 1$). Another interesting aspect regards the impact of low temperatures on the battery functioning. Taking into consideration table 5.6 and remembering the assumptions made at the beginning of this subchapter (battery pre-heated for $T_a < 15^\circ\text{C}$), it can be noticed that only one driving mission (RWD03) implicates minimum battery temperatures lower than 15°C. In particular, this occurs for values of T_a equal to -5, 0 and 5°C. Consequently, the corresponding values of $L_{bat,km}$ cannot be calculated (cells in yellow) since the life model proposed by Wang [9] and adopted in this work is valid only for battery temperatures higher than 15°C.

<i>HVAC system operating</i> ($T_{cabin} = 20^{\circ}\text{C}$)			T_a ($^{\circ}\text{C}$)									
			-5	0	5	10	15	20	25	30	35	
<i>WLTP</i>	$L_{bat,km} \geq 200000 \text{ km}$	$n_{pass}=1$										
		$n_{pass}=5$										
	$T_{min} \geq 15^{\circ}\text{C}$	$n_{pass}=1$										
		$n_{pass}=5$										
	$T_{max} \leq 35^{\circ}\text{C}$	$n_{pass}=1$										
		$n_{pass}=5$										
<i>RTS 95</i>	$L_{bat,km} \geq 200000 \text{ km}$	$n_{pass}=1$										
		$n_{pass}=5$										
	$T_{min} \geq 15^{\circ}\text{C}$	$n_{pass}=1$										
		$n_{pass}=5$										
	$T_{max} \leq 35^{\circ}\text{C}$	$n_{pass}=1$										
		$n_{pass}=5$										
<i>FTP 75</i>	$L_{bat,km} \geq 200000 \text{ km}$	$n_{pass}=1$										
		$n_{pass}=5$										
	$T_{min} \geq 15^{\circ}\text{C}$	$n_{pass}=1$										
		$n_{pass}=5$										
	$T_{max} \leq 35^{\circ}\text{C}$	$n_{pass}=1$										
		$n_{pass}=5$										
<i>HWFET</i>	$L_{bat,km} \geq 200000 \text{ km}$	$n_{pass}=1$										
		$n_{pass}=5$										
	$T_{min} \geq 15^{\circ}\text{C}$	$n_{pass}=1$										
		$n_{pass}=5$										
	$T_{max} \leq 35^{\circ}\text{C}$	$n_{pass}=1$										
		$n_{pass}=5$										
<i>RWD01</i>	$L_{bat,km} \geq 200000 \text{ km}$	$n_{pass}=1$										
		$n_{pass}=5$										
	$T_{min} \geq 15^{\circ}\text{C}$	$n_{pass}=1$										
		$n_{pass}=5$										
	$T_{max} \leq 35^{\circ}\text{C}$	$n_{pass}=1$										
		$n_{pass}=5$										
<i>RWD03</i>	$L_{bat,km} \geq 200000 \text{ km}$	$n_{pass}=1$										
		$n_{pass}=5$										
	$T_{min} \geq 15^{\circ}\text{C}$	$n_{pass}=1$										
		$n_{pass}=5$										
	$T_{max} \leq 35^{\circ}\text{C}$	$n_{pass}=1$										
		$n_{pass}=5$										
<i>RWD04</i>	$L_{bat,km} \geq 200000 \text{ km}$	$n_{pass}=1$										
		$n_{pass}=5$										
	$T_{min} \geq 15^{\circ}\text{C}$	$n_{pass}=1$										
		$n_{pass}=5$										
	$T_{max} \leq 35^{\circ}\text{C}$	$n_{pass}=1$										
		$n_{pass}=5$										
<i>RWD06</i>	$L_{bat,km} \geq 200000 \text{ km}$	$n_{pass}=1$										
		$n_{pass}=5$										
	$T_{min} \geq 15^{\circ}\text{C}$	$n_{pass}=1$										
		$n_{pass}=5$										
	$T_{max} \leq 35^{\circ}\text{C}$	$n_{pass}=1$										
		$n_{pass}=5$										

Table 5.7: Battery sensitive analysis with the HVAC system operating.

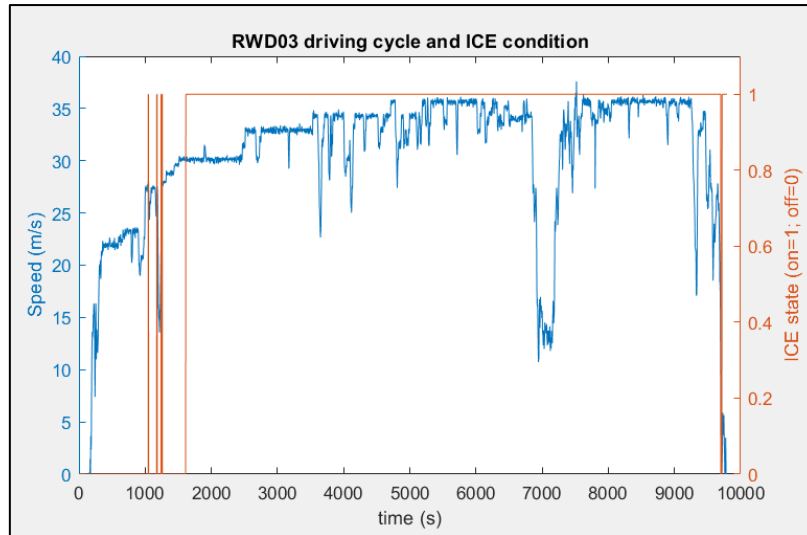


Figure 5.15: Intervention of the ICE while travelling the RWD03 in Electric mode, with $SOC_0=0.95$ and at $T_a=-5^\circ\text{C}$.

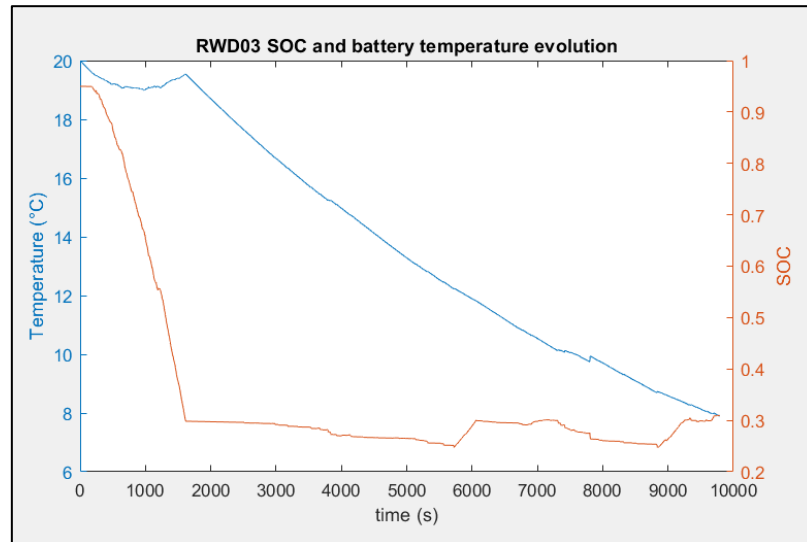


Figure 5.16: SOC and battery temperature variation while travelling the RWD03 in Electric mode, with $SOC_0=0.95$ and at $T_a=-5^\circ\text{C}$.

By examining more in detail the results of the RWD03 simulations, it can be understood why this is the only driving mission implying battery temperature lower than 15°C (when the HVAC does not operate). A first peculiarity regards the fact that the RWD03 travels the longest distance (296 km, table 5.1) among the eight missions considered. Therefore, as figures 5.15 and 5.16 show, after a first trait, until $SOC=0.3$ (i.e. around 1600 s), in which the traction is mainly provided by the MGP4, it follows a long charge sustaining phase, where the high level RB controller alternates moments in Hybrid mode (in which the SOC descends slowly up to 0.25) to others in

E-save mode (in which the SOC increases back to 0.30). Therefore, on the whole, the rate of use of the battery while travelling the RWD03 is not so substantial and this aspect also explains why, for any temperature considered in the sensitivity analysis, this driving mission always guarantees a battery lifetime larger than 200000 *km*. Consequently, after the charge depleting phase, in which intense Joule's heat is generated, the battery temperature (figure 5.16) dramatically drops because the battery pack is employed less (traction mainly provided by the ICE) and the passive cooling due to the surrounding air is no more balanced by the internal generation of heat. Conversely, when the HVAC system operates and maintains T_{cabin} at 20°C, this transfer of heat from the battery to the surrounding air is more restrained and the temperature, evidently, cannot go below the lower limit (table 5.7). Consequently, for cold climate conditions and HVAC system turned off, it may be necessary to employ the heating pads while travelling. However, since the assumptions made in this analysis are not particularly significant for exploring the battery functioning at low temperature, it has been employed a simple strategy for managing the heating system, consisting in switching on the pads every time the battery temperature reaches $T_{Hson} = 15^{\circ}\text{C}$ (obviously, only for those cases in which $T_a < 15^{\circ}\text{C}$) and maintaining them in this state up to $T_{Hsoff} = 16^{\circ}\text{C}$. In particular, it has been chosen not to optimize the employment of the heating pads since the conditions simulated, that are battery pre-heated, $SOC_0 = 0.95$ and Electric mode selected (which imply a maximum use of the battery and, consequently, higher Joule's heat, that, to some extent, opposes the achievement of low temperatures), do not allow the realization of exhaustive and general reflections about cold temperature operating management. In any case, the strategy adopted solves the RWD03 issues occurring with the HVAC system off.

Instead, moving to the simulations conducted at high temperatures, completely different considerations can be done. In fact, the results obtained at these conditions are particularly interesting. As first aspect, it is possible to observe that for several driving missions, even if the battery does not surpass the upper thermal limit of 35°C, the battery is not able to provide a $L_{bat,km}$ higher than 200000 *km*. In fact, as specified in subchapter 4.3. (also by means of figure 4.7), the hot portion of the ideal thermal range of employment of Li-ion cells can already notably affect battery duration. Moreover, although not illustrated by means of tables, even if the cooling system was used, although normally not expected for battery temperatures below 35°C, it could

be observed that, in many cases, the increment of $L_{bat,km}$ due to this intervention would not be enough for exceeding the imposed constraint of 200000 km. Actually, for the employing of the cooling system with the HVAC system off (plausible condition since this latter is controlled by the passengers), it could occur that the $L_{bat,km}$, rather than increases, results smaller than the value without cooling. Specifically, this can happen because chilling with an air flow at ambient temperature is not particularly efficient and, consequently, if the operating temperatures T_{CSon} and T_{CSoff} are not chosen properly, it is possible that the higher electric load due to the functioning of the cooling fan (Fan2 in figure 4.5), requesting a power P_{fan} , is not offset by an effective reduction of battery temperature; consequently, the battery simply ages faster because not cooled enough. Obviously, it is legitimate to present charges against the effectiveness of the air cooling system; however, it must be remembered that the actual most resounding aspect among the previous considerations is that an energy management (currently dictated by the default high level RB controller) valid at $T_a=25^\circ\text{C}$ can be no more suitable at $T_a=30^\circ\text{C}$ (as tables 5.6 and 5.7 testify). Therefore, little temperature variations can really undermine battery duration; consequently, the battery thermal management cannot be underestimated. Moreover, still reasoning on tables 5.6 and 5.7, if on the one hand it is clear that the more the temperature increases, the more problematic becomes the employment of the battery, on the other one evaluating the impact of the different driving missions results more arduous. In particular, this aspect can be clarified by introducing some values from the simulations. Taking into account table 5.6, in particular the compliance of the $L_{bat,km}$ obligation at $T_a=30^\circ\text{C}$ for the driving missions *FTP 75* (figure 5.3) and *HWFET* (figure 5.4), the following values are obtained: with $n_{pass} = 1$, *FTP 75* permits to travel around 182000 km whereas *HWFET* about 175000 km; with $n_{pass} = 5$, instead, the battery provides in both cases around 173000 km. Therefore, if for the case with only the driver the *HWFET* results more critical than the *FTP 75*, with five passengers these two driving missions appears comparable. Although these outcomes could sound weird, they actually make sense by remembering that the *MGP4* is characterized by a limited value of maximum power (60 hp). As a consequence, simulating conditions particularly power demanding (as, for example, by simply incrementing n_{pass} or changing the driving mission in question) could not

imply a significant reduction of battery lifetime, but simply a growth of fuel consumption because, as specified in 3.4. *Default Rule-Based EMS*, the EMS performs a passage to the Hybrid mode every time the power requested cannot be provided in pure-electric (i.e. the ICE intervenes in place of the MGP4).

Consequently, in order to solve the criticalities related to battery employment at high ambient temperatures, since the question results rather intricate, it is necessary to reason on a large number of different cases; however, it is clearly unthinkable to analyze each case one at a time. For this reason, as the following chapter illustrates, it has been decided to implement an optimization of the high level RB controller (i.e. the EMS) that includes the management of the cooling system (without being necessarily constrained to the specific cooling solution adopted in this work) and considers all the eight driving missions previously introduced with the aim to guarantee an adequate duration of the battery, evidently, without forgetting the real reason of vehicles electrification, that is the reduction of emissions (i.e. fuel consumptions).

6. PSO Implementation

The reflections made in the previous chapter have shown the need to realize an optimization (based on all the driving missions introduced) that allows the attainment of a new online EMS able to avoid the problematic overexploitation of the battery and, at the same time, to guarantee low fuel consumptions. In particular, as this chapter illustrates, these objectives have been reached by implementing a PSO. However, before entering into the details of the specific case considered in this work, it is necessary to introduce briefly the general concepts at the basis of PSO.

6.1. PSO Theoretical Basics

As already underlined in chapter 2. *State of the Art*, the PSO, first introduced in 1995 by Kennedy and Eberhart [27], is a metaheuristic based on the social behavior that is possible to observe in nature for different group of animals. In fact, when looking for the optimal solution, the PSO employs a procedure that is analogous to that used by a social group of birds or fish, who finds its strength in the constant communication among its members (particles) and in their consequent continuous learning (concept of personal and global best).

In particular, each particle finds itself in a N-dimensional domain D^N , that delimits the space in which the optimal solution is searched. Specifically, N indicates the number of parameters that intervene in the optimization problem. Speaking in terms of a generic p-particle (with $p=1,\dots,P$ and P equal to the total number of particles), its position in D^N in a generic instant t_i (with $i=1,\dots,I$ and I equal to the total number of iterations that is desired to perform) is indicated by $d_p^N(t_i)$. However, this position is not fixed, but varies according to the p-particle velocity $v_p^N(t_i)$, that rather than a velocity indicates a displacement; in fact, $d_p^N(t_i)$ and $v_p^N(t_i)$ have the same unit of measurement. Moreover, $v_p^N(t_i)$ varies in time as well. Specifically, in order to

compute the new values of p-particle position $d_p^N(t_{i+1})$ and velocity $v_p^N(t_{i+1})$ at the new instant t_{i+1} , the following equations can be used:

$$v_p^N(t_{i+1}) = wv_p^N(t_i) + r_1c_1(d_{p,best}^N - d_p^N(t_i)) + r_2c_2(d_{G,best}^N - d_p^N(t_i)) \quad (46)$$

$$d_p^N(t_{i+1}) = d_p^N(t_i) + v_p^N(t_{i+1}) \quad (47)$$

In equation (46), the new value of p-particle velocity $v_p^N(t_{i+1})$ has three contributes (figure 6.1): an inertia term $wv_p^N(t_i)$, that quantifies the influence of the previous velocity on the new one, a cognitive component $r_1c_1(d_{p,best}^N(t_i) - d_p^N(t_i))$, that depends on the personal best performance of the p-particle, and a social component $r_2c_2(d_{G,best}^N(t_i) - d_p^N(t_i))$, that is related to the global best performance of the entire group of particles.

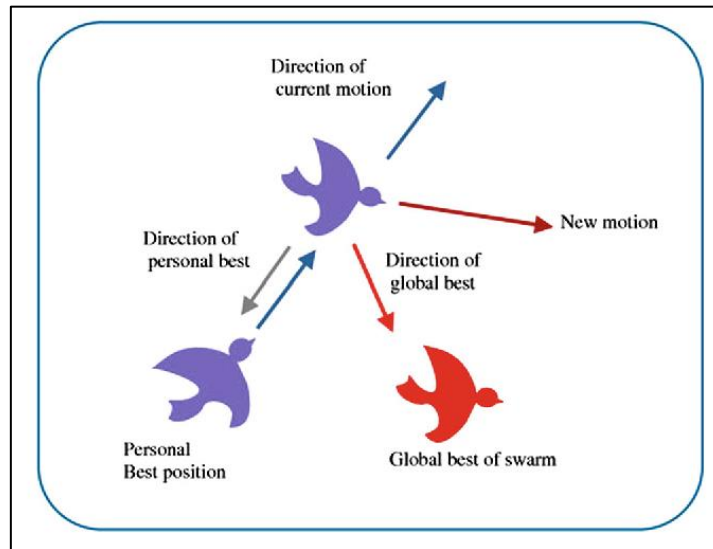


Figure 6.1: Schematic representation of the updating of particle velocity. Source: [i].

In particular, w is the inertia coefficient, r_1 and r_2 are two different values among 0 and 1, which are randomly chosen at each iteration, c_1 and c_2 are respectively the personal and the social acceleration, whereas $d_{p,best}^N(t_i)$ and $d_{G,best}^N(t_i)$ are the personal (of the p-particle) and the global (of the entire group of particles) best positions.

By adopting the Clerc and Kennedy PSO version [27], the following relations can be introduced:

$$\chi = \frac{2k}{|2 - \Phi - \sqrt{\Phi^2 - 4\Phi}|} \quad \text{with } 0 \leq k \leq 1 \quad (48)$$

$$\Phi = \Phi_1 + \Phi_2 \geq 4 \quad (49)$$

$$w = \chi \quad (50)$$

$$c_1 = \chi\Phi_1 \quad (51)$$

$$c_2 = \chi\Phi_2 \quad (52)$$

where all the new parameters are commonly called ‘‘Clerc and Kennedy’s constriction coefficients’’. With respect to this work, it was used $k = 1$ and $\Phi_1 = \Phi_2 = 2.05$.

Therefore, it only remains to specify how $d_{G,best}^N(t_i)$ and $d_{p,best}^N(t_i)$ are determined. Hypothesizing that the problem that is desired to be optimize can be expressed as a minimization problem (as the case considered in this work, that is specified in the following subchapter), the optimal solution is the one implying the smallest value of a cost function defined on the domain D^N . In particular, this cost function, indicated as $C(d^N)$, allows to quantify the goodness of the generic p-particle position $d_p^N(t_i)$ in the generic instant t_i . Consequently, due to the fact that each particle keeps memory of its past personal best, at each instant (i.e. for any new position) the p-particle performs the following operation at each iteration:

$$C(d_{p,best}^N(t_i)) = \min\left(C(d_{p,best}^N(t_{i-1})), C(d_p^N(t_i))\right) \quad (53)$$

In this way, the p-particle best position is evaluated (and potentially updated) at each instant. Moreover, since the particles also communicate among them, they compare constantly at each instant t_i their personal best positions, in order to evaluate the global best of the entire group:

$$\begin{aligned}
& C(d_{G,best}^N(t_i)) \\
& = \min\left(C(d_{G,best}^N(t_{i-1})), C(d_{1,best}^N(t_i)), \dots, C(d_{p,best}^N(t_i)), \dots, C(d_{P,best}^N(t_i))\right) \quad (54)
\end{aligned}$$

After the last iteration, the resulting $d_{G,best}^N(t_i)$ is then considered as the optimal solution of the problem. Obviously, in the exposed procedure, a wide range of control operations is also necessary, here not described since not fundamental in the understanding of PSO (as, for example, the setting of the maximum and minimum values of v_p^N). If more details are desired, it is possible to consult *Yarpiz* website [27]. In any case, in order to have the PSO working properly, it is necessary to choose really carefully the cost function $C(d^N)$, the explored domain D^N and the numbers of particles P and of iterations I.

6.2. Problem Characterization

Due to the fact that, in subchapter 5.3. *Sensitivity Analysis Considerations*, the necessity to optimize the high level RB controller, which must surely include a thermal management of the battery, has been discussed solely in broad terms, more information will be now provided. In effect, before undertaking the optimization phase, a clear overview of the considered problem must be furnished.

In particular, as already disclosed, the data collected in tables 5.6 and 5.7 have highlighted as the employment of the battery at high, but plausible, ambient temperature can reduce the duration expected from the vehicle ESS. Moreover, the results obtained are particularly astonishing since they refer to thermal ranges normally considered innocuous for battery deterioration. Consequently, although in tables 5.6 and 5.7 are not reported precise values, but only the fulfillment of some conditions, it results evident anyway that the EMS successfully employed at $T_a=25^\circ\text{C}$ is no more appropriate at $T_a=30^\circ\text{C}$, let alone at $T_a=35^\circ\text{C}$. Therefore, in order to effectively guarantee both a sufficient battery duration and an acceptable fuel economy, it turns out to be indispensable the adaptation of the EMS to the different external temperatures. In particular, this adaptation, which is desired to be optimal, must bring into play both T_{CSon} and T_{CSoff} , whose values would depend, evidently, on T_a and on the HVAC system state (operating or not). However, as already mentioned, it is not said that acting solely on the BTMS functioning is sufficient for satisfying the

condition imposed. Obviously, this is particularly true for the cooling system adopted in this work, but more efficient solutions can imply similar considerations. Consequently, it could be also necessary to operate actively and directly on the high level RB controller, modifying its characteristics. Consequently, since the cases considered take into account the Electric mode, the operation of the high level controller with this mode selected must be free to vary conveniently with T_a and the HVAC state. In particular, since the passage towards the Hybrid mode due to power limitations cannot be changed (since related to the MGP4 power size), it only remains alterable the SOC of transition from charge depleting to charge sustaining phase, initially set at 0.30 (subchapter 3.4.) and now indicated as SOC_{var} . Therefore, mindful of the outcomes of tables 5.6 and 5.7, an optimization of the aforementioned three variables (T_{CSon} , T_{CSoff} and SOC_{var}) has been conducted for four values of T_a , namely 26°C, 29°C, 32°C and 35°C, and for both the cases of air conditioning on and off (HVAC system states). In this way, a total of three two-dimensional lookup tables representing the new high level RB controller and outputting the values of T_{CSon} , T_{CSoff} and SOC_{var} , by entering the values of ambient temperature and HVAC state, have been obtained by following the procedure exposed in the following subchapter.

However, before moving on, it is necessary to make a small clarification. As specified in 4.2.1. *Air Cooling System*, the operation of the HVAC system and of the dedicated fan (Fan1 in figure 4.5) weigh on the battery and should increase the power effectively outputted by this component. Nevertheless, since the activation of the air conditioning is not directly aimed at cooling the battery, but at increasing the passengers' climate comfort and, therefore, it would be employed regardless of the necessity to cool the battery, it was chosen to ignore the little increment of thermal load, from the HVAC point of view, due to the chilling of the battery and to consider as costless (i.e. no additional electric energy consumptions) the consequent advantages in cooling the battery. Specifically, this choice has been taken in order to make more equitable the comparison between the consumptions obtained with the two possible cooling conditions ($T_{cabin}=T_a$ and $T_{cabin}=20^\circ C$) related to the HVAC state.

6.3. Cost Function and Research Domain Determination

As disclosed, the reasons that make the PSO extremely popular are certainly its adaptability to many different problems and the simplicity of its mathematics. However, in order to obtain a genuine optimal solution it is necessary that the cost function, the domain analyzed and the numbers of particles and iterations are chosen suitably. Generally, with respect to the number of iterations I and of particles P , their effectiveness is simply evaluated by repeating several times the same optimization problem and by reducing or increasing each time both I and P . In particular, their proper values are those that allow to reach a satisfying solution in a reasonable amount of time. In fact, the solution researched is desired to be satisfactory, because the metaheuristics (as the PSO) difficultly provide the actual best solution of the problem considered.

As far as the cost function is concerned, instead, the question becomes more complex. In fact, a clear overview of the problem considered, together with predetermined objectives, is mandatory. Therefore, with respect to this work, before introducing the cost function, the purposes of the optimization must be declared clearly.

As shown in the previous subchapter, an optimization of T_{CSon} , T_{CSoff} and SOC_{var} for different values of ambient temperature must be performed by taking into account all the eight driving missions considered. In fact, in subchapter 5.3. *Sensitivity Analysis Considerations*, it was highlighted that, in order to obtain an optimal result as general as possible, the problem cannot be focused on one only driving cycle. Consequently, it is possible to speak in terms of generic driving mission j (obviously with $j=1, \dots, 8$).

With respect to the authentic object of the optimization, it is evident that the battery lifetime cannot be considered alone. In fact, the largest lifetime possible would trivially imply that the battery is not used. Therefore, remembering that the main reason of transports electrification is reducing their environmental impact, it appears obvious that the fuel economy must be taken into account as well. In fact, the objective of this optimization process is to find out the strategy that permits to obtain the lowest fuel consumption, without undermining battery duration.

Nevertheless, although the cost function must thus guarantee a sufficient value of battery life and a reasonable fuel consumption, above all it must be deduced and based on real/reasonable facts. In fact, performing an optimization by using a cost

function deriving from unrealistic assumptions can lead to useless results. Hence, with respect to this latter aspect, which qualifies the reliability of the PSO implemented in this work, two researches come to the aid of the debated problem. In particular, the health insurer *UnipolSai* (2019) [40] has pointed out that the average quantity of km travelled by a car in Italy per day (only counting the days in which the vehicle is effectively used) is around 41 km. Moreover, the association *Anci* has observed in its press release (2016) [41] that, still in Italy, the average number of passengers per car is equal to 1.33. Although these two pieces of information can appear uninteresting, they are actually fundamental in the definition of the cost function here employed. In fact, the simulations referring (at a certain ambient temperature) to the generic driving mission j , but related to two different load conditions that consist in the two mentioned extreme cases (i.e. driver only and 5 passengers), can see a combination of their values of battery lifetime in km (respectively indicated as $L_{bat,km,driver_j}$ and $L_{bat,km,5pass_j}$) and of their fuel consumptions in $l/100km$ (from now on referred as $f_{100km,driver_j}$ and $f_{100km,5pass_j}$) by using weight factors based on the average number of passengers per car (therefore, respectively 0.9175 and 0.0825). In this way, for the generic driving mission j it is possible to legitimately fuse together the values referring to the two load conditions considered in the quantities L_{bat,km_j} and f_{100km_j} .

Therefore, once every driving mission has been equipped with the afore-said quantities, it is possible to pass to the correlation of all the driving missions among them. Specifically, to do this it is necessary to remember the average value of 41 km/day [40] and the commonly employed lower limits of acceptable battery lifetime duration, i.e. 200000-300000 km [22]. Thus, the following choices have been made: the battery must guarantee at least 200000 km in whatever driving mission, whereas, with respect to the vehicle most probable employment (41 km/day), that can be obtained from an appropriate combination of the eight missions considered and whose corresponding battery life is indicated as $L_{bat,km,ave}$ (km), a minimum limit of 300000 km is imposed. Obviously, these threshold values could be chosen differently and, in this regard, interesting considerations will be made in chapter 8. *Conclusions*. Back to the current case, the following constraints have therefore been set: $L_{bat,km_j} \geq$

200000 *km* for each driving mission and $L_{bat,km,ave} \geq 300000$ *km* for all the missions considered together and constituting an average employment of the vehicle around 41 *km/day*. Although the conditions just declared are not directly related to the cost function employed in this work, which, as later illustrated, focuses on fuel consumptions (in $l/100km$) only, it was imposed that, in case they are not satisfied, a very high value (e.g. 1000 $l/100km$) is regardless assigned as result of the cost function.

Before specifying the cost function considered, it is still necessary to illustrate how the value of $L_{bat,km,ave}$, referring to average daily distance, has been evaluated. Specifically, each driving mission has been considered to be performed in a different day. Moreover, four of the eight missions (namely *RTS 95*, *FTP 75*, *HWFET* and *RWD06*) have been considered repeated in two different days. In this way, the number of total days/trips becomes 12 and by making the average of the *km* travelled per day (by means of table 5.1) it can be obtained the wished value of 41 *km/day*. This means that when the eight driving missions combine among them their values of battery lifetime L_{bat,km_j} for obtaining $L_{bat,km,ave}$ (in order to check the life constraint of 300000 *km*) a weight factor w_{days_j} , whose different values are based on the number of days the driving mission *j* is repeated (i.e. $1/12$ for the driving missions effectuated one day only and $1/6$ for the others), is employed. In addition, the vehicle use that results from these assumptions suitably reflects a possible reality since it is constituted (as table 5.1 shows) by several medium-short trips (coinciding to a probable house-work routine), with sporadic long ones (corresponding to particular and less frequent occasions).

Obviously, besides the $L_{bat,km,ave}$ quantity, it is also possible to introduce $f_{100km,ave}$ ($l/100km$), that concerns the fuel consumed travelling the 41 *km/day* and can be computed in a way analogous to the one just specified for $L_{bat,km,ave}$ (i.e. by using w_{days_j}), but by using f_{100km_j} instead of L_{bat,km_j} . Specifically, $f_{100km,ave}$ has been associated to the cost function, whose outcome must be minimized by means of the optimization procedure. In fact, this quantity has been considered the most representative in order to quantify the fuel effectively consumed by the vehicle.

Obviously, it could be disapproved the fact of considering, in the cost function, solely the fuel consumptions and not the electric energy provided by the battery; however, the choice made here can be justified by considering that the electric energy consumptions are indirectly checked by the fuel consumptions and by the battery lifetime values. In fact, if the battery is discharged faster, the passage between Electric mode and Hybrid mode happens early, with consequent higher fuel consumptions; moreover, generally speaking, it is not a problem to consume electric energy as long as this fact does not increase the fuel consumed or reduce the battery lifetime below the limits.

Therefore, starting from the afore-said considerations, a PSO was conducted for each value of T_a taken into account (26°C, 29°C, 32°C and 35°C), one at a time, and for both the cases of air conditioning in operation and turned off (that are simply translated in a different value of T_{cabin}). With respect to the number of particles and iterations, $P=30$ and $I=20$ have been used. Afterward, as size N of the domain of research D^N it was elected 3 since the cost function computation (for each combination of T_a and T_{cabin}) is related to the quantities T_{CSon} , T_{CSoff} and SOC_{var} . Therefore, these quantities constitutes the PSO domain variables. Consequently, the only essential question that remains unspecified is the extension of D^N . Hence, it could be reasonably used the following solution:

$$D^N: \begin{cases} T_a \leq T_{CSon} \leq 40^\circ C \\ T_{cabin} \leq T_{CSoff} < T_{CSon} \\ 0.25 \leq SOC_{var} \leq 0.95 \end{cases}$$

in which the upper T_{CSon} limit of 40°C has been chosen in order to include, also for $T_a=35^\circ C$, the possibility of no active cooling, whereas the lower SOC_{var} limit of 0.25 (but not beyond in order to prevent the achievement of too low SOC values) has been introduced in order to question the SOC value of 0.30 (marking the passage from charge depleting to charge sustaining modality) imposed by the default EMS, which, as specified at the end of subchapter 3.4., was set with rationality, but not optimally. However, performing the PSO with the afore-said D^N implies some problems in the solutions obtained. In fact, as it commonly occurs when employing simplified/standard version of PSO (as that by Clerc and Kennedy) [42], the solutions

found often refer to local minimums of the cost function. Consequently, in literature, several PSO variants are proposed to solve this issue. However, with respect to the specific case in question, it was observed that this criticality occurred because the domain D^N was not adequately explored. In particular, considering momentarily an equivalent unidimensional ($N = 1$) generic D^N (blue line in figure 6.2) in which it is searched the position corresponding to the minimum value of a generic cost function (red curve in figure 6.2), it was notice that the particles normally focused exclusively on the central part of D^N (yellow area in figure 6.2).

To solve this issue, it was then decided to expand the domain (indicated as \bar{D}^N) and assigning to the cost function related to the new domain portions (not contained in D^N) the values resulting by computing the cost function in the closest limit of the previous D^N (red horizontal lines in figure 6.3). With this expedient, it is possible to exploring more extensively D^N , as the yellow area in figure 6.3 shows (with \bar{D}^N represented by a green line). In particular, thanks to this expedient, in case the optimal solution is found inside \bar{D}^N , but outside D^N , it is known that the optimal position is actually placed at the corresponding D^N limit.

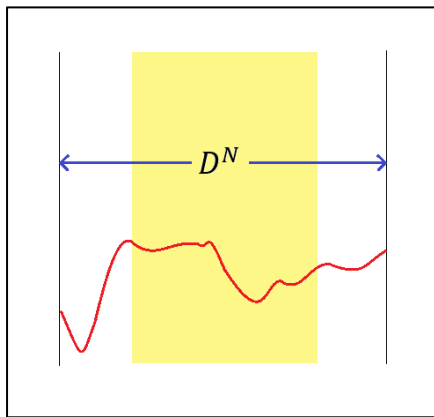


Figure 6.2: D^N portion effectively explored by the particles when D^N is used.

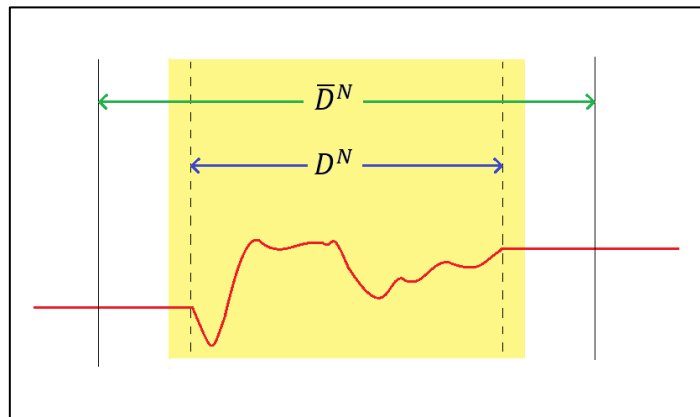


Figure 6.3: D^N portion effectively explored by the particles when \bar{D}^N is used.

Back to $N = 3$, the \bar{D}^N thus employed in this work is the following one:

$$\bar{D}^N: \begin{cases} T_a - 2^\circ\text{C} \leq T_{CS,on} \leq 40^\circ\text{C} \\ T_{cabin} - 2^\circ\text{C} \leq T_{CS,off} < T_{CS,on} + 2^\circ\text{C} \\ 0.25 \leq SOC_{var} \leq 0.95 \end{cases}$$

Consequently, it is now possible to move to the effective PSO implementation. In particular, the generic p-particle position (with $p=1,\dots,30$) at the generic instant t_i (with $i=1,\dots,20$) turns out to be:

$$d_p^N(t_i) = [T_{Csonp}(t_i), T_{Csoffp}(t_i), SOC_{varp}(t_i)] \quad (55)$$

with:

$$d_p^N(t_i) \in \bar{D}^N$$

With respect to the cost function constraints, instead, the lifetime values $L_{bat,km,p_j}(t_i)$ (with $j=1,\dots,8$ and referring individually to the different driving missions) and $L_{bat,km,avep}(t_i)$ (concerning all the driving missions combined together) related to the generic $d_p^N(t_i)$ are computed as follows:

$$L_{bat,km,p_j}(t_i) = 0.9175 \cdot L_{bat,km,driverp_j}(t_i) + 0.0825 \cdot L_{bat,km,5passp_j}(t_i) \quad (56)$$

$$L_{bat,km,avep}(t_i) = \sum_{j=1}^8 w_{days_j} L_{bat,km,p_j}(t_i) \quad (57)$$

Afterward, according to the previous reflections, the cost function can be expressed as:

$$\begin{aligned} C(d_p^N(t_i)) &= f_{100km,ave}(d_p^N(t_i)) \\ &= \sum_{j=1}^8 \left[w_{days_j} f_{100km,p_j}(t_i) + 1000^l / 100km \cdot (L_{bat,km,p_j}(t_i) < 200000km) \right] \\ &\quad + 1000^l / 100km \cdot (L_{bat,km,ave}(t_i) < 300000km) \quad (58) \end{aligned}$$

Therefore, it is finally possible to execute the PSO, procedure that must be repeated for each possible combination of T_a and T_{cabin} and whose results are precisely illustrated in the following chapter.

7. Calibration Results

The optimization problem illustrated in the previous chapter, whose resolution has requested around 120 hours (by means of a notebook computer equipped with a 16 GB RAM and an Intel Core i7-1065G7 processor of 1.3 GHz), has allowed to obtain the values collected in tables 7.1 and 7.2, which refer (for each possible combination of T_a and T_{cabin}) to the best T_{CSon} , T_{CSoff} and SOC_{var} values (i.e. $T_{CSon,best}$, $T_{CSoff,best}$ and $SOC_{var,best}$) guaranteeing, for the thermal conditions in question, the lowest $f_{100km,ave}$ (i.e. $f_{100km,ave,best}$).

<i>HVAC system turned off</i> ($T_{cabin} = T_a$)	T_a (°C)			
	<u>26</u>	<u>29</u>	<u>32</u>	<u>35</u>
$T_{CSon,best}$ (°C)	-	29.5	32.6	35.4
$T_{CSoff,best}$ (°C)	-	29.4	32.4	35.3
$SOC_{var,best}$	0.40	0.83	0.88	0.90
$f_{100km,ave,best}$ (l/100km)	1.63	3.70	4.77	5.10

Table 7.1: PSO outcomes for HVAC system turned off.

<i>HVAC system operating</i> ($T_{cabin} = 20^\circ\text{C}$)	T_a (°C)			
	<u>26</u>	<u>29</u>	<u>32</u>	<u>35</u>
$T_{CSon,best}$ (°C)	-	29	32	35
$T_{CSoff,best}$ (°C)	-	23.9	25.7	27.5
$SOC_{var,best}$	0.40	0.40	0.82	0.86
$f_{100km,ave,best}$ (l/100km)	1.63	1.63	3.60	4.40

Table 7.2: PSO outcomes for HVAC system operating.

As already mentioned, these outcomes, which refer to the new optimal high level RB controller (later specified), must be converted in lookup tables in order to be introduced in the *Simulink* vehicle model. However, since at $T_a=26^\circ\text{C}$ the intervention of the cooling system is not requested neither with the HVAC system on nor off, it is evident that from the data collected in tables 7.1 and 7.2 there is not enough information to indicate, by means of an interpolation, the optimal operating temperature $T_{CSon,best}$ and $T_{CSoff,best}$ for T_a between 26°C and 29°C . Moreover, especially for the case with the air conditioning functioning (table 7.2), the gap between the $SOC_{var,best}$ values for T_a equal to 29°C and 32°C is too steep and could conceal particular trends. Consequently, due to the afore-said reflections, it has been decided to integrate tables 7.1 and 7.2 with the PSO results (requiring 90 additional hours of simulation time) related to ambient temperatures of 27°C , 28°C and 30°C , as reported in tables 7.3 and 7.4.

<i>HVAC system turned off</i> <i>($T_{cabin} = T_a$)</i>	T_a ($^\circ\text{C}$)		
	<u>27</u>	<u>28</u>	<u>30</u>
$T_{CSon,best}$ ($^\circ\text{C}$)	28.2	28.5	30.4
$T_{CSoff,best}$ ($^\circ\text{C}$)	27.9	28.4	30.3
$SOC_{var,best}$	0.79	0.81	0.84
$f_{100km,ave,best}$ ($l/100km$)	2.95	3.31	4.03

Table 7.3: Integration to PSO outcomes for HVAC system turned off.

<i>HVAC system operating</i> <i>($T_{cabin} = 20^\circ\text{C}$)</i>	T_a ($^\circ\text{C}$)		
	<u>27</u>	<u>28</u>	<u>30</u>
$T_{CSon,best}$ ($^\circ\text{C}$)	27	28	30
$T_{CSoff,best}$ ($^\circ\text{C}$)	25.3	24.8	24.7
$SOC_{var,best}$	0.40	0.40	0.79
$f_{100km,ave,best}$ ($l/100km$)	1.63	1.63	3.05

Table 7.4: Integration to PSO outcomes for HVAC system operating.

Consequently, from the information contained in tables 7.1-7.4, it is possible to obtain the curves (lookup tables) in figures 7.1-7.3, in which, instead of the quantities $T_{CSon,best}$, $T_{CSoff,best}$ and $SOC_{var,best}$, have been represented, over T_a , the more significative variations $\Delta T_{CSon,best}=T_{CSon,best}-T_a$, $\Delta T_{CSoff,best}=T_{CSoff,best}-T_a$ and $\Delta SOC_{var,best}=SOC_0 - SOC_{var,best}$. In figure 7.4, instead, it is reported the resulting $f_{100km,ave,best}$ evolution over T_a .

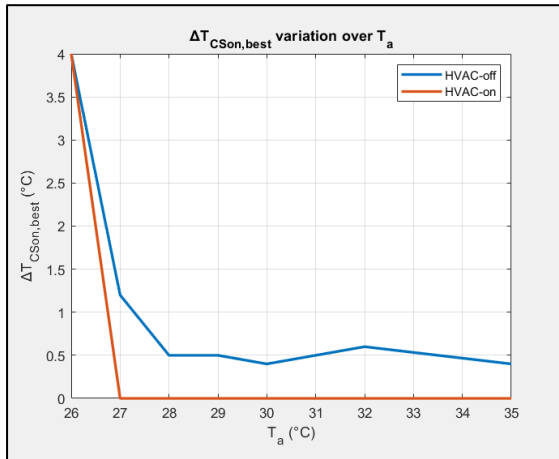


Figure 7.1: $\Delta T_{CSon,best}$ variation over T_a .

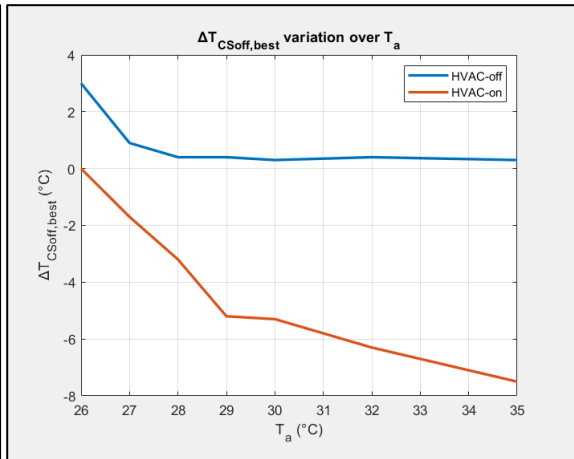


Figure 7.2: $\Delta T_{CSoff,best}$ variation over T_a .

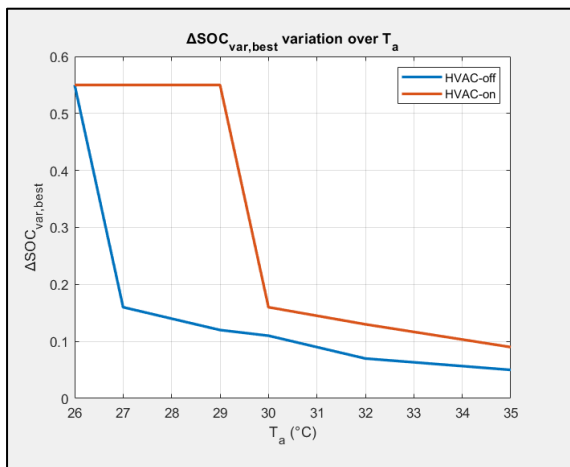


Figure 7.3: $\Delta SOC_{var,best}$ variation over T_a .

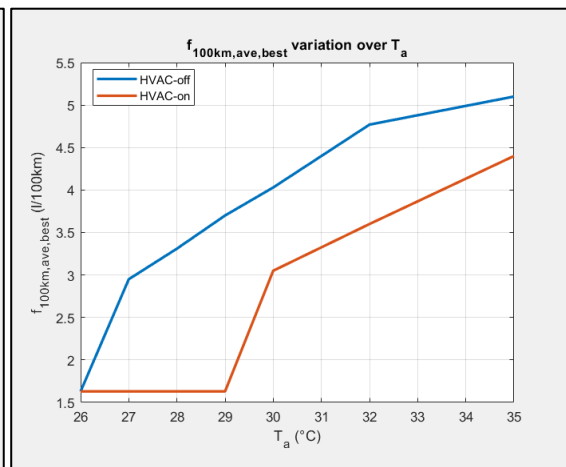


Figure 7.4: $f_{100km,ave,best}$ variation over T_a .

Although in the following subchapters more specific considerations will be done, it is important that some aspects are highlighted now. As it can be intuitively deduced, the higher is T_a , the more urgent becomes the need to chill the battery; therefore, $\Delta T_{CSon,best}$ decreases (figure 7.1) since it is requested to start cooling the battery sooner, $\Delta T_{CSoff,best}$ decreases as well (figure 7.2) since it is necessary to cool the

battery longer and, similarly, $\Delta SOC_{var,best}$ reduces (figure 7.3) because, in order to limit the battery deterioration, it is permitted to exploit the battery less. Consequently, this latter aspect implies unavoidably that the minima fuel consumptions compatible with battery aging supervision increases with T_a (figure 7.4). Obviously, these overall trends, which can influence among them, are also governed by other factors. For example, by taking into account the evolution of $\Delta T_{CSon,best}$ for the HVAC system turned off (blue line in figure 7.1) it can be observed that, from $T_a=28^\circ\text{C}$ on, its value remains practically fixed around 0.5°C , without decreasing with T_a increase. Specifically, this occurs because cooling with a difference of temperature (between battery and air flow rate) smaller than 0.5°C is not particularly efficient, given that some power (P_{fan}) is expended for realizing it. For the same reason, at the same T_a range, $\Delta T_{CSoff,best}$ oscillates around 0.4°C (blue line in figure 7.2).

Finally, it can be observed that the operation of the HVAC system, by lowering T_{cabin} value, improves the effectiveness of the cooling system (in particular, as figure 7.2 shows, it is possible to set $T_{CSoff,best}$ below T_a) and, consequently, it also allows (when compared to the case with HVAC system off) to exploit the battery longer (figure 7.3), fact that, evidently, corresponds to a lesser fuel consumption (figure 7.4).

7.1. Fuel Consumptions Minimization

From the PSO results collected in tables 7.1 and 7.2, it turns out that no cooling is necessary when $T_a=26^\circ\text{C}$. This fact does not astonish since, as observed in tables 5.6 and 5.7 (in subchapter 5.3. *Sensitivity Analysis Considerations*), an ambient temperature of 25°C allowed all the driving missions to be travelled without any problems. However, it can be observed that a $SOC_{var,best}$ of 0.40 (indicating the best passage from charge depleting to charge sustaining strategy), different from the default value of 0.30, is obtained for $T_a=26^\circ\text{C}$. This fact can be explained remembering that, as already specified in subchapter 6.3., the initial value of 0.30 was assigned reasonably, but without checking a minimization of fuel consumptions, differently from what done, instead, with the PSO. In particular, the reason why the fuel consumed with $SOC_{var}=0.40$ is lower than that with a value of 0.30 can be understood by reasoning on the RWD03 driving mission (figure 5.7). In fact, considering an

ambient temperature of 25°C and the two aforementioned values of SOC_{var} (i.e. 0.30 and 0.40), the respective SOC evolutions while travelling the RWD03 are reported in figure 7.5.

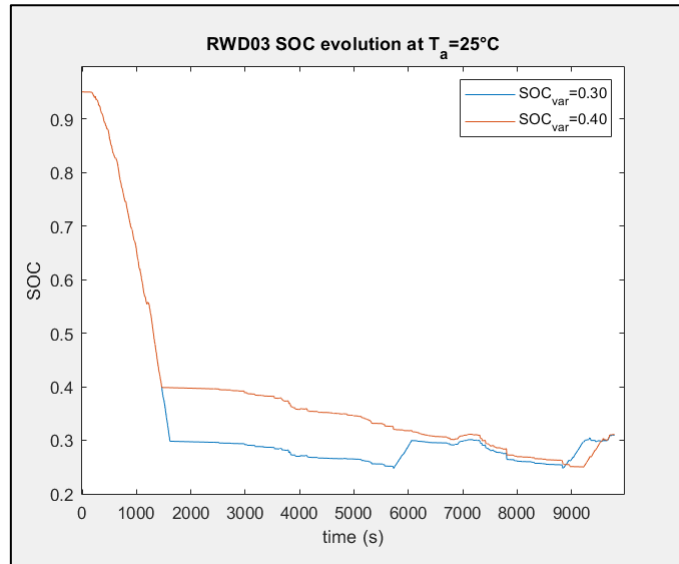


Figure 7.5: RWD03 SOC evolution with SOC_{var} equal to 0.30 and 0.40, at $T_a=25^\circ\text{C}$.

From figure 7.5, it can be observed that a SOC_{var} equal to 0.40 allows to avoid the first of the two particularly fuel consuming phases in E-save mode (in which the SOC increases from 0.25 to 0.30) that occur when $SOC_{var}=0.30$ and, at the same time, it does not move up excessively the passage to charge sustaining mode. Consequently, if on the one hand it becomes clear why $SOC_{var}=0.40$ coincides with the minima fuel consumptions, on the other one it can also be inferred that this result is particularly close to the RWD03 mission. In fact, as already highlighted, this driving mission is the longest one among those considered here (table 5.1); therefore, for climate conditions in which the battery can be exploited without any problems (i.e. $T_a \leq 26^\circ\text{C}$), the RWD03 is the one that impacts the most on fuel consumptions because the other missions, since far more shorter, are completely travelled in charge depleting. Considering then, for example, the already mentioned WLTP4 (which is long enough to always reach SOC values entailing the passage to charge sustaining strategy, figure 5.14), the related consumptions are far more reduced if a SOC_{var} of 0.30 is used instead of one of 0.40. Therefore, it is evident that, when there are not problems concerning battery ageing and, therefore, the SOC of passage from charge depleting

to charge sustaining mode (i.e. SOC_{var}) can be elected freely (focusing solely on fuel economy), it is fundamental to choose its value by means of an accurate analysis and compendium of different possible and significant long trips. However, as already specified, the purposes of this work is more oriented at quantifying how battery protection influences electric energy exploitation; therefore, without entering into the details of the considerations just made, but conscious of the strong influence of the driving missions chosen, $SOC_{var}=0.40$ has been considered as the best possible value of passage from Electric mode to Hybrid one. However, as the results reported in tables 7.1-7.4 show, it is not always possible to set SOC_{var} at 0.40 (in other words, 0.40 does not always coincide with $SOC_{var,best}$, but only when $T_a \leq 26^\circ C$); in fact, for some temperatures and to varying degrees with the state of HVAC plant, the constraints on battery life, in spite of the intervention of the cooling system, prevail on the fuel economy and raise the $SOC_{var,best}$ above 0.40, with a consequent increase of the minimum (best) value of fuel consumption, that, therefore, is no more fixed, but varies with the conditions of employment (ambient temperature) of the battery. Therefore, this reflection confirms the current literary trend that redefines fuel economy in order to protect the battery from fast degradation; however, as the results of the PSO show (although they can still be improved, as subchapter 7.3. illustrates), this reconsideration of fuel economy can be necessary even for little variations of temperature occurring within the ideal thermal range of batteries employment ($15^\circ C$ - $35^\circ C$ [7]). Moreover, it is interesting to analyze the impact of the cooling conditions on the fuel consumptions. In effect, as figure 7.4 illustrates, when the air conditioning is on, it is consumed less fuel than the case with the HVAC system off since the battery is rapidly brought to thermal conditions that allow a larger employment of the electric energy (figure 7.3) before aging issues brutally arise. Consequently, it intuitively follows that with a more effective cooling system (as a liquid one) lower fuel consumptions can be achieved.

7.2. Optimized Rule-Based EMS

Once conducted the PSO, it is possible to explicate the new high level RB controller that, unlike the default one, is able to safeguard battery life by including a management of the battery employment sensitive to the thermal conditions. However, it must be remembered that the optimization accomplished concerns high

ambient temperatures only; in fact, as already specified in subchapter 5.3. *Sensitivity Analysis Considerations*, the assumptions made for conducting the sensitivity analysis did not lend themselves well to perform an interesting and general optimization regarding battery employment at cold temperatures. Moreover, since the results obtained from the afore-said calibration are related to the vehicle employment with the Electric mode selected and $SOC_0=0.95$, before defining the new RB EMS it is necessary to make some considerations addressed to generalize the calibration outcomes to all the possible driving modes and SOC_0 values. With respect to the generalization of SOC_0 , it is possible to reason, as already done for the figures 7.1-7.3, in terms of $\Delta T_{C_{Son,best}}$, $\Delta T_{C_{Soff,best}}$ and $\Delta SOC_{var,best}$ (all varying over time); in this way, by using $\Delta SOC_{var,best}$, it is possible to release $SOC_{var,best}$ from the specific SOC_0 considered during the optimization. However, this latter assertion needs some elucidations. First of all, for the moment, it is still considered selected the Electric mode. Secondly, starting from whatever possible SOC_0 , $\Delta SOC_{var,best}$ can be effectively exploited as long as the SOC remains greater than 0.40, since, as already illustrated in the previous subchapter, fuel consumptions increase if the passage from charge depleting to charge sustaining mode is effectuating below this SOC value. Lastly, it must not be forgotten that, as already explained in subchapter 5.2., employing the battery at lower SOC implies a slightly larger degradation than that occurring, for a same employment, at higher SOC; nevertheless, since this difference was observed practically negligible, it can be concluded that the strategies valid with $SOC_0 = 0.95$ can also be used when starting from lower SOC_0 .

Moving then to the other two possible modes and considering the respective most critic conditions (according to table 5.4 in subchapter 5.2.), which are $SOC_0 = 0.95$ for the Hybrid mode and $SOC_0 = 0.21$ for the E-save one, and simulating them in all the eight driving missions, with $T_a=35^\circ\text{C}$ (the most critical thermal condition), for both the states of the HVAC system and with the objective to check if the corresponding values of $L_{bat,km}$ are higher than 200000 km (similarly to what done in subchapter 5.3. for the Electric mode selected and from $SOC_0 = 0.95$), it was observed that the E-save mode does not generate any problem, whereas the Hybrid one yes and, practically, in a way identical to the case with the Electric mode selected. In particular, this issue with Hybrid mode occurs because, according to the default EMS, as long as the SOC is higher than 0.60 the vehicle proceeds in Electric mode; therefore, the new

high level RB controller must consider also this aspect. A last consideration that is necessary to be done before moving on, is that all the SOC values of passage defined by the default controller could be optimized; however, their optimization has not been conducted here since it would not have included the thermal aspect, as this work want to do, and, moreover, analogously to the value of 0.40 for SOC_{var} , the quantities attained would not have been of general interest, since extremely influenced by the driving missions considered.

Consequently, the optimized high level RB controller remains similar to the default one (defined at the end of subchapter 3.4. *Default Rule-Based EMS*), but integrates it with the following features:

- When the Electric mode is selected, the automatic change to the Hybrid mode is no more performed at a SOC of 0.30, but of 0.40 (despite its strong dependence on the RWD03, as illustrated in the previous subchapter). However, according to figure 7.3, this passage to Hybrid mode can be anticipated to $SOC_{var,best}=SOC_0 - \Delta SOC_{var,best}$, depending on SOC_0 , T_a and HVAC system state. Moreover, the cooling system operates according to figures 7.1 and 7.2.
- When the Hybrid mode is selected, as long as the SOC is higher than 0.60, the vehicle proceeds in Electric mode. However, the return to the Hybrid mode can be moved up (again according to figure 7.3) to $SOC_{var,best}=SOC_0 - \Delta SOC_{var,best}$ in case this value is larger than 0.60. Furthermore, as long as the vehicle proceeds in the Electric mode (before moving definitely back to the Hybrid mode), the cooling system operates as stated by figures 7.1 and 7.2.

In this way, by means of overall larger fuel consumptions, but apparently minima for the achievement of the objectives preset (battery life constraints), it is possible to safeguard battery duration when exposed and used in different reasonable hot climate conditions.

7.3. High-Level Strategy

If on the one hand it is sure that, with the optimized EMS, the battery is able to provide, for any T_a and state of the HVAC system, at least 200000 km (actually around this quantity because of the interpolation present in the lookup tables reported in figures

7.1-7.3) when travelling whatever driving mission and no less than 300000 *km* (again around this value for the same previous reasons) when considering the established combination of all the missions together, on the other hand it is evident that the fuel consumptions increase substantially with T_a (figure 7.4). Actually, this considerable employment of fuel could be reduced without undermining battery duration. In fact, the variation of the $SOC_{var,best}$ with T_a , which has been determined by the PSO and occurs when the intervention of the cooling system is not sufficient alone for guaranteeing the desired battery duration, has implied an important imbalance among the driving missions, which do not generate no more an overall similar battery aging when travelled. Consequently, since the PSO implemented guarantees 200000 *km* for every driving mission, it follows that the results obtained can be widely influenced by the most problematic driving condition simulated. In particular, this disequilibrium among the missions, due to the increase of $SOC_{var,best}$ over T_a , occurs for two main reasons. First of all, as already shown in table 5.1, the eight driving missions travel different distances that, excluding the RWD03, are completely accomplished in charge depleting when the $SOC_{var,best}$ is set at 0.40 (i.e. $T_a \leq 26^\circ\text{C}$). Conversely, at higher T_a , when the $SOC_{var,best}$ raises in order to anticipate the passage to charge sustaining strategy and to reduce, in this way, the portion of *km* travelled in pure electric on a given driving mission, it results intuitive that the values of $SOC_{var,best}$ found out are influenced by the shortest mission considered (that is the *RTS 95*, table 5.1). In fact, because of this particular feature, this driving cycle needs a $SOC_{var,best}$ rather high in order to balance the quantity of *km* respectively travelled in Electric and Hybrid mode, whereas the others missions, since longer, would request lower values of $SOC_{var,best}$. Consequently, although some driving missions (such as the *WLTP* and the RWD04) could surely employ the pure electric modality for longer (reducing, in this manner, the corresponding fuel consumptions), they are instead limited by the briefest mission simulated. Moreover, the battery aging disparity caused by the raise of $SOC_{var,best}$ is also due to the different velocity evolutions characterizing the different driving missions considered. In fact, taking into account the *WLTP* (figure 5.1) it is evident that this driving cycle presents the most power demanding part at its end, as also testified by the frequent intervention of the ICE (shown in figure 5.11) that occurs when this cycle is travelled with the Electric mode selected at $T_a=25^\circ\text{C}$. Despite these frequent switches to the Hybrid mode, the final

part of the *WLTP* remains the most critical trait for the battery (both for a larger electric power demanding and a final temperature higher than the initial one), as the corresponding greater rate of SOH reduction (reported in figure 7.6) shows. Consequently, if the $SOC_{var,best}$ (due to T_a) is set at a value high enough to exclude completely this problematic portion, the total quantity of *km* achievable by the battery when travelling this mission increases decisively.

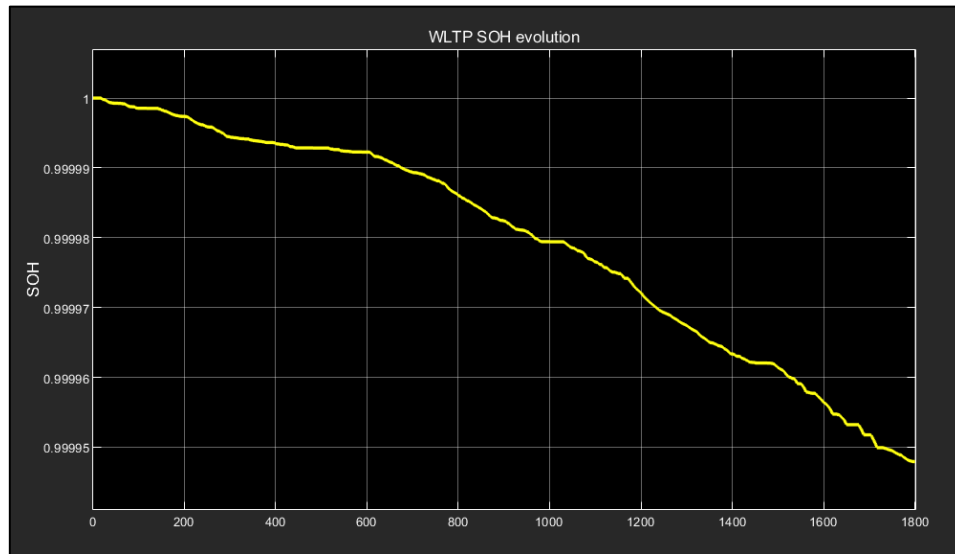


Figure 7.6: SOH evolution while travelling the WLTP at $T_a=25^\circ\text{C}$, in Electric mode and starting from a SOC value of 0.95, according to the conditions of table 5.2.

Therefore, in order to dissociate the PSO results from the accomplishment of the $L_{bat,km}$ constraint in the worst/shortest driving condition, which, as just illustrated, implies that with the other missions a larger and unfavorable fuel consumption occurs as a result of the related useless over-extension of battery duration, it can be thought to base the PSO solely on the fulfillment of $L_{bat,km,ave} \geq 300000 \text{ km}$. By acting in this way, lower values of $SOC_{var,best}$ and of $f_{100km,ave,best}$ can be achieved; however, the battery lifetime guaranteed by some driving missions can be decisively smaller than 200000 *km* and, consequently, problems arise if the vehicle is mainly used in a way analogous to the afore-said missions. Hence, this expedient is not satisfactory. A similar idea with similar outcomes would be that of employing customized life constraints for the different driving missions and the different T_a according to the respective (hard to assess) probability/frequency. More interesting results could instead be achieved if the EMS defined in the previous subchapter was also able to

access, at every moment, to an evaluation of the battery lifetime evolution (including the contribution of the corresponding potential plug-in recharge as well) from the beginning of the driving mission in question. In particular, this information could be obtained by continuously computing equation (43) and, as a result, equations (44) and (45) as well (but replacing the variables SOH_{end} , SOC_{end} and $s_{km,tot}$ referring to the final instant with those corresponding to the current instant SOH , SOC and s_{km}). In this way, it could be thought that, every time the passage to the charge sustaining modality is effectuated at a $SOC_{var,best}$ higher than 0.40 (according to PSO results), a comeback to the charge depleting strategy can be conducted, during the execution of the driving mission in question, if the lifetime value of the battery surpasses an opportune quantity, indicated as $L_{bat,km,up}$. Afterward, to be completely sure that both the imposed battery lifetime constraints are still fulfilled, it must also be set a lower limit of battery lifetime, indicated as $L_{bat,km,down}$, below which the EMS moves back to the charge sustaining strategy. Obviously, $L_{bat,km,up}$ and $L_{bat,km,down}$ could vary with T_a , but if reasonable fixed values are assigned to them in such a way as to ensure that the lifetime constraints adopted for the PSO are always satisfied, an already notable reduction in fuel consumptions can be obtained for both the cases of air conditioning on and off.

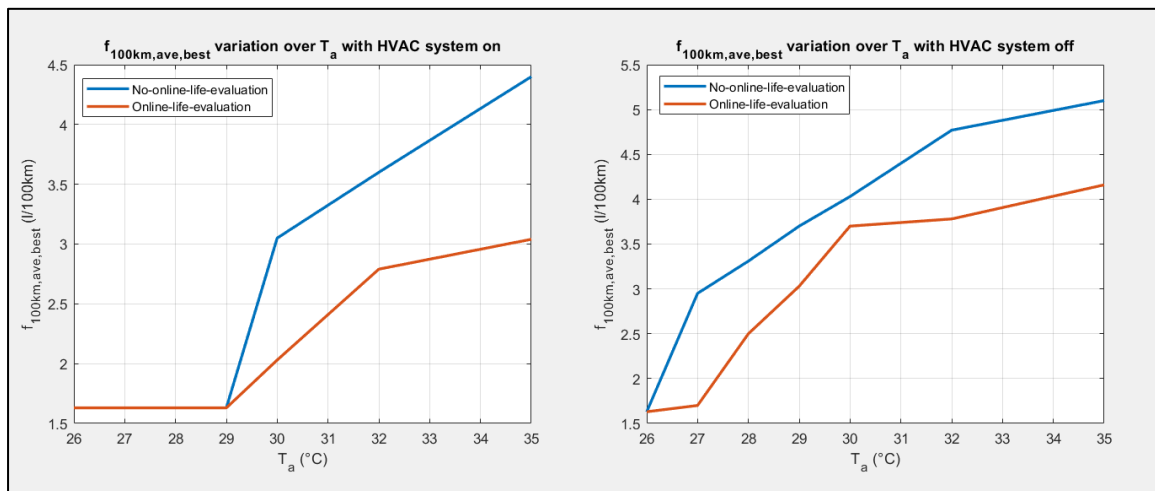


Figure 7.7: Improvements in fuel consumptions by means of an online evaluation of battery life evolution, for both cases of HVAC system on and off.

In particular, in figure 7.7 are reported the quantities $f_{100km,ave,best}$ obtained from the PSO (already depicted in figure 7.4) and the corresponding ones resulting from the

implementation of the latter expedient, specifically by using values of $L_{bat,km,up}$ and $L_{bat,km,down}$ respectively equal to 400000 km and 200000 km for the case with the HVAC system off and equal to 275000 km and 200000 km for the case with the air conditioning.

Therefore, the afore-said additional EMS feature surely constitutes an interesting aspect to be used in online management, but its actual development would imply in-depth considerations, evidently not conducted in this work.

8. Conclusions

This work aimed at illustrating the importance that a plausible thermal model of the battery (together with the related BTMS) holds for evaluating the actual aging rate of a HEV ESS during the quasi-static simulation of different driving missions. In fact, in accordance with the cycle life model by Wang [9], which is commonly employed in literature [20-22], it has been shown that little differences in the operating temperature of the battery (which are normally believed innocuous, especially if within the range 15°C-35°C [7]), mainly due to distinct climate conditions, can already imply a notable reduction of this component life. However, although this outcome could sound particularly disturbing, it must be considered that Wang's model, as specified in subchapter 2.1. *Capacity Fade Models*, extends over a rather ample thermal range and, therefore, could be inaccurate when evaluating modest variations of temperature (as indeed done in this paper). Moreover, it must also be remembered that the afore-said life model refers to a specific commercial type of Li-ion cell (A123 26650 [19]); consequently, the results attained in this work cannot be ascribed directly to Li-ion batteries in general, although a similar behavior can be expected. After these indispensable clarifications, it can be highlighted another important feature of this work, which concerns the implementation of the PSO destined to obtain a RB EMS able to conciliate together, at different ambient temperatures, fuel economy and battery safeguard. In particular, although the case considered here makes reference to a plug-in HEV inspired by the *Jeep® Renegade 4xe*, whose HV battery has been supposed cooled by means of cabin air, the optimization procedure realized can also be used for other hybrid electric vehicles and cooling systems. However, it is necessary to make some crucial elucidations about the implicit assumptions made while determining the underlying concepts of the specific PSO in question. In effect, the constraints about battery life, that have been employed in the calibration process, have been set at values rather high if compared to the effective distance a vehicle can

reach in 8-10 years (current calendar life of Li-ion batteries [2]) by simply travelling 41 km/day . Actually, the choice of using these thresholds has been made in order to align this paper to the corresponding portion of literature and, at the same time, to compensate all the possible omissions potentially caused by the utilization of simplified solutions in the modelling of the vehicle in *Simulink*. Moreover, it is also very likely that the average daily distance normally considered by the car manufacturers, for security reasons, is larger than the one employed here. Consequently, from these latter observations, it follows that, depending on the requirements at stake, the same PSO procedure here proposed could also be performed using different values of life constraints and daily use. Furthermore, it could be assumed too a different regularity with which plug-in recharge is effectuated. Hence, in these cases, it could potentially occur that, in contrast to what obtained in this work, the PSO does not output dissimilar energy managements at the different ambient temperatures, but that one fits all cases. However, this outcome must not be interpreted as a proof of the irrelevance of the temperature when varying between 15°C and 35°C , but rather as a clue about a possible under-sizing of the electric motor/motors supplied by the battery. In fact, since the fulfillment of the life constraints with an external temperature of 35°C would imply, for the above-mentioned reasons, that the battery durability at 25°C is unnecessarily large, it can be inferred that a more powerful electric motor (enabling the achievement of higher C-rate values) may be installed without implying durability issues. This possibility is certainly interesting because could reduce the intervention of the ICE while travelling short/medium trips, as it occurred while the simulation of the *WLTP* with the Electric mode selected (subchapter 5.2.). Analogously, in case the life requirements are not satisfied for any temperature, for 20°C neither, it can be concluded that the electric motor is probably over-sized for that particular battery. Therefore, on the whole, it is possible to assert that regardless of the parameters, which must be properly chosen anyway, the proposed PSO can result a valid tool while designing a HEV. However, in order not to neglect peculiar operating aspects of the vehicle, it is fundamental to simulate, as highlighted in this work, several driving missions and different load conditions. In doing so, though, the outcomes of the PSO can be particularly conditioned by the most critical mission. This fact is certainly precautionary, but implies that the fuel consumptions obtained with the RB controller are decisively

greater than those achievable by means of an offline EMS. However, this latter issue can be considerably resized, as sketched in subchapter 7.3. *High-Level Strategy*, if the RB EMS outputted by the PSO could also access, constantly, to an evaluation of the battery aging evolution. Obviously, the hints present in this paper are not sufficient and further studies should be conducted on this prospect. Furthermore, in order to integrate other questions here summarily debated, it would be undoubtedly interesting to improve, on the whole, the vehicle model simulated, to employ other typologies of Li-ion cells in order to make a comparison of aging rates (evaluated by means of the respective cycle life models) and to thoroughly inspect the battery operation at low temperatures so that it is possible to make a complete treatise of this thermal range as well.

References

Papers

- [1] European Parliament, “Electric road vehicles in the European Union: Trends, impacts and policies,” [https://www.europarl.europa.eu/RegData/etudes/BRIE/2019/637895/EPRS_BRI\(2019\)637895_EN.pdf](https://www.europarl.europa.eu/RegData/etudes/BRIE/2019/637895/EPRS_BRI(2019)637895_EN.pdf), accessed 5 October 2020.
- [2] Emadi, A., “Advanced Electric Drive Vehicles”, CRC Press, 978-1-4665-9770-9, 2015 by Taylor & Francis Group, LLC.
- [3] Governo italiano, “Intervista a La Stampa,” <http://www.governo.it/it/articolo/intervista-la-stampa/13627>, accessed 5 October 2020.
- [4] République Française, “Peut-on bénéficier du bonus écologique pour un véhicule hybride?,” <https://www.service-public.fr/particuliers/vosdroits/F32430#:~:text=Oui%2C%20%C3%A0%20conditi on%20que%20vous,d'au%20moins%20%20ans>, , accessed 5 October 2020.
- [5] Bloom I., Cole B. W., Sohn J. J., Jones S. A., Polzin E. G., Battaglia V. S., Henriksen G. L., Motloch C., Richardson R., Unkelhaeuser T., Ingersoll D., and Case H. L., “An accelerated calendar and cycle life study of Li-ion cells,” J. Power Sources, vol. 101, no. 2, pp. 238–247, 2001.
- [6] Jaguemont, J., Boulon, L., Dubé, Y. and Martel F., “Thermal Management of a Hybrid Electric Vehicle in Cold Weather,” in IEEE Transactions on Energy Conversion, vol. 31, no. 3, pp. 1110-1120, Sept. 2016.
- [7] Vidal, C., Gross, O., Gu, R., Kollmeyer P., Emadi A., “xEV Li-Ion Battery Low-Temperature Effects - Review,” in IEEE Transactions on Vehicular Technology, vol. 68, no. 5, pp. 4560-4572, 2019.
- [8] Rauhala, T., Jalkanen, K., Romann, T., Lust, E., Omar, N., Kallio, T., “Low-temperature aging mechanisms of commercial graphite/LiFePO₄ cells cycled with a simulated electric vehicle load profile—A post-mortem study,” Journal of Energy Storage, vol. 20 , pp. 344-356 , 2018.

- [9] Wang J., Liu P., Hicks-Garner J., Sherman E., Soukiazian S., Verbrugge M., Tataria H., Musser J., and Finamore P., "Cycle-life model for graphite- LiFePO₄ cells," J. Power Sources, vol. 196, no. 8, pp. 3942– 3948, 2011.
- [10] MathWorks, "Simulink," <https://www.mathworks.com/help/simulink/index.html>, accessed 5 October 2020.
- [11] Fiat Chrysler Automobiles, "Renegade 4xe and Compass 4xe: the Jeep® brand's take on the plug-in hybrid," <http://www.media.fcaemea.com/em-en/jeep/press/renegade-4xe-and-compass-4xe-the-jeep-brand-s-take-on-the-plug-in-hybrid>, accessed 5 October 2020.
- [12] Quattroruote, "Prova su strada Jeep Renegade," <https://www.jeep-official.it/content/dam/jeep/it/recensioni/pdf/renegade/Quattroruote-14112018.pdf>, accessed 21 October 2020.
- [13] Campellomotors, "Jeep Renegade scheda tecnica," <https://www.campellomotors.it/sites/default/files/2017-03/Jeep%20Renegade%20scheda%20tecnica.pdf>, accessed 21 October 2020.
- [14] Pneurama, "User friendly EVs with GKN eAxle," https://www.pneurama.com/en/rivista_articolo.php/User-friendly-EVs-with-GKN-eAxle-?ID=33852, accessed 21 October 2020
- [15] United States Environmental Protection Agency, "Compliance and Fuel Economy Data -Annual Certification Data for Vehicles, Engines, and Equipment," <https://www.epa.gov/compliance-and-fuel-economy-data/annual-certification-data-vehicles-engines-and-equipment>, accessed 21 October 2020.
- [16] Alix, G., Dabadie, J., and Font, G., "An ICE Map Generation Tool Applied to the Evaluation of the Impact of Downsizing on Hybrid Vehicle Consumption," SAE Technical Paper 2015-24-2385, 2015.
- [17] Le Berr, F., Abdelli, A., Postariu, D.-M., Benlamine, R., "Design and Optimization of Future Hybrid and Electric Propulsion Systems: An Advanced Tool Integrated in a Complete Workflow to Study Electric Devices", Oil Gas Sci. Technol., vol. 67, no. 4, pp. 547-562, 2012.
- [18] Anselma, P. and Belingardi, G., "Next Generation HEV Powertrain Design Tools: Roadmap and Challenges," SAE Technical Paper 2019-01-2602, 2019.

- [19] A123 Systems, "Nanophosphate® High Power Lithium Ion Cell ANR26650M1-B," online <https://www.batteryspace.com/prod-specs/6610.pdf>, accessed 5 October 2020.
- [20] Ebbesen, S., Elbert P. and Guzzella L., "Battery State-of-Health Perceptive Energy Management for Hybrid Electric Vehicles," in IEEE Transactions on Vehicular Technology, vol. 61, no. 7, pp. 2893-2900, 2012.
- [21] Onori S., Spagnol P., Marano V., Guezennec Y., and Rizzoni G., "A new life estimation method for lithium-ion batteries in plug-in hybrid electric vehicles applications," Int. J. Power Electron., vol. 4, no. 3, pp. 302–319, 2012.
- [22] Anselma, P., Kollmeyer, P., Belingardi, G., and Emadi, A., "Multitarget Evaluation of Hybrid Electric Vehicle Powertrain Architectures Considering Fuel Economy and Battery Lifetime," SAE Technical Paper 2020-37-0015, 2020.
- [23] Lin, X., Perez, H.E., Mohan, S., Siegel, J., Stefanopoulou, A., Ding, Y., & Castanier, M., "A lumped-parameter electro-thermal model for cylindrical batteries," J. of Power Sources, 257, 1-11, 2014.
- [24] Janarthanam, S., Burrows, N., and Boddakayala, B., "Factors Influencing Liquid over Air Cooling of High Voltage Battery Packs in an Electrified Vehicle," SAE Technical Paper 2017-01-1171, 2017.
- [25] Han, T., Khalighi, B., Yen, E. C., and Kaushik, S., "Li-Ion Battery Pack Thermal Management: Liquid Versus Air Cooling," ASME. J. Thermal Sci. Eng. Appl. ,11(2): 021009, 2018.
- [26] De Vita, A., Maheshwari, A., Destro, M., Santarelli, M., Carello, M., "Transient thermal analysis of a lithium-ion battery pack comparing different cooling solutions for automotive applications," Applied Energy, Elsevier, vol. 206(C), pages 101-112, 2017.
- [27] Yarpiz (2020), "Particle Swarm Optimization (PSO)," <https://www.mathworks.com/matlabcentral/fileexchange/52857-particle-swarm-optimization-pso>, MATLAB Central File Exchange, accessed 21 October 2020.
- [28] Mohan, G., Assadian, F., Longo, S., "Comparative analysis of forward-facing models vs backward-facing models in powertrain component sizing," IET Conference Publications, 10.1049/cp.2013.1920, 2013.
- [29] Jeep official, "Renegade 4xe, prestazioni," <https://www.jeep-official.it/4xe-ibrido/renegade-4xe/prestazioni>, accessed 5 October 2020.

- [30] Li, Q., Itoh, Y., Imanishi, N., Hirano, A., Takeda, Y., Yamamoto, O., "All solid lithium polymer batteries with a novel composite polymer electrolyte," *Solid State Ion.*, 159, 97–109, 2003.
- [31] Sapienza, Università di Roma, "Teorema di Thevenin," <https://www.sbai.uniroma1.it/sites/default/files/Teorema%20di%20The%CC%81venin.pdf>, accessed 5 October 2020.
- [32] Çengel, Y. A., "Termodinamica e trasmissione del calore", McGraw-Hill, 1997.
- [33] Holman JP., "Heat transfer, 10th ed.," Graw-Hill; 2002.
- [34] Kim Y., Mohan S., Siegel J. B., Stefanopoulou A. G. and Ding Y., "The estimation of radial temperature distribution in cylindrical battery cells under unknown cooling conditions," 52nd IEEE Conference on Decision and Control, Florence, 2013.
- [35] Jeon, D. H., Baek, S. M., "Thermal modeling of cylindrical lithium ion battery during discharge cycle," *Energy Conversion and Management*, vol. 52, no. 8-9, pp. 2973, 2011.
- [36] Arasu, M., Ahmed, Q., and Rizzoni, G., "Optimizing Battery Cooling System for a Range Extended Electric Truck," SAE Technical Paper 2019-01-0158, 2019.
- [37] Graziani Catullo, "Jeep Renegade 4xe ibrida plug-in, la prova dei consumi reali," <https://grazianicatullo.it/jeep-renegade-4xe-ibrida-plug-in-la-prova-dei-consumi-reali/>, accessed 5 October 2020.
- [38] Wikipedia, "Zona a traffico limitato, english version," https://en.wikipedia.org/wiki/Zona_a_traffico_limitato, accessed 5 October 2020.
- [39] Istat, "Temperatura e precipitazione nelle città capoluogo di provincia," <https://www.istat.it/it/archivio/242010>, accessed 21 October 2020.
- [40] UnipolSai, "Presentati i risultati dell'osservatorio sulle abitudini di guida degli italiani nel 2018 in seguito all'analisi delle scatole nere installate nelle automobili," https://www.unipolsai.com/sites/corporate/files/pages_related_documents/cs_osservatorio-unipolsai-2019.pdf, , accessed 21 October 2020.
- [41] Anci, "Mobilità sostenibile – Ricerca ANCI, nelle città serpenti di auto 'vuote', ma cala inquinamento," <http://www.anci.it/mobilita-sostenibile-ricerca-anci-nelle-citta-serpenti-di-auto-vuote-ma-cala-inquinamento/>, accessed 21 October 2020.
- [42] Wikipedia, "Particle swarm optimization," https://en.wikipedia.org/wiki/Particle_swarm_optimization, accessed 7 November 2020.

[43] Biswas, A., Anselma, P. G., Rathore, A., Emadi, A., "Comparison of Three Real-Time Implementable Energy Management Strategies for Multi-mode Electrified Powertrain," IEEE Transportation Electrification Conference & Expo (ITEC), Chicago, IL, USA, 2020, pp. 514-519, 2020.

Images

[a] Emadi, A., "Advanced Electric Drive Vehicles", CRC Press, 978-1-4665-9770-9, 2015 by Taylor & Francis Group, LLC.

[b] Kazemiabnavi, S., Dutta, P., Banerjee, S., "Ab Initio Modeling of the Electron Transfer Reaction Rate at the Electrode-Electrolyte Interface in Lithium-Air Batteries," ASME International Mechanical Engineering Congress and Exposition, Proceedings (IMECE). 6. 10.1115/IMECE2014-40239, 2014.

[c] Waldmann, T., Wilka, M., Kasper, M., Fleischhammer, M., Wohlfahrt-Mehrens, M., "Temperature dependent ageing mechanisms in Lithium-ion batteries—A post-mortem study," J. Power Sources, vol. 262, pp. 129–135, 2014.

[d] Anselma, P. and Belingardi, G., "Next Generation HEV Powertrain Design Tools: Roadmap and Challenges," SAE Technical Paper 2019-01-2602, 2019.

[e] <https://www.jeep-official.it/4xe-ibrido/renegade-4xe>, accessed 5 October 2020.

[f] A123 Systems, "Nanophosphate® High Power Lithium Ion Cell ANR26650M1-B," online <https://www.batteryspace.com/prod-specs/6610.pdf>, accessed 5 October 2020.

[g] Shekhawat, A., "Particle Swarm Optimization," <https://arjn95.medium.com/particle-swarm-optimization-8ad9a88a81e3>, accessed 21 October 2020.

[h] Han, T., Khalighi, B., Yen, E. C., and Kaushik, S., "Li-Ion Battery Pack Thermal Management: Liquid Versus Air Cooling," ASME. J. Thermal Sci. Eng. Appl. ,11(2): 021009, 2018.

[i] Esmine, A., Coelho, R. A., Matwin, S., "A review on particle swarm optimization algorithm and its variants to clustering high-dimensional data," Artificial Intelligence Review, 44, 23-45, 2013.

Acknowledgements

Throughout the writing of this thesis I have received a great deal of support and, therefore, I would like to express my gratitude to all the people who have sustained me.

I would first like to thank my supervisors, Prof. Giovanni Belingardi and Ing. Pier G. Anselma, whose knowledge was crucial in developing the research aims. In fact, their feedbacks truly helped me to refine and enhance my dissertation. In particular, I really owe a lot to Ing. Anselma, who has constantly given fundamental recommendations about the progress and the purposes of this work.

I would then like to express my infinite gratitude to my family, my parents Gabriella and Roberto, my siblings Luca and Cecilia, my grandparents Anna, Mario, Franca and Vittorio, who have helped me during the whole university studies.

Special thanks to all my university mates and friends, especially to Roberto, Emanuele, Antonio, Miriam, Paolo, Lorenzo, Giocchino, Joshua, Iru and Francesco.

I would also like to sincerely acknowledge Fede and her whole family.

Thanks to my aunts Silvia and Diana.

Finally, many thanks go to Politecnico di Torino and Edisu that made the achievement of this goal possible.